The University of Oxford

Preparation and Characterisation of Encapsulation Magnetic Metal Iron Oxide Nanoparticles

Ali Al-Saadi

19th/ January/ 2012

Inorganic Chemistry Department

Outline

Declaration

I declare that the work done experimentally and presented in this thesis is my own unless stated otherwise. The work in this thesis is built upon previous studies from my fellow students with the sources of information properly cited and acknowledged.

Acknowledgements

First I would like to take this opportunity to sincerely thank my supervisor, Prof. Edman Tsang, for giving me this golden opportunity to work in this most competitive 'nanotechnology' area.

Secondly, I would like thanks Dr Vitaliy Khutoryanskiy for his assistance in this project, Dr Chester Lo from Iowa State University for his help with the VSM analysis. Thirdly, I would like to thank my sponsors, National Physical Laboratory (NPL) and Engineering and Physical Science Research Council (EPSRC) for funding this project.

I would like to deeply thank my friends and colleagues who have given me their support, advice, encouragement and all other contributions during execution of this research and thesis preparation. Particularly, the helps from Dr Chih Hao Yu is kindly acknowledged.

I am also indebted to all members, staff and lab technicians including, John Baun in the chemistry department at University of Reading and Phil Wiseman in the Inorganic Chemistry Laboratory at University of Oxford for their helps by making a friendly working environment.

I am grateful to Prof. Colquhoun and his group including Dr Mathew Bird and Dr Zhixue Zhu for maintaining friendly environment, tidy and clean place in shared Tsang-Colquhoun laboratory in the first two years of course and I am thankful to Phil Wiseman for the training and the use of SQUID at University of Oxford.

Abstract

One of the most challenging goals in nanoparticle research is to develop successful protocols for the large-scale, simple and possibly low-cost preparation of morphologically pure nanoparticles with enhanced properties. The work presented in this thesis was focused on the synthesis, characterisation and testing of magnetic nanoparticles and their potential applications. There are a number of magnetic nano-materials prepared for specific applications such as metal oxide nanoparticles encapsulated with various porous materials including Fe_3O_4/Fe_2O_3 coated with soft bio-organic materials such as glycol chitosan and bovine serum albumin and hard materials such as silica (SiO_2) and zinc sulphide (ZnS). The preparation of these materials was achieved principally by bottom-up methods with different approaches including micro-emulsion, precipitation, electrostatic and thermolysis processes.

The thesis also presents the uses of various analytical techniques for characterising different types of nano-materials including Attenuated Total Reflection Fourier Transformer Infrared Vibrational Spectroscopy (ATR-FTIR), Ultraviolet Visible-Near Infrared (UV-Vis-NIR) Spectroscopy, Zeta Potentiometric Surface Charge Analysis, Superconducting Quantum Interference Device (SQUID) and Vibration Sample Magnetometry (VSM) for magnetic analysis and powder X-Ray Diffraction (XRD) for crystallographic pattern analysis.

There are many applications of magnetic nanoparticles, including nano-carriers for biological and catalytic reagents. The magnetic nanoparticles can facilitate separation in order to isolate the carriers from solution mixtures as compared to many inefficient and expensive classic methods, which include dialysis membrane, electrophoresis, ultracentrifugation, precipitation and column separation methods.

There are six key chapters in this thesis: the first chapter introduces the up-to-date literature regarding magnetic nano-materials. The uses of magnetic nano-materials in drug binding and for protein separation are discussed in the second and third chapters. The fourth chapter presents the use of magnetic nanoparticle in conjunction with a photo-catalytic porous overlayer for the photo-catalytic reduction of organic

molecules. The fifth chapter describes different analytical techniques used for the characterisation of nanoparticles and the underlying principles and the experimental details are also given. The sixth chapter summarises the results and provides an overview of the work in a wider context of future applications of magnetic nanoparticles.

Abbreviation

ATR-FTIR	Attenuated Total Reflection- Fourier Transformer Infrared
BET	Brunauer Emmett Teller
BSA	Bovine Serum Albumin
CD	Circular Dichroism
CTAB	Cetyltrimethylammonium
EDX	Energy Dispersion X-ray
FePt	Iron Platinum
Fcc	Face Centred Cubic
Fct	Face Centred Tetragonal
Fe_3O_4/ Fe_2O_3	Magnetite/ Maghemite Iron Oxide
FWHM	Full Width at Half Maximum
H_c	Coercivity
HRTEM	High Resolution Transmission Electron Microscope
IEP	Isoelectric Point
Igepal CO-520	Polyoxyethylene (5) nonylphenylether
M_s	Saturation Magnetisation
ME	Micro-Emulsion
M_r	Remnant Magnetisation
SA	Surface Area
SAED	Selected Area Electron Diffraction
SAXS	Small Angle X-Ray Diffraction
$SiO_2@Fe_3O_4$	Iron Oxide Encapsulated in Silica
TGA	Thermal Gravimetric Analysis
TEM	Transmission Electron Microscope
TEOS	Tetraethyl Orthosilicate
UV-Vis-NIR	Ultra Violet Visible Near Infrared
VSM	Vibrating Sample Magnetometer
WO	Water to Surfactant Ratio
XRPD	X-Ray Powder Diffraction

Chapter One

Introduction

Contents

1.1 Overview

The use of magnetic nanoparticles has recently been demonstrated to give a wide range of technological possibilities. The majority of research has been focused on the assembly of magnetic nanoparticles as thin films for applications in optical, electrical and magnetic storage systems. Their application as magnetic separable *nano-vehicles* for chemical or biological species is a new area with rather different criteria, and this area is the main focus in this thesis.

The facilitated separation of small magnetic particles carrying biologically or chemically active species from solution has a potential for many applications. For example, in the field of fine chemical manufacture, the expensive catalyst component such as noble metal or enzyme, after tagged with a magnetic particle can be captured for re-use by magnetic means. However, this technique is not problem-free. This includes the intrinsically weak magnetic properties of tagged species, magnetic interferences from neighbouring particles in solution, poor stability of small magnetic particles and no specific interaction with bio- or chemical species, which remain as the key issues.

In this Chapter we now review some synthetic approaches to make magnetic iron oxide particles, the methodologies for their surface passivation & functionalisation and the relevant literature prior to our studies.[1-5]

1.2 Synthesis

1.2.1. Organometallic routes

There are many reported methods for preparing iron oxide based magnetic nanoparticles and these methods are also adopted for the preparation of other magnetic metallic or alloy nanoparticles. The methods include the polyol process, thermolysis decomposition,[6-20] reverse micelles [8,21-24] and sonochemical decomposition, etc.[25] Many of them are based on the decomposition of reactive organometallic species. For example, using iron pentacarbonyl to form iron containing nanoparticle in the presence of oleic acid or polyvinyl pyrrolidone. The nano-size iron is then undergone a controlled oxidation in air to iron oxide. The iron oxide nanoparticles obtained by these methods were relatively monodispersed. For example, Hyeon and co-workers [25] used this route to produce a series of monodispersed maghemite (Fe_2O_3) from 4 to 16 nm (figure 1). His group first prepared iron nanoparticles in the presence of oleic/lauric acid and they then carried out an oxidation procedure to convert the iron particles to iron oxide using trimethylamine oxide in dioctyl ether. No size selective process was required to further narrow the size range of the particles. [25]

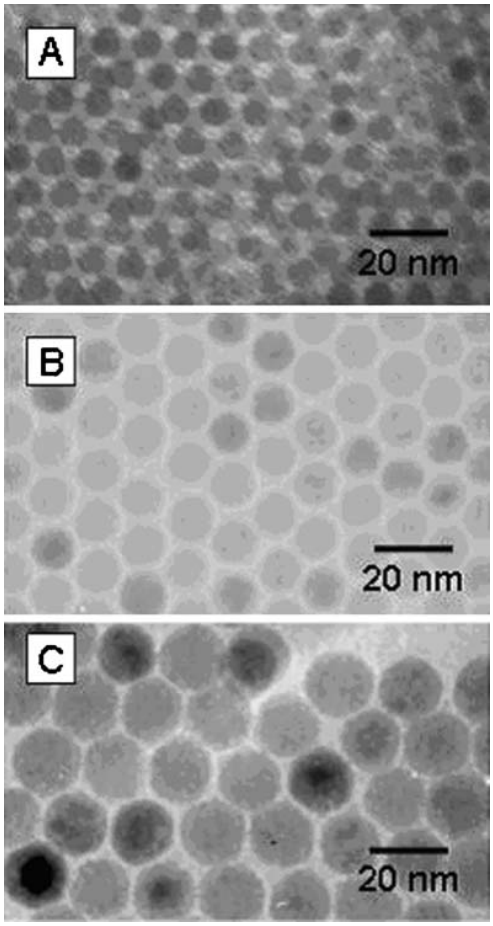

Figure 1: Examples of iron oxide nanoparticles of different sizes [25]

1.2.2 Reverse micelle

Commonly an emulsion is made where oil droplets are added to water in a very small concentration. In reverse micelle, a small concentration of water is added to an oil phase. The dispersions of the water droplets in oil and oil droplets in water are successfully achieved by the addition a surfactant and sometimes with a co-surfactant (figure 2). When the concentration of the surfactant reaches a critical micelle concentration (CMC), surfactant molecules start to aggregate. The shape of these micelles is normally spherical but other shapes are possible such as ellipsoidal and cylindrical. The shape and size of micelles depend on the type of surfactant used as well as the conditions adopted such as concentration, pH, temperature and ionic

strength. By templating these micelles of different morphologies nanoparticles of different sizes and shapes can be made accordingly, as shown in figure 3.

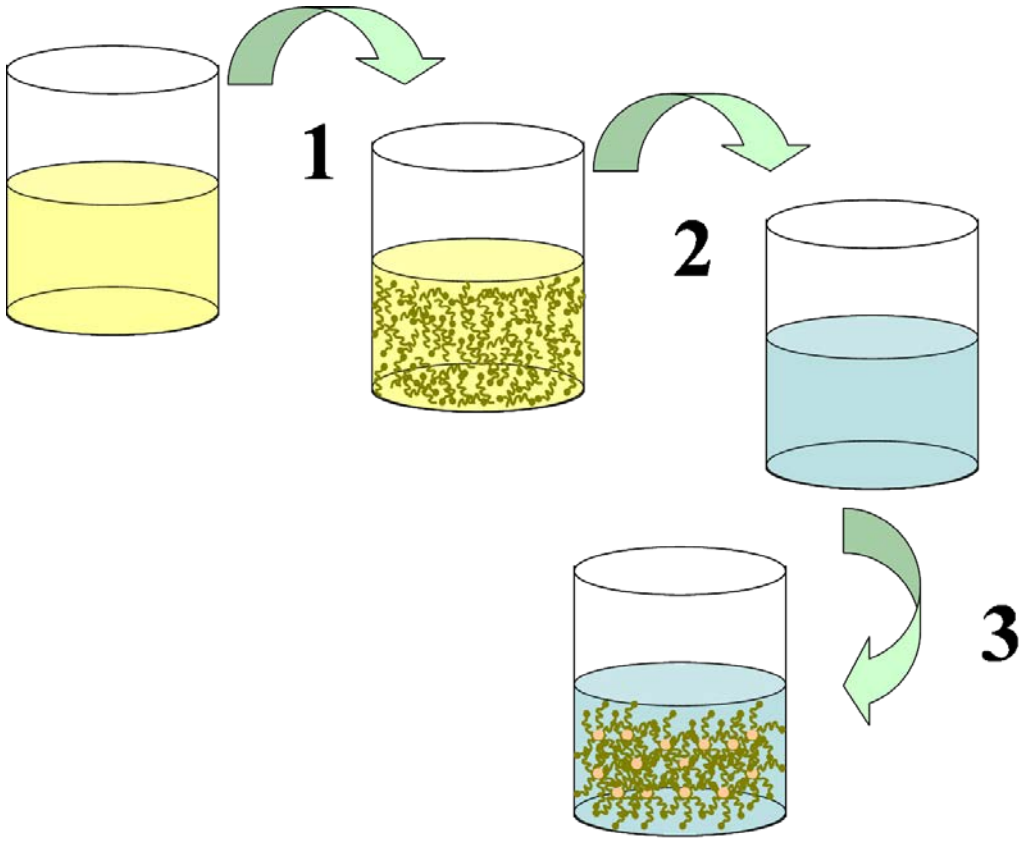

Figure 2 shows oil droplets stabilised with surfactant in water solution. The procedure involves 1) the addition of cationic surfactant such as CTAB in toluene, 2) addition of surfactant CTAB toluene in polar solvent such as deionised water to form 3) oil surfactant water system.

Earlier in Oxford it was shown that iron oxide magnetic nanoparticles can be made inside a reversed micelle. The water droplet containing Fe^{2+} and Fe^{3+} when mixed with alkaline solution formed nanosize iron oxide inside the reversed micelle. The magnetic particle was then encapsulated with a silica particle with tuneable size from 4-13 nm by adjusting the water to surfactant ratio.[21, 27-29] Silica is a porous material that can entrap various drug molecules for delivery,[30-32] e.g. for tumour therapy[33-35] and can host other biological reagents such as antigens and antibodies.[36,37]

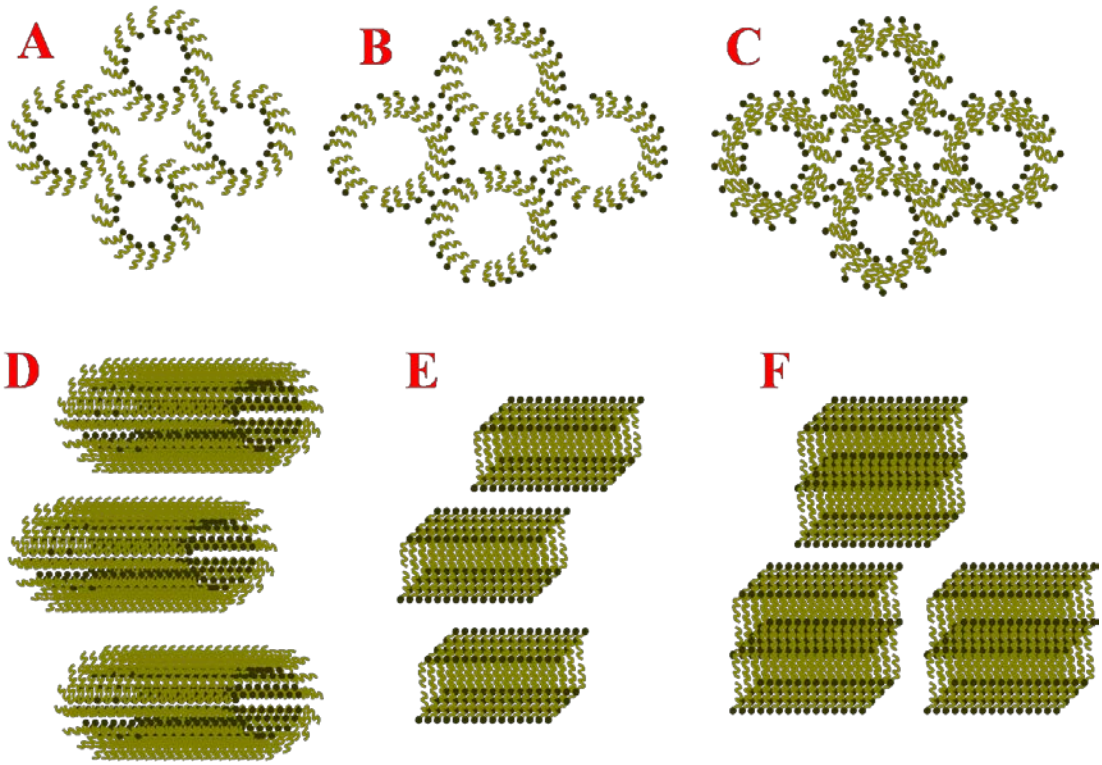

Figure 3 show different structure of surfactant above critical concentration of aggregation including A) inverse micelles, B) micelles, C) liposome, D) cylindrical, E) bilayer sheet and F) laminar.

1.2.3 Sol-gel method

The chemical solution deposition system called ‘sol-gel’ process can be used to prepare porous oxide coatings. The process involves hydrolysis and polycondensation reactions at various stages with metal oxide precursors such as metal alkoxides and chlorides. During hydrolysis a metal oxide is produced as a result of the metal centres becoming interconnected via oxo (M-O-M) or hydroxyl (M-OH-M) bridges. Further polymerisation condensation reactions give small particles in solution. Larger sized gels are formed at the solid liquid interface when the particles start to aggregate to form polymeric oxide network. The interesting aspect of this method is that finely divided nanoparticles if present in solution, are entrapped in the sol-gel coating. The extent of aggregation of these small nanoparticles can be much reduced as the small particles can be quickly encapsulated by the sol-gel material facilitating their

separation. The first study of sol-gel process dates from the 1880s in the use of silicon alkoxides such as tetraethyloxysilane (TEOS) in water and ammonium hydroxide to give porous silica gel (SiO_2): the reaction scheme is shown in the figure 4. This process was investigated in this thesis in order to synthesise silica protected magnetite nanoparticles in a sol-gel matrix while the magnetic particles are formed.

$$Fe^{2+}_{(aq)} + 2Fe^{3+}_{(aq)} + 8OH^{-}_{(aq)} \rightarrow Fe_3O_{4(s)} + 4H_2O_{(l)}$$

$$Si(CH_3CH_2O)_{4(l)} + 4NH_3.H_2O_{(l)} \rightarrow 4CH_3CH_2OH_{(l)} + 4NH_{3(g)} + Si(OH)_{4(s)}$$

$$4NH_{3(g)} + 2Si(OH)_{4(s)} \rightarrow 2SiO_{2(s)} + 4NH_3.H_2O_{(l)}$$

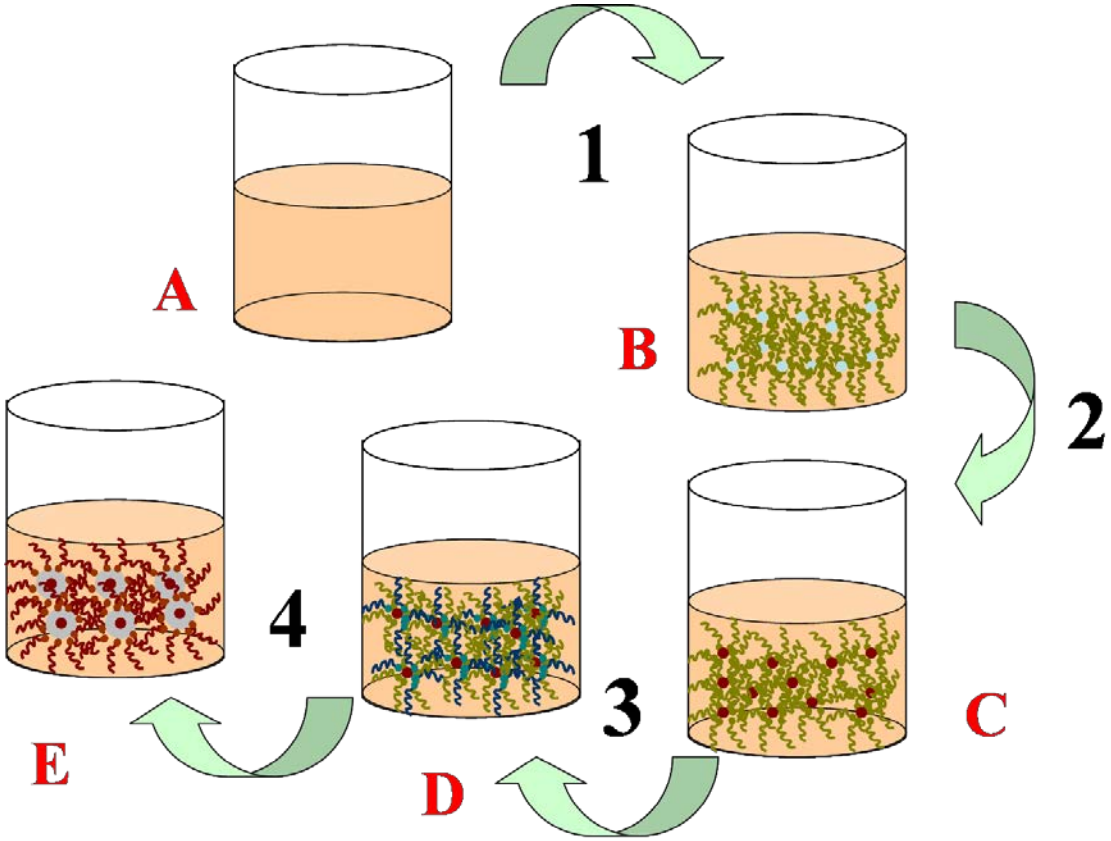

Figure 4 shows the synthetic procedure for the sol-gel process. A) addition of toluene, B) addition of aqueous Fe(II) + Fe(III) + CTAB surfactant, C) addition of ammonia solution, D) addition of TEOS, E) addition of ammonia solution. The synthetic process involves: 1) the addition of water droplet with dissolved Fe(II) + Fe(III) stabilised by the CTAB surfactant, 2) addition of ammonia drop wise for the preparation of iron oxide by the controlled precipitation method, 3) addition of TEOS silica precursor, 4) hydrolysis and condensation of silica encapsulating iron oxide nanoparticles.

1.2.4 Polyol process

In recent years, reductions of organometallic species are usually carried out in a high boiling poly-alcohol solvent at elevated temperature such as ethylene glycol, propylene glycol. This process is, known as the 'Polyol process', which has been applied for the preparation of metallic or semiconductors quantum dots. The Polyol Process was utilised in this thesis for the preparation of magnetic nanoparticles which

will be described in later chapters. The idea of using the organometallic route to make metallic nanoparticles in the high boiling alcohol was originated from Bawendi. [37] The employment of appropriate stabiliser in the alcohol was important in preventing the nanoparticles or magnetic nanoparticles from agglomeration in solution. [38] Many studies have been carried out in this area for the preparation of a wide range of magnetic nanoparticles. The most popular route involves thermal decomposition of metal complexes such as iron pentacarbonyl, $Fe(CO)_5$ and dicobaltoctacarbonyl, $Co_2(CO)_8$ above 200 ^oC in an inert atmosphere (nitrogen or argon) in the presence of different types of stabilisers, yielding monodispersed nanoparticles.[6,39,40] Such complexes decomposed rapidly within few minutes at elevated temperature, liberating carbon monoxide (*figure* 5).

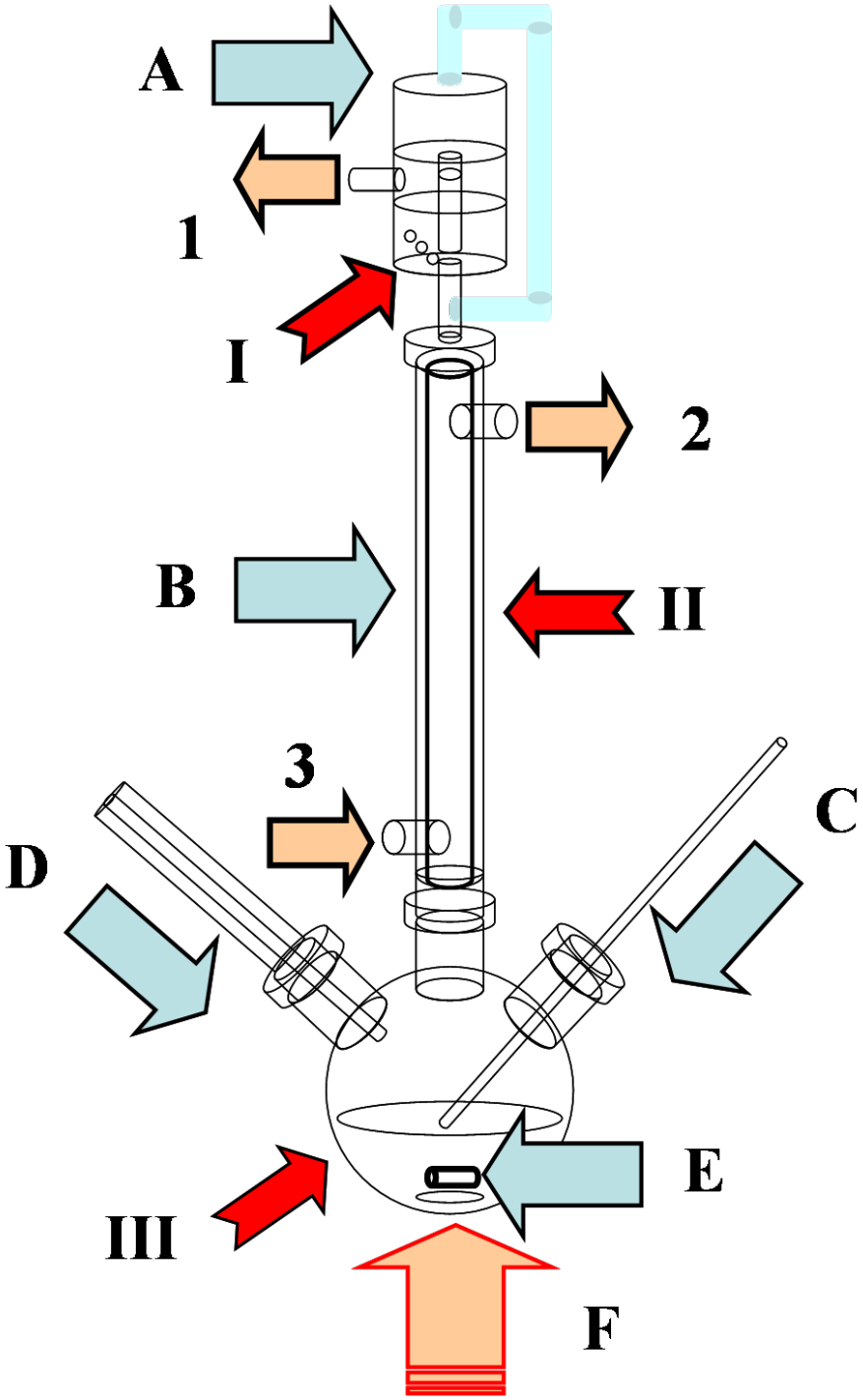

Figure 5 shows the setup for the Polyol process including: A) oil bubbler, B) condenser, C) mercury thermometer, D) nitrogen gas bubbler, E) stirrer and F) heater with acquired chemical: I) paraffin oil, II) water cooling bath, III) dioctyl ether + metal precursor + surfactant. The nitrogen gas passes out from the oil bubbler through 1) to ensure that no leak in a properly sealed apparatus. Cold water enters the condenser through 2) below and rises and passes out through 3) providing cold jacket to condense slightly volatile solvents.

It is known that the use of a capping agent can stabilise nanoparticles, which can offer a steric barrier to prevent particles from agglomeration in solution. Moreover, the capping agent plays an important role in dictating the size of nanoparticles. The early study of iron nanoparticles revealed that oleic acid is a good capping agent, possibly because the double bond present in this capping agent gives rigidity and stability to the surface passivation.[41] Other capping agents such as oleylamine and trialkylphosphine gave slower growth of particles. These reagents are labile and reversibly bound to the surface of nanoparticles and can come off easily when nanoparticles are extensively washed. A strongly binding capping agent inhibits growth of particles, while a weak binding agent allows rapid growth. The capping agents not only can prevent agglomeration but also reduce surface oxidation.

1.3 Surface modification & protection of magnetic nanoparticles

Stabilisation of magnetic nanoparticles in solution for long periods of time without agglomeration or precipitation is a key challenge. Although there are many developments in the synthesis of magnetic nanoparticles, stability of these particles in solution remains to be the most important issue. Pure magnetic nanoparticles such as Fe, Co and Ni can be spontaneously oxidised in air. Their susceptibility to air oxidation becomes substantially higher as the size of nanoparticle decreases and it is vital to develop new methods for the protection of these magnetic nanoparticles. To achieve this goal a protective layer that is impenetrable to oxygen molecules is required, which often involves chemical bonding by surface atoms on the particle.

As a result, various methods used for the preparation of protective layers on magnetic nanoparticles against oxidation and erosion by acid and base have been carefully considered. These methods generally involve the formation of core-shell structures where the naked magnetic nanoparticles are placed as the core and the protective layer as the shell. The core is isolated by the shell from the surrounding environment by providing a protective barrier where no direct contact can be made. The protective coating can be categorised roughly to two groups, namely organic shells including

polymers and surfactants,[42-46] and inorganic layers, including silica,[44] carbon,[45] noble metals such as Ag[47] and Au[48,49].

1.3.1 Passivation of magnetic nanoparticles by mild oxidation

A very cheap and relatively easy method for protecting magnetic metallic or alloy nanoparticles is by a controlled surface oxidation of the metal nanoparticles. This technique is long known for the treatment of air sensitive supported catalysts and can be achieved by various methods. For instance, Peng *et al.* reported a method for nanoparticles preparation/passivation using plasma-gas-condensation deposition apparatus.[50] Boyen *et al.* reported the use of an oxygen plasma to oxidise the surface of cobalt nanoparticles.[51] Controlling the oxidation of the outer layer can give a profound impact in the magnetic exchange-biased systems between ferromagnetic core and antiferromagnetic material shell. A mild oxidation method was developed by Bönnemann *et al* who used air to partially oxidise cobalt nanoparticles to give CoO outer layer. This layer was shown to stabilise the cobalt nanoparticle from further oxidation. [52]

1.3.2 Coating magnetic nanoparticles with polymer and surfactant

Surface passivation of magnetic nanoparticles during and after synthesis with surfactant and polymer is crucial to avoid agglomeration. The organic based stabiliser with functional terminal groups can keep the particles dispersed in solution by the introduction of electrostatic or steric repulsions between these organic molecules as previously described by Papell in 1965.[53] In fact, the net surface charge [54] and the nature of surfactant molecule [55-57] adsorbed on the surface of ferromagnetic nanoparticles are the major factors affecting their colloidal stability in solutions. A typical example is the ferrofluid (Fe_3O_4) that can be synthesised by controlled precipitation of Fe^{2+} and Fe^{3+} in ammonium hydroxide or sodium hydroxide solution. The magnetite nanoparticles are only slightly negatively charged in neutral pH (the isoelectric point is close to pH7), which can result in highly unstable colloidal particles. There are a number of ways to re-disperse these magnetic nanoparticles in

solution. The addition of organic or inorganic based surfactants such as aqueous tetramethylammonium hydroxide or aqueous perchloric acid can result in the rapid re-dispersion of the magnetite nanoparticles through surface adsorption.[54] Another approach is to redisperse the particles in nitric acid which oxidises them to γ-Fe_2O_3.[58] Magnetic nanoparticles can be chemically adsorbed or anchored by surfactants or polymers, creating repulsive single or double layers. The forces of van der Waals attraction and steric repulsion by the protective layers are balanced, which keeps the stabilised particles in a colloidal form.

Polymers containing carboxylate acid, phosphate, or sulphate functional groups can bind to the surface of magnetite.[59] Polymers such as poly(pyrrole), poly(aniline), poly(alkylcyanoacrylates), poly(methylidene malonate), or polyesters, such as poly(lactic acid), poly (glycolic acid), poly(e-caprolactone), and their copolymers can be used.[60-63] Biocompatible polymers coated magnetic nanoparticles were intensively studied for drug binding and as contrast agents for magnetic resonance imaging.[164,165] Polymer coated magnetite nanoparticles using inverse micro-emulsion in organic solvent was recently reported by Chu *et al.*[66] The magnetite nanoparticle was first formed in the reversed aqueous micelle. The polymer was then coated on the magnetite particles using an oil soluble mixture of the monomer (methacrylic acid and hydroxyethyl methacrylate) together with addition of the crosslinker molecule (*N,N'*-methylenebis(acrylamide)) and, finally, an initiator (2,2-azobis(isobutyronitrile)), all under a nitrogen atmosphere. The polymerization reaction took place at the oil-water interface at 55 ^{o}C. The coated magnetite nanoparticles were precipitated in acetone methanol mixture in 9:1 volume ratio and then redispersed in toluene. The magnetite showed a superparamagnetic behaviour with an average size of 80 nm.

Similarly, ferromagnetic nanoparticles can also be coated with polyaniline in the presence of aniline, poly(acrylic acid) and ammonium persulphate.[67] The size distribution of nanoparticles was around 20-30 nm with the core-shell structure, as reported by Asher *et al.*[68] The iron nanoparticles with an average size 10 nm can be embedded in polystyrene using emulsion polymerization, which can give stable superparamagnetic photonic crystals.[69] The same method was used by Zhang *et al.* to coat $MnFe_2O_4$ nanoparticles with polystyrene using a radical polymerization method to form core-shell nanoparticles with sizes below 15 nm.[70] The $MnFe_2O_4$ magnetic

nanoparticles were stirred at pH 4 overnight using 3-chloropropionic acid, and dried in air after washing to remove excess $K_2S_2O_8$ initiator. The magnetic $MnFe_2O_4$ nanoparticles were then added to styrene under a nitrogen atmosphere. A xylene solution containing CuCl and 4,4-dinonyl-2,2-dipyridyl was added. The solution was stirred and kept at 130 ^oC for 24 h to give the polystyrene coated $MnFe_2O_4$ nanoparticles. The procedure can be used to prepare polystyrene nanoparticles without the magnetic core when the metal precursors are not included in the recipe. Magnetic nanoparticles with single or double layers of surfactant and polymer are not air-stable and are easily corroded by acidic solution.[71] The coatings are not stable especially at high temperature and can be degraded by the catalytic effect of the core nanoparticles. The development of new methodology for the protection against oxidation still remains a challenge.

1.3.3 Noble metal coating

The deposition of noble metal on the surface of magnetic nanoparticle by various methods including microemulsion,[72,73] redox transmetalation,[74–76] iterative hydroxylamine seeding,[77] was purposely established for protection of the magnetic particle against oxidation as noble metals are generally easily reduced and difficult to oxidize. Coating of cobalt nanoparticles (6 nm diameter) with platinum was reported by Cheon *et al*. [74] The cobalt nanoparticles was refluxed with Pt-(hexafluoroacetylacetonate)$_2$ for 8 h in nonane in the present of $CH_3(CH_2)_{11}CN$ stabilizer. The coated magnetic nanoparticles were obtained in powder form by isolating the particles from ethanol solution using centrifugation. Figure 6 shows the TEM images of cobalt nanoparticles coated with platinum. The size of the coated magnetic nanoparticles was below 10 nm.

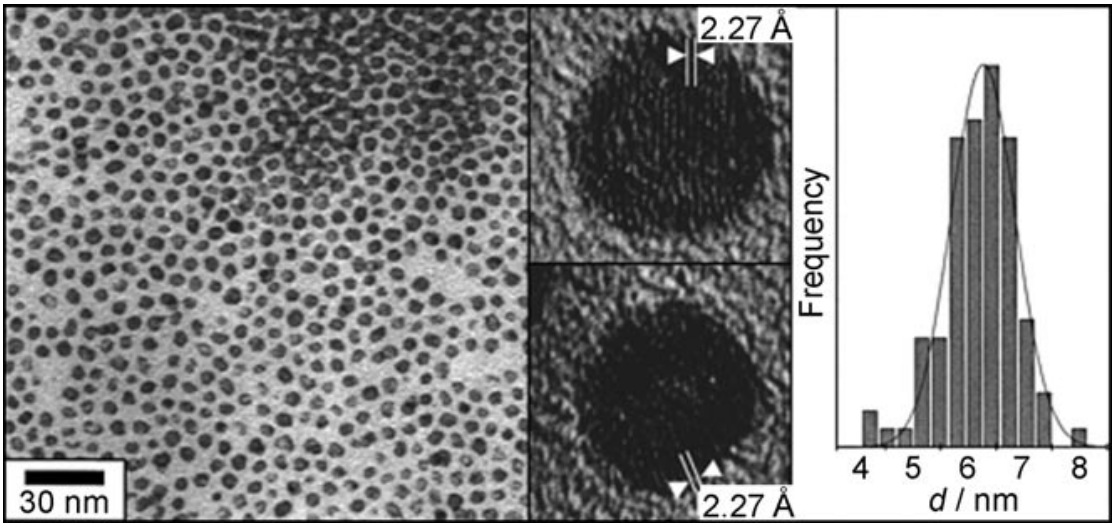

Figure 6. Left: TEM images of Co coated with Pt in core-shell structure. The spacing of the lattice fringes shown in the high resolution images corresponds to the Pt (111) plane. Right: plot of the particle size distribution. The image was taken from reference. [74]

The coated magnetic nanoparticles were air stable and can be re-dispersed in organic solvents. It has been shown that the solution contained Co (hexafluoroacetylacetonate)$_{2,}$ indicating the core-shell structure was formed as a result of redox reaction between Co^0 and Pt^{2+}. Precious metals such as gold can also be used as a coating due to its low reactivity. [178-181]

Iron nanoparticle coated with gold with the core size of about 11 nm and 2.5 nm thickness of gold shell was reported by O'Connor and co-workers.[66] Under acidic and neutral pH the coated iron nanoparticles were found to be stable. The coating was successfully achieved in an aprotic polar solvent such as 1-methyl-2-pyrrolidinone (NMPO). $FeCl_3$ was dissolved in NMPO containing sodium and naphthalene. The solution was stirred vigorously at room temperature. The Fe^{3+} ions were reduced to iron particles by metallic sodium. The sodium chloride by-product was removed by centrifugation. The iron nanoparticles were then coated with gold by the addition of the capping agent 4-benzylpyridine at elevated temperature and dehydrated $HAuCl_4$ pre-dissolved in NMPO. A reverse microemulsion method was also employed to prepare gold-coated iron nanoparticles successfully. Cetyltrimethylammonium

bromide (CTAB) and 1-butanol were used as co-surfactants to form the reverse micelles in the octane oil phase. $NaBH_4$ was used to reduce $FeSO_4$, followed by the reduction of $HAuCl_4$ for the coating of the magnetic nanoparticles.[48] A new but advanced method for the preparation of iron nanoparticles coated with gold was recently reported by Zhang *et al.* using laser irradiation in wet chemistry. The laser was used to deposit the gold shell onto the surface of iron magnetic core.[82] The body centered cubic (*bcc*) iron core of 18 nm was coated with *fcc* gold shell of 3 nm thickness. The single domain of iron nanoparticles exhibiting superparamagnetic behaviour with a blocking temperature of 170 K was recorded. The M_{sat} value was determined to be 210 emu/g approaching 96% of the bulk value.

Cobalt nanoparticles coated with gold were reported by Guo *et al.* This method was based on chemical reduction.[83,84] Lithium triethylhydridoborate was employed as a reducing agent to prepare the cobalt nanoparticles and 3-(*N*,*N*'-dimethyldodecylammonio) propanesulfonate was used as a surfactant to prevent their agglomeration. The produced cobalt nanoparticles were added to $KAuCl_4$ pre-dissolved in tetrahydrofuran (THF) under an inert atmosphere. The gold shell was formed on the surface of cobalt nanoparticles via the controlled reduction of Au^{3+} using the same lithium triethylhydridoborate solution. Thiol groups can be added to the gold coated magnetic nanoparticles for catalytic and optical applications.[85]

1.3.4 Silica coating of magnetic nanoparticles

Silica coating on magnetic nanoparticle was reported to reduce unwanted interaction(s) with external chemical species.[86] In addition, the silica shell shows great stability under a wide pH range, its surface can also be functionalised to carry chemical or biochemical species with a controllable shell thickness. For example, silica-coated magnetic nanoparticles can be prepared using the Stöber method as previously described.[87-91] By varying the concentration of ammonium hydroxide and the ratio of tetraethoxysilane (TEOS) to water the thickness of the silica shell can also be nicely tailored. Organic additives with various functional groups can easily be attached on the silica shell by means of many well established methods.[92] This allows additional functionality such as bio-labelling, drug targeting, and drug delivery

to be implemented. It was demonstrated that magnetic iron oxides hematite (Fe_2O_3) and magnetite (Fe_3O_4) can be coated with silica shells.[93-95] The surfaces of the iron oxide particles are compatible to those of silica, which make the coating firmly attached to these oxides.

Commercially available ferrofluids directly coated with silica shells through controlled hydrolysis of TEOS was demonstrated by Xia and co-workers.[89] Various amounts of TEOS were added to the ferrofluid and the formation of the coating was completed at room temperature within 3 hours, giving controllable thickness of the silica coating. Their TEM images clearly showed that each iron oxide nanoparticle was encapsulated in a silica particle, as seen in figure 7.

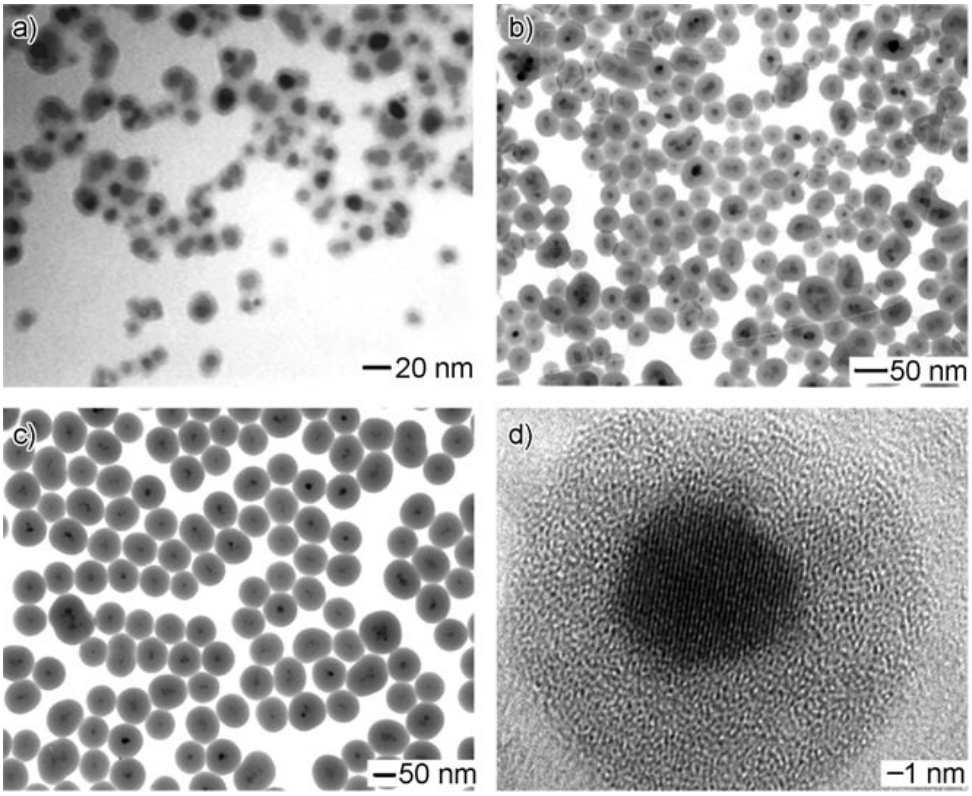

Figure 7. Iron oxide core nanoparticles encapsulated with various thickness of silica shells. By changing the amount of TEOS precursor the thickness of silica shell can be tailored: a) 10, at b) 60, and at c) 1000 mg of TEOS was added into 20 mL of 2-propanol. d) An image showing an iron oxide core nanoparticle in a 6 nm silica shell was taken from the reference. [89]

The synthesis of magnetic cobalt nanoparticle encapsulated in amorphous silica shell was reported by Kobayashi *et al.* [96] Their method utilized 3-aminopropyl trimethoxysilane and TEOS as the silica precursors which were pre-dissolved in aqueous ethanolic solution.

It is interesting to note that an uniform magnetic iron core of 270 nm encapsulated in mesoporous silica shell was for the first time reported by Shi and co-workers.[97] The method involved the use of the Stöber process to prepare the silica coating on hematite nanoparticle. The mesoporous silica was produced from the controlled sol-gel polymerization of TEOS and *n*-octadecyltrimethoxysilane. Hydrogen was used to reduce the iron oxide to metallic iron.

Despite the fact that a considerable progress has been made in the silica encapsulation of magnetic nanoparticle, controlling the thickness of silica shell still remains a key challenge. Micro-emulsion method was particularly explored,[98] which was claimed to give controlled thickness of silica shell from 1.8-30 nm on the surface of Fe_2O_3 nanoparticles.[99] The synthesis of monodispersed α-Fe nanoparticles encapsulated in silica was reported by Tartaj *et al.*, which was found to be air stable. The 50 nm magnetic nanoparticles clearly exhibited superparamagnetic behaviour. The synthetic procedure involved the synthesis of iron oxide in silica by the reverse micro-emulsion process and then the encapsulated iron oxide was reduced to α-Fe by hydrogen at 450 ^{o}C.[100] Other magnetic nanoparticles including $CoFe_2O_4$ and $MnFe_2O_4$ were successfully coated with silica shells using a similar synthetic approach by the reverse micro-emulsion method.[101]

On the other hand, the synthesis of other reactive metal cores encapsulated by silica shells by reduction from their respective metal oxides is more challenging. This is due to the fact that the reactive metal cores such as cobalt or chromium can sometimes be readily oxidized by oxygen present in the solution. As a result, the use of additive(s) to provide a “vitreophilic” (glasslike) surface appeared to be crucial.[102] Nevertheless, relatively non-reactive precious metal cores such as gold, silver, platinum and palladium were demonstrated to be stable in silica shells.[103] Mild oxidation at the surface of magnetic cobalt nanoparticles developed by Bönnemann *et al*. was an acceptable strategy to solve this problem.[52]

Yttria (Y_2O_3) has been claimed to be a very effective protective coat for reactive magnetic nanoparticles. Needle-like YCo-FeOOH nanoparticles can first be prepared by a combination of the carbonate and self-assembly route using electrostatic means. The needle-like nanoparticle can then be used as precursor for the synthesis of FeCo nanoparticle in yttria.[104] This new oxide coated magnetic alloy material gave a very high coercivity value of 1150 Oe.

Although it was fairly easy to synthesise the same alloy core in silica shell using established methods, silica is unstable under basic conditions and its porous nature also allowed oxygen to gain access to the core. As a result, yttria appears to be a more useful coating material to provide protection for the reactive magnetic nanoparticles in alkaline solution.

1.3.5 Carbon coating magnetic nanoparticles

The use of carbon material to encapsulate magnetic nanoparticles has been receiving attention since carbon in particular the graphite structure can give an impermeable protective layer to even the di-hydrogen molecule. In addition, carbon coating has many potential advantages over polymers and silica materials, offering higher thermally and chemically stability and biocompatibility. Also, the discovery of fullerenes rapidly fuelled the interests in the preparation of encapsulated magnetic nanoparticles in these new carbon structures. Carbon coating of magnetic core nanoparticles can be generated by using Kratschmer arc-discharge process.[105] Many metal nanoparticles, including Co, Fe, Ni, Cr, Au, etc. were successfully encapsulated in carbon nanotubes. There are many reported methods for the preparation of carbon coated magnetic particles including arc-discharge, laser ablation, and electron irradiation processes, etc.[106–109] The carbon coating apparently provides effective protection against oxidation, which is crucial for a number of applications.[110]

Air stable cobalt nanoparticles were produced by a sonochemical procedure, as reported by Gedanken and co-workers.[111] The nanoparticles were polydisperse and each of them was coated with a carbon shell. Fe and Fe_3C nanoparticles encapsulated with carbon coating were made by the pyrolysis of iron stearate at 900 ^oC under an

argon atmosphere.[112] Although the carbon encapsulated magnetic nanoparticles were reported to be stable up to 400 ^{o}C in air, they suffered broad particle size distribution ranging from 20-200 nm. In addition, this single-step, direct method in converting salt to metal can be scaled up for mass production. On the other hand, a similar method in the preparation of highly stable cobalt nanoparticles encapsulated with carbon was reported by Lu *et al.* [108] The 11 nm cobalt nanoparticles were coated with poly(furfuryl alcohol). These polymer coated cobalt magnetic nanoparticles was then converted to carbon coated particles by pyrolysis. Using CTAB as an alternative carbon precursor gave imperfect carbon coatings with hollow shells, which can be used as electrodes. The core nanoparticles were leached by rinsing the material in acid solution. Using a related method cobalt nanoparticles can be encapsulated with carbon by the use of poly(styrene-b-4-vinylphenoxy phthalonitrile). These cobalt magnetic nanoparticles gave high saturation magnetic susceptibility value between 95-100 emu/g under ambient temperature for one year.

Recently, it was shown that ion exchangeable polymer can be used to take up a large quantity of cobalt cations. After the thermal treatment of the polymeric material carrying the cobalt ions, the final product contained cobalt nanoparticles entrapped in mesoporous graphitic carbon. The material displayed air stability and ferromagnetic properties for more than 10 months without degradation.[113]

In general, carbon protective layer is prepared from pyrolysis of an organic containing coating. During the high temperature treatment, it often induces particle agglomeration. Thus, the preparation of carbon coated magnetic nanoparticles still remains a major challenge in this field.

1.4 Aim and accomplishment in this thesis

The aim of this project was to explore different synthetic methodologies of magnetic nanoparticles as vehicles to carry functional proteins and drug molecules for various applications. As a result, a number of synthetic methods for the preparation of magnetic nanoparticles or encapsulated magnetic nanoparticles including the uses of controlled precipitation, sol-gel process and the polyol process were studied. In particular, a new methodology of intercalating porous materials, bio-organic species with protein molecules through layer-by-layer deposition was reported. Some of these new nano-structures were demonstrated to store a large amount of protein molecules while maintaining their biological activity in solid form. Application of this method in drug delivery was also studied.

The thesis is structured as follows:

(1) A short review on synthesis, passivation and chemical functionalization of magnetic nanoparticles is presented in Chapter 1.

(2) Preparations of iron oxide magnetic nanoparticles using controlled precipitation and their encapsulation in porous silica are presented in Chapter 2. A new method of placing alternated layers of polyions amine carbohydrate and a blood protein, BSA is described in Chapter 3 which also contains the assessment of the biological activity of the immobilised protein and the possible uses of this new composite material for drug delivery.

(3) Encapsulation of magnetic iron oxide nanoparticles in other porous semiconducting materials and their potential uses are presented in Chapter 4.

(4) Characterisation methods for magnetic metal iron oxide nanoparticles and other related magnetic alloy materials are presented in Chapter 5.

(5) Final Discussion and conclusions of the research in this thesis are presented in Chapter 6.

(6) Chapter 7 of this research enlists the details of the chemicals used in this project.

1.5 References

1. S. C. Tsang, V. Caps, I. Paraskevas, D. Chadwick, D. Thompsett, Angew. Chem., Int. Ed. 2004, 43, 5645-5649.
2. M. C. Daniel, D. Astruc, *Chem. Rev*. **2004**, *104*, 293-346.
3. J. Z. Du, Y. M. Chen, *Angew. Chem. Int. Ed*. **2004**, *43*, 5084-5087.
4. H. L. Li, H. Sun, W. Qi, M. Xu, L. X. Wu, *Angew. Chem. Int. Ed*. **2007**, *46*, 1300-1303.
5. H. Colfen, S. Mann, *Angew. Chem. Int. Ed*. **2003**, *42*, 2350-2365.
6. V. F. Puntes, D. Zanchet, C. K. Erdonmez and A. P. Alivisatos, *J. Am. Chem. Soc*. **2002**, *124*, 12874-12880.
7. T. Y. Kim, W. J. Kim, S. H. Hong, J. E. Kim and K. S. Suh, *Angew. Chem. Int. Ed*. **2009**, *48*, 3806-3809.
8. J. Park, J. Joo, S. G. Kwon, Y. Jang, T. Hyeon, *Angew. Chem. Int. Ed*. **2007**, *46*, 4630-4660.
9. A. M. Cao, J. S. Hu, H. P. Liang, L. J. Wan, *Angew. Chem. Int. Ed*. **2005**, *44*, 4391-4395.
10. B. Fang, N. K. Chaudhari, M. S. Kim, J. H. Kim and J. S. Yu, *J. Am. Chem. Soc*. **2009**, *131*, 15330-15338.
11. H. Y. Liang, H. X. Yang, W. Z. Wang, J. Q. Li, H. X. Xu, *J. Am. Chem. Soc*. **2009**, *131*, 6068-6069.
12. L. E. M. Howard, H. L. Nguyen, S. R. Giblin, B. K. Tanner, I. Terry, A. K. Hughes and J. S. O. Evans, *J. Am. Chem. Soc*. **2005**, *127*, 10140-10141.
13. D. Seo, J. C. Park, H. Song, *J. Am. Chem. Soc*. **2006**, *128*, 14863-14870.
14. B. M. Leonard and R. E. Schaak, *J. Am. Chem. Soc*. **2006**, *128*, 11475-11482.
15. L. C. Varanda and M. Jafelicci, *J. Am. Chem. Soc*. **2006**, *128*, 11062-11066.
16. Y. J. Xiong, J. M. McLellan, J. Y. Chen, Y. D. Yin, Z. Y. Li, Y. N. Xia, *J. Am. Chem. Soc*. **2005**, *127*, 17118-17127.
17. J. Y. Chen, T. Herricks, M. Geissler, Y. N. Xia, *J. Am. Chem. Soc*. **2004**, *126*, 10854-10855.
18. B. Y. Kim, I. B. Shim, Z. O. Araci, S. S. Saavedra, O. L.A. Monti, N. R. Armstrong, R. Sahoo, D. N. Srivastava, J. Pyun, *J. Am. Chem. Soc*. **2010**, *132*, 3234-3235.

19. B. D. Korth, P. Keng, I. Shim, S. E. Bowles, C. Tang, T. Kowalewski, K. W. Nebesny, J. Pyun, *J. Am. Chem. Soc*. **2006**, *128*, 6562-6563.
20. B. Z. Tian, X. Y. Liu, H. F. Yang, S. H. Xie, C. Z. Yu, B. Tu, D. Y. Zhao, *Adv. Mater*. **2003**, *15*, 1370-1374.
21. S. C. Tsang, C. H. Yu, X. Gao, K. Tam, *J. Phys. Chem. B*. **2006**, *110*, 16914-16922.
22. M. J. Hollamby, K. Trickett, A. Mohamed, S. Cummings, R. F. Tabor, O. Myakonkaya, S. Gold, S. Rogers, R. K. Heenan, J. Eastoe, *Angew. Chem. Int. Ed*. **2009**, *48*, 4993-4995.
23. D. E. Moilanen, E. E. Fenn, D. Wong, M. D. Fayer, *J. Am. Chem. Soc*. **2009**, *131*, 8318-8328.
24. C. R. Vestal, Z. J. Zhang, *J. Am. Chem. Soc*. **2002**, *124*, 14312-14313.
25. K. S. Suslick, M. Fang and T. Hyeon, *J. Am. Chem. Soc.*, 1996, **118**,11960.
26. P. Tartaj, M. D. Morales, S. Veintemillas-Verdaguer, T. Gonzalez-Carreno, C. J. Serna, *J. Phys. D- Appl. Phys*, **2003**, *36*, R182-R197.
27. A. G. Roca, R. Costo, A. F. Rebolledo, S. Veintemillas-Verdaguer, P. Tartaj, T. Gonzalez-Carreno, M. P. Morales, C. J. Serna, *J. Phys. D- Appl. Phys*. **2009**, *42*, 224002.
28. J. Kim, J. E. Lee, J. Lee, J. H. Yu, B. C. Kim, K. An, Y. Hwang, C. H. Shin, J. G. Park, J. Kim, T. Hyeon, *J. Am. Chem. Soc*. **2006**, *128*, 688-689.
29. S. Giri, B. G. Trewyn, M. P. Stellmaker, V. S. Y. Lin, *Angew. Chem., Int. Ed*. **2005**, *44*, 5038-5044.
30. T. Sen, A. Sebastianelli, I. J. Bruce, *J. Am. Chem. Soc*. **2006**, *128*, 7130-7131.
31. Q. A. Pankhurst, J. Connolly, S. K. Jones, J. Dobson, *J. Phys. D- Appl. Phys*. **2003**, *36*, R167-R181.
32. X. H. Gao, Y. Y. Cui, R. M. Levenson, L. W. K. Chung, S. M. Nie, Nat. *Biotechnol*. **2004**, *22*, 969-976.
33. J. H. Lee, Y. W. Jun, S. I. Yeon, J. S. Shin, J. Cheon, *Angew. Chem. Int. Ed*. **2006**, *45*, 8160-8162.
34. D. R. Radu, C. Y. Lai, K. Jeftinija, E. W. Rowe, S. Jeftinija, V. S. Y. Lin, *J. Am. Chem. Soc*. **2004**, *126*, 13216-13217.
35. E. Katz, O. Lioubashevski, I. Willner, *J. Am. Chem. Soc*. **2005**, *127*, 3979-3988.

36. S. G. Grancharov, H. Zeng, S. H. Sun, S. X. Wang, S. O'Brien, C. B. Murray, J. R. Kirtley, G. A. Held, *J. Phys. Chem. B.* **2005**, *109*, 13030-13035.
37. C. B. Murray, C. R. Kagan, M. G. Bawendi, Annu. *Rev. Mater. Sci*. **2000**, *30*, 545-610.
38. E. Papirer, P. Horny, H. Balard, R. Anthore, C. Petipas, A. Martinet, *J. Colloid. Interface. Sci*. **1983**, *94*, 207-219.
39. H. Kura, M. Takahashi, T. Ogawa, *J. Phys. Chem. C*. **2010**, *114*, 5835-5838.
40. K. S. Suslick, M. M. Fang, T. Hyeon, *J. Am. Chem. Soc*. **1996**, *118*, 11960-11961.
41. L. E. Euliss, S. G. Grancharov, S. O'Brien, T. J. Deming, G. D. Stucky, C. B. Murray, G. A. Held, *Nano Lett*. **2003**, *3*, 1489-1493.
42. X. Liu, Y. Guan, Z. Ma, H. Liu, *Langmuir*. **2004**, *20*, 10278-10282.
43. R. Hong, N. O. Fischer, T. Emrick, V. M. Rotello, *Chem. Mater*. **2005**, *17*, 4617-4621.
44. Y. Sahoo, H. Pizem, T. Fried, D. Golodnitsky, L. Burstein, C. N. Sukenik, G. Markovich, *Langmuir*. **2001**, *17*, 7907-7911.
45. M. Kim, Y. Chen, Y. Liu, X. Peng, *Adv. Mater*. **2005**, *17*, 1429-1432.
46. N. S. Sobal, M. Hilgendorff, H. Mohwald, M. Giersig, M. Spasova, T. Radetic, M. Farle, *Nano Lett*. **2002**, *2*, 621-624.
47. Q. X. Liu, Z. H. Xu, J. A. Finch, R. Egerton, *Chem. Mater*. **1998**, *10*, 3936-3940.
48. J. Lin, W. L. Zhou, A. Kumbhar, J. Wiemann, J. Y. Fang, E. E. Carpenter, C. J. O'Connor, *J. Solid State Chem*. **2001**, *159*, 26-31.
49. D. K. Kim, M. Mikhaylova, Y. Zhang, M. Muhammed, *Chem. Mater*. **2003**, *15*, 1617-1627.
50. D. L. Peng, K. Sumiyama, T. Hihara, S. Yamamuro, T. J. Konno, *Phys. Rev. B*. **2000**, *61*, 3103.
51. H. G. Boyen, G. Kastle, K. Zurn, T. Herzog, F. Weigl, P. Ziemann, O. Mayer, C. Jerome, M. Moller, J. P. Spatz, M. G. Garnier, P. Oelhafen, *Adv. Funct. Mater*. **2003**, *13*, 359-364.
52. H. Bonnemann, W. Brijoux, R. Brinkmann, N. Matoussevitch, N. Waldofner, N. Palina, H. Modrow, *Inorg. Chim. Acta*. **2003**, *350*, 617-624.
53. S. S. Papell, US Patent 3215572, 1965.
54. R. Massart, *IEEE Trans. Magn*. **1981**, *17*, 1247-1248.

55. K. Raj, R. Moskowitz, *J. Magn. Magn. Mater*. **1990**, *85*, 233-245.
56. M. Decuyper, M. Joniau, *Langmuir*. **1991**, *7*, 647-652.
57. A. Wooding, M. Kilner, D. B. Lambrick, *J. Colloid. Interface. Sci*. **1992**, *149*, 98-104.
58. D. Zins, V. Cabuil, R. Massart, *J. Mol. Liq*. **1999**, *83*, 217-232.
59. R. M. Cornell, U. Schertmann, The Iron Oxides: Structure, Properties, Reactions, Occurrence and Uses, VCH, Weinheim, 1996.
60. M. X. Wan, J. C. Li, *J. Polymer. Sci*. **1998**, *36*, 2799-2805.
61. M. D. Butterworth, S. A. Bell, S. P. Armes, A.W. Simpson, *J. Colloid Interface Sci*. **1996**, *183*, 91-99.
62. P. Tartaj, M. P. Morales, T. Gonzalez-Carreno, S. Veintemillas-Verdaguer, C. J. Serna, *J. Magn. Magn. Mater*. **2005**, *290*, 28-34.
63. G. Barratt, *Cell. Mol. Life Sci*. **2003**, *60*, 21-37.
64. L. A. Harris, J. D. Goff, A. Y. Carmichael, J. S. Riffle, J. J. Harburn, T. G. St Pierre, M. Saunders, *Chem. Mater*. **2003**, *15*, 1367-1377.
65. A. F. Thunemann, D. Schutt, L. Kaufner, U. Pison, H. MPhwald, *Langmuir*. **2006**, *22*, 2351-2357.
66. P. A. Dresco, V. S. Zaitsev, R. J. Gambino, B. Chu, *Langmuir*. **1999**, *15*, 1945-1951.
67. J. G. Deng, X. B. Ding, W. C. Zhang, Y. X. Peng, J. H. Wang, X. P. Long, P. Li, A. S. C. Chan, *Polymer*. **2002**, *43*, 2179-2184.
68. X. L. Xu, S. A. Majetich, S. A. Asher, *J. Am. Chem. Soc*. **2002,** *124*, 13864-13868,
69. X. L. Xu, G. Friedman, K. D. Humfeld, S. A. Majetich, S. A. Asher, *Adv. Mater*. **2001**, *13*, 1681-1684.
70. C. R. Vestal, Z. J. Zhang, *J. Am. Chem. Soc*. **2002**, *124*, 14312-14313.
71. D. Farrell, S. A. Majetich, J. P.Wilcoxon, *J. Phys. Chem. B*. **2003**, *107*, 11022-11030.
72. J. Rivas, R. D. Sanchez, A. Fondado, C. Izco, A. J. Garciabastida, J. Garciaotero, J. Mira, D. Baldomir, A. Gonzalez, I. Lado, M. A. L. Quintela, S. B. Oseroff, *J. Appl. Phys*. **1994**, *76*, 6564-6566.
73. E. E. Carpenter, C. Sangregorio, C. J. O'Connor, *IEEE Trans. Magn*. **1999**, *35*, 3496-3498.
74. J. I. Park, J. Cheon, *J. Am. Chem. Soc*. **2001**, *123*, 5743-5746.

75. Z. H. Ban, Y. A. Barnakov, V. O. Golub, C. J. O'Connor, *J. Mater. Chem.* **2005**, *15*, 4660-4662.

76. Y. S. Shon, G. B. Dawson, M. Porter, R.W. Murray, *Langmuir*. **2002**, *18*, 3880-3885.

77. J. L. Lyon, D. A. Fleming, M. B. Stone, P. Schiffer, M. E. Williams, *Nano Lett*. **2004**, *4*, 719-723.

78. S. J. Cho, J. C. Idrobo, J. Olamit, K. Liu, N. D. Browning, S. M. Kauzlarich, *Chem. Mater*. **2005**, *17*, 3181-3186.

79. H. Yu, M. Chen, P. M. Rice, S. X. Wang, R. L. White, S. H. Sun, *Nano Lett*. **2005**, *5*, 379-382.

80. L. Y. Wang, J. Luo, M. M. Maye, Q. Fan, R. D. Qiang, M. H. Engelhard, C. M. Wang, Y. H. Lin, C. J. Zhong, *J. Mater. Chem*. **2005**, *15*, 1821-1832.

81. D. Caruntu, B. L. Cushing, G. Caruntu, C. J. O'Connor, *Chem. Mater*. **2005**, *17*, 3398-3402.

82. J. Zhang, M. Post, T. Veres, Z. J. Jakubek, J. W. Guan, D. S. Wang, F. Normandin, Y. Deslandes, B. Simard, *J. Phys. Chem. B.* **2006**, *110*, 7122-7128.

83. Z. Guo, C. S. S. R. Kumar, L. L. Henry, C. K. Saw, J. Hormes, E. J. Podlaha, 49th Magnetism and Magnetic Materials (MMM) Annual Conference Proceedings, 2004, S. 366.

84. Z. H. Lu, M. D. Prouty, Z. H. Guo, V. O. Golub, C. S. S. R. Kumar, Y. M. Lvov, *Langmuir*. **2005**, *21*, 2042-2050.

85. V. L. Colvin, A. N. Goldstein, A. P. Alivisatos, *J. Am. Chem. Soc*. **1992**, *114*, 5221-5230.

86. D. L. Ma, J. W. Guan, F. Normandin, S. Denommee, G. Enright, T. Veres, B. Simard, *Chem. Mater*. **2006**, *18*, 1920-1927.

87. W. Stober, A. Fink, E. Bohn, *J. Colloid Interface Sci*. **1968**, *26*, 62-69.

88. T. Tago, T. Hatsuta, K. Miyajima, M. Kishida, S. Tashiro, K. Wakabayashi, *J. Am. Ceram. Soc*. **2002**, *85*, 2188-2194.

89. Y. Lu, Y. D. Yin, B. T. Mayers, Y. N. Xia, *Nano Lett*. **2002**, *2*, 183-186.

90. C. Graf, D. L. J. Vossen, A. Imhof, A. van Blaaderen, *Langmuir*. **2003**, *19*, 6693-6700.

91. A. P. Philipse, M. P. B. Vanbruggen, C. Pathmamanoharan, *Langmuir*. **1994**, *10*, 92-99.

92. A. Ulman, *Chem. Rev*. **1996**, *96*, 1533-1554.
93. M. Ohmori, E. Matijevic, *J. Colloid Interface Sci*. **1992**, *150*, 594-598.
94. M. A. Correa-Duarte, M. Giersig, N. A. Kotov, L. M. Liz-Marzan, *Langmuir*. **1998**, *14*, 6430-6435.
95. M. Ohmori, E. Matijevic, *J. Colloid Interface Sci*. **1993**, *160*, 288-292.
96. Y. Kobayashi, M. Horie, M. Konno, B. Rodriguez-Gonzalez, L. M. Liz-Marzan, *J. Phys. Chem. B*. **2003**, *107*, 7420-7425.
97. W. R. Zhao, J. L. Gu, L. X. Zhang, H. R. Chen, J. L. Shi, *J. Am. Chem. Soc*. **2005**, *127*, 8916-8917.
98. S. Santra, R. Tapec, N. Theodoropoulou, J. Dobson, A. Hebrad, W. H. Tan, *Langmuir*. **2001**, *17*, 2900-2906.
99. D. K. Yi, S. S. Lee, G. C. Papaefthymiou, J. Y. Ying, *Chem. Mater*. **2006**, *18*, 614-619.
100. P. Tartaj, C. J. Serna, J. Am. Chem. Soc. 2003, 125, 15754-15755.
101. C. R. Vestal, Z. J. Zhang, *Nano Lett*. **2003**, *3*, 1739-1743.
102. L. M. LizMarzan, M. Giersig, P. Mulvaney, *Chem. Commun*. **1996**, 731-732.
103. T. Ung, L. M. LizMarzan, P. Mulvaney, *Langmuir*. **1998**, *14*, 3740-3748.
104. N. O. Nunez, P. Tartaj, M. P. Morales, P. Bonville, C. J. Serna, *Chem. Mater*. **2004**, *16*, 3119-3124.
105. J. H. J. Scott, S. A. Majetich, *Phys. Rev. B*. **1995**, *52*, 12564-12571.
106. K. H. Ang, I. Alexandrou, N. D. Mathur, G. A. J. Amaratunga, S. Haq, *Nanotechnology*. **2004**, *15*, 520-524.
107. W. Teunissen, F. M. F. de Groot, J. Geus, O. Stephan, M. Tence, C. Colliex, *J. Catal*. **2001**, *204*, 169-174.
108. T. Hayashi, S. Hirono, M. Tomita, S. Umemura, *Nature*. **1996**, *381*, 772-774.
109. R. Nesper, A. Ivantchenko, F. Krumeich, *Adv. Funct. Mater*. **2006**, *16*, 296-305.
110. H. B. S. Chan, B. L. Ellis, H. L. Sharma, W. Frost, V. Caps, R. A. Shields, S. C. Tsang, *Adv. Mater*. **2004**, *16*, 144-149.
111. S. I. Nikitenko, Y. Koltypin, O. Palchik, I. Felner, X. N. Xu, A. Gedanken, *Angew. Chem. Int. Ed*. **2001**, *40*, 4447-4449.
112. J. F. Geng, D. A. Jefferson, B. F. G. Johnson, *Chem. Commun*. **2004**, 2442-2443.

113. A. H. Lu, W. C. Li, E. L. Salabas, B. Spliethoff, F. Schuth, *Chem. Mater*. **2006**, *18*, 2086-2094.

Chapter Two

Immobilization of BSA on Silica Coated Magnetic Iron Oxide Nanoparticles

Contents

2.1 Overview

Colloid stable magnetic iron oxide nanoparticles, which undergo reversible precipitation from aqueous solution with external magnetic field, have many potential applications. However, one of the key problems has been the lack of generic homogeneous anchoring sites on the magnetic nanoparticle's surface for binding of chemical/biochemical species. Here, it is demonstrated that iron oxide nanoparticle encapsulated in a silica shell can offer a specific binding site to a protein molecule without severe denaturing of the structure. This can be achieved *via* an electrostatic interaction with the surface silanol groups. As a result, a high loading of Bovine Serum Albumin (BSA) can be anchored onto the silica encapsulated iron oxide. FTIR, circular dichroism and binding constant (using site I and site II drugs) measurements all indicate only a small degree of conformational alteration in the BSA upon immobilization onto this magnetic material. A partial unfolding of the secondary structure on external sheath of the protein due to competitive hydrogen bonding interactions with surface acidic hydroxyl groups is shown to take place. This slight structural modification is in a sharp contrast to the severe blockage of the drug binding site in anchored BSA by extended silica surface.[(1)] Nevertheless, our results clearly suggests that the internal hydrophobic sites I and II of the immobilized BSA on the silica-based magnetic nanoparticle still remain intact and functional for specific drug molecule bindings.

2.2 Introduction

The application of magnetic nanoparticles is not only taken place in electrical, optical and magnetic areas, but also some new areas including magnetic assisted bio-separation and bio-catalysis. As a result, a number of protein-conjugated magnetic nanoparticles have recently been used in some new biotechnology areas.[2-4] In biomedicine, magnetic nanoparticles can be used as recoverable labeling or imaging reagents when tagged with biological entities.[5] These approaches are attractive to industry as the valuable tagged bio-molecules can be magnetically recycled from solution, thus minimizing waste production through regeneration.[6] However, the lack of generic homogeneous anchoring sites on nanoparticle surface for selective binding of chemical/biochemical species, whilst maintaining the native structure under a wide range of conditions is one key problem. For example, a clear correlation has been found between the affinity of proteins for surface with the extent of their structural changes.[7] Most proteins generally show a higher affinity to hydrophobic surfaces which could also lead to higher degree of protein denaturation.[8] Also, a nanoparticle surface may or may not take up a particular protein, which depends on the match of their isoelectric points in a rather narrow pH range. It has also been observed that an increase in electrostatic interaction is always accompanied with a certain extent of alternation in the native structure.[9]

A single-step solution based method on the synthesis of iron oxide nanoparticle encapsulated in a thin coating of silica using micro-emulsion technique has been reported.[10] In this chapter, we report *for the first time* the activity-structure evaluation of immobilized bovine serum albumin (BSA) on this nano magnetic body. We believe that two important aspects can be obtained from this study. First, the interactions between biological species and magnetic supports have not fully investigated in the literature and thus the study of BSA immobilization onto silica coated magnetic support is regarded to be important as a model. Secondly, the pharmaceutical industry has routinely determined the fraction of drug binds to plasma albumin, and the binding constant in order to assess the free drug concentration *in vivo*. Equilibrium dialysis is one of the established protocols for this purpose.[11]

However, this procedure is slow and inefficient. Therefore, one important aspect of studying this present system is to develop an alternative analytical system for binding constant evaluation using magnetic separation for the industry.

BSA has been long regarded as the model for human serum albumin. BSA is a major protein constituent of bovine blood plasma that can bind to various drug species as endogenous and exogenous ligands. Its drug binding properties are rather complicated, which include hydrophobic and electrostatic as well as hydrogen bonding interactions. In the context of pharmaceutical research, it is generally believed that the plasma albumin serves as a depot and transport protein to help the distribution of drug in the systemic circulation to the target biological site, while the free fraction of drug drives the pharmacological response. As a result, the binding ability to albumin critically affects the pharmacokinetic and pharmacological behaviours of a particular drug compound.[12-15] The structure of BSA consists of three repeating domains, which can be further divided into two sub-domains (named I-III with A and B). Hydrophilic moieties are located on the protein surface, where the more hydrophobic residues are generally located in the interior of the protein molecule.[1] The serum albumin of repeating subdomain IA, IIA, IIIA creating internal hydrophobic sites I and II for binding drug compounds have been extensively studied by X-ray crystallography.[16,17] Herein, the activity-structure of immobilized bovine serum albumin (BSA) protein on this nano magnetic body is investigated by various methods.

2.3 Experimental Section

2.3.1 Synthesis of silica encapsulated Fe_3O_4 nanoparticles

According to our reported methodology 7.3 g CTAB, shown in figure 1, was added into 180 mL dried toluene in a 250 mL round bottom flask with stirring for 4 h. In general, the higher mole ratio of water to surfactant (Wo value) used, the larger of the nanoparticles size we observed.[9] In this case, the Wo = [water]/[CTAB] of 20 was fixed. Thus, solution containing Fe(II)/Fe(III) salts, 0.3428 g of $FeCl_2.4H_2O$ (1.724

mmol) and 0.9321 g of $FeCl_3.6H_2O$ (3.448 mmol), pre-dissolved in 7.2 mL deionized water was added drop-wise into the bottom flask constantly flushed with nitrogen for 2h. After four hours, 8 mL of diluted ammonium hydroxide solution (5 % w/w) was added dropwise to the same flask with a continuous nitrogen purge. The color was gradually changed from light yellow to dark brown but without precipitation. At this point, 6.951 g TEOS, as shown in figure 2, was directly added into the micro-emulsion and the mixture was allowed to age for 5 days to encourage hydrolysis and condensation of the silica precursor. After aging, the resulting nanoparticles were collected as a precipitate when ethanol was added into the solution. The precipitate was then washed with excess ethanol and re-dispersed in toluene. This step was repeated for five times in order to remove the surfactant from the precipitate (until the FTIR showed no trace of the surfactant). At last, the precipitate was washed with acetone and left in air for drying at room temperature overnight. The formation of iron oxide nanoparticle from the chemical reaction of ammonium hydroxide with Fe(II)/Fe(III) species is shown according to equation (1) and then followed by silica encapsulation from controlled hydrolysis of TEOS according to equation (2). Figure 3 presents a schematic summary of the preparative procedure.

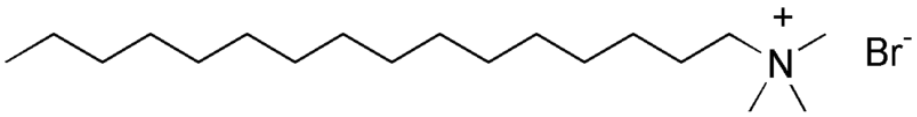

Figure 1. Shows cetyltrimethylammonium bromide (CTAB).

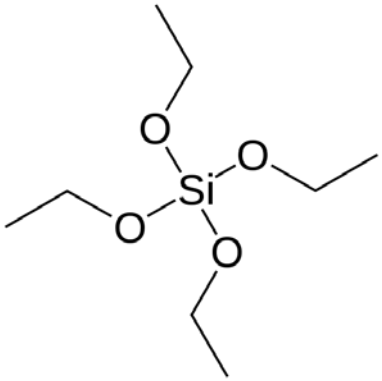

Figure 2. Shows tetraethyl orthosilicate (TEOS).

$$Fe^{2+}_{(aq)} + 2Fe^{3+}_{(aq)} + 8OH^{-}_{(aq)} \rightarrow Fe_3O_{4(s)} + 4H_2O_{(l)} \quad (1)$$

$$Si(OEt)_{4(l)} + H_2O_{(l)} \rightarrow Si(OH)_{4(s)} \rightarrow SiO_{2(s)} + 2H_2O_{(l)} \quad (2)$$

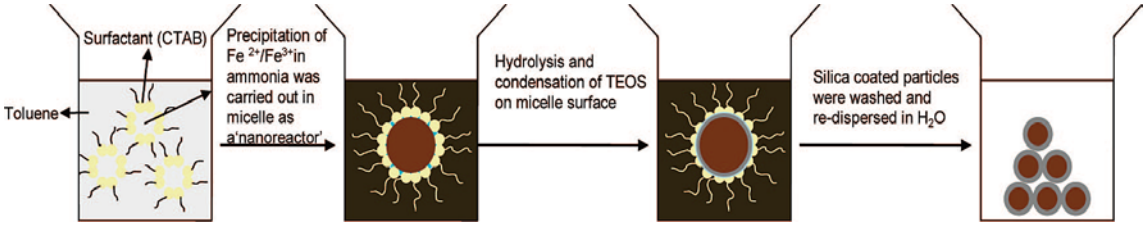

Figure 3. Synthetic procedure for preparing silica-encapsulated iron oxide nanoparticles.

2.3.2 Experimental procedure for constructing BSA calibration curves

0.0500 grams of BSA was weighed in 50 ml volumetric flask. Approximately 10 ml of phosphate buffer at pH 7.4 was added to dissolve the BSA powder into clear solution. A further phosphate buffer was added to the 50 ml mark to make up 1 mg/ml BSA stock solution. 2.5 ml aliquot of BSA stock solution was transferred to 10 ml disposable glass vials, each diluted at different volumes. The absorbance of each diluted solution was taken against a reference cell containing phosphate buffer at pH 7.4. Thus, the BSA absorption peaks at different concentrations are shown in figure 4 with the straight line plot of the concentration against absorbance in the inset graph.

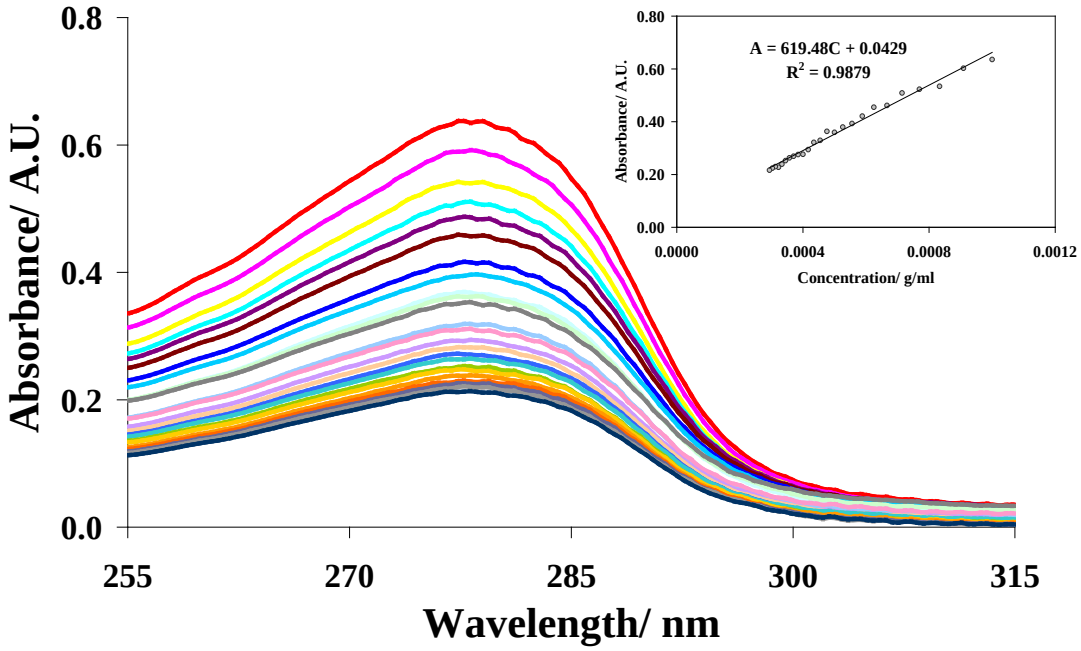

Figure 4. Absorption peak for BSA at 278 nm wavelength at different concentrations, the plot of concentration against absorption gives a straight line in the inset graph.

2.3.3 Experimental procedure for constructing ibuprofen calibration curves

0.0500 grams of ibuprofen was weighed in 50 ml volumetric flask. Approximately 10 ml of phosphate buffer at pH 7.4 was added to dissolve the ibuprofen powder into clear solution. A further phosphate buffer was added to the 50 ml mark to make up 1 mg/ ml ibuprofen stock solution. 2.5 ml aliquot of ibuprofen stock solution was transferred to 10 ml disposable glass vials, each diluted at different volumes. The absorbance of each diluted solution was taken against a reference cell containing phosphate buffer at pH 7.4. Thus, the ibuprofen absorption peaks at different concentrations are shown in figure 5 with the straight line plot of concentration against absorbance in the inset graph

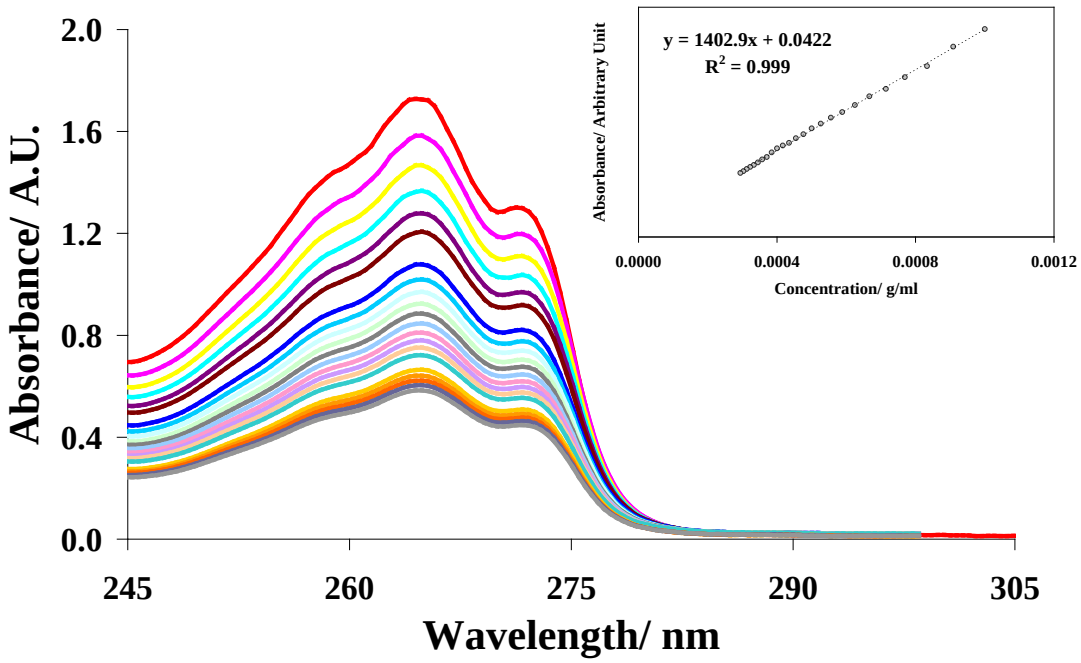

Figure 5. Absorption peak for ibuprofen at 273 nm wavelength at different concentrations, the plot of concentration against absorption gives a straight line in the inset graph.

2.3.4 Experimental procedure for constructing warfarin calibration curves

0.0017 grams of warfarin was weighed in 100 ml volumetric flask. Approximately 10 ml of phosphate buffer at pH 7.4 was added to dissolve the warfarin powder into clear solution. A further phosphate buffer was added to the 100 ml mark to make up 0.017 mg/ml warfarin stock solution. 2.5 ml aliquot of warfarin stock solution was transferred to 10 ml disposable glass vials, each diluted at different volumes. The absorbance of each diluted solution was taken against a reference cell containing a phosphate buffer at pH 7.4. Thus, the warfarin absorption peaks at different concentrations are shown in figure 7 with the straight line plot of concentration against absorbance in the inset graph.

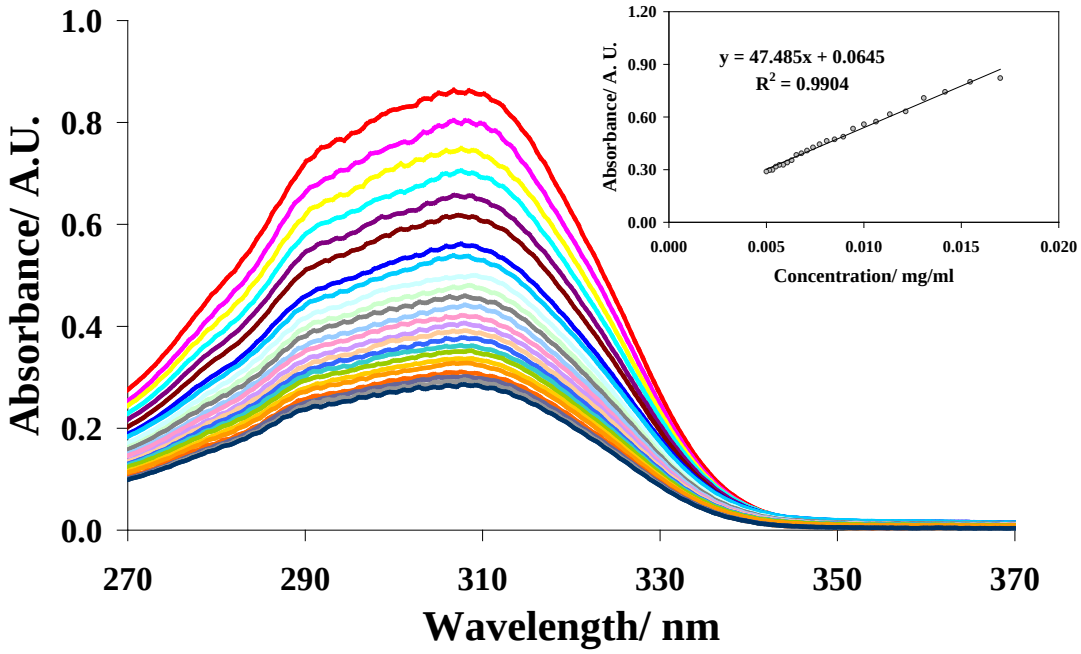

Figure 7. Absorption peak for warfarin at 306 nm wavelength at different concentrations, the plot of concentration against absorption gives a straight line in the inset graph.

2.3.5 Material Characterization

All the synthesized nanoparticles were collected, washed and characterized with various techniques, such as BET Surface Area and Pore volume determination using nitrogen, Powder X-ray diffraction (XRD), Transmission electron microscopy (TEM), Energy Dispersive X-ray Spectrometry (EDS), Fourier Transform Infra-Red Spectroscopy (FTIR), Circular Dichroism, CD and Vibration Sample magnetization (VSM). The VSM studies were carried out using VSM Model 4500, Princeton Applied Research equipped with a 7000 Oe electromagnet and FTIR spectroscopy was obtained using the Perkin-Elmer 1720-X. The CD measurements to reflect conformations of native and immobilized BSA were carried out using the Jasco J-810 spectropolarimeter. The XRD patterns were obtained using a Siemens D5000 X-ray diffractometer. The data was collected in Debye-Scherrer geometry using a monochromated X-ray beam of Cu kα radiation (λ= 1.5406Å). Also, XRD were used to estimate the average particle size using the Debye-Scherrer equation:

$$l = \frac{k\lambda}{\beta \cos\theta} \qquad \textbf{(3)}$$

where l is the thickness of the crystal, k is the Debye-Scherrer constant (0.9), λ is the X-ray wavelength and ß is the line broadening in radians obtained from the full width at half-maximum. It could be obtained by $ß^2 = ß_M^2 - ß_S^2$ where $ß_S$ is the full width at half-maximum of a standard material and $ß_M$ is the measured full width at half-maximum of the material. θ is the Bragg angle. The lower limit of detection occurs when the peaks become so broad that they disappear into the background. Normally, for those crystals with a thickness of 50 to 500Å, the line broadening is easily detected and measured.

The silica coated magnetic nanoparticles were characterized by Transmission Electron Microscopy (TEM) using a FEI /Philips CM 20 instrument. The samples were prepared by placing a drop of colloidal dispersion of the nanoparticles in isopropanol onto a carbon-coated copper grid, followed by natural evaporation of the solvent. Native BSA (schematics, shown in figures 8-10) and immobilized BSA on the surface of magnetic nanoparticles were investigated by ATR-IR**.** The spectra were acquired using a Nicolet 6700 ATR-IR spectrometer with a liquid-nitrogen-cooled MCT detector. A small drop of test sample was placed on smart golden gate-ZeSe/diamond crystal surface and evaporated at room temperature. The spectra were obtained by averaging 128 scans with a resolution of 4 cm^{-1} over the wavenumbers ranging from 650 to 4000 cm^{-1}. The region between 1500- 1900 cm^{-1} containing Amide I and Amide II of BSA were key importance.

Sodium dodecyl sulphate polyacrylamide gel electrophoresis (SDS-PAGE) was used to compare the molecular weight of native BSA and immobilised BSA based on a standardised procedure, which could reflect the interaction(s) between the BSA and the magnetic nanoparticles. The BSA samples were therefore prepared with and without the magnetic support: they were mixed with concentrated loading buffer and incubated at 95 °C for 5 minutes to ensure denaturation of the BSA. Adequate β-mercaptoethanol was added to reduce the denature protein. The samples were then loaded on a commercial 10% NuPAGE Bis-Tris gel (Invitrogen) and separated by

electrophoresis at 200 volts for 35 minutes along with protein markers in MES buffer. Coomassie brilliant blue R-250, shown in figure 11, was used to stain the protein. The gel was carefully removed by separating the two glass plates and subjected to 100 ml staining solution. The staining solution contained 100 mg Coomassie brilliant blue R-250, 100 mg $CuSO_4$, 15 ml methanol, 10 ml glacial acetic acid and 75 ml deionised water. The gel was left to stain overnight with constant agitation. The gel was destained to remove excess dyes by immersing the gel in a 100 ml destining solution containing 10 ml glacial acetic acid, 50 ml methanol and 40 ml deionised water overnight with constant agitation. Blue protein bands were clearly seen against clear background and a photograph was taken for analysis.

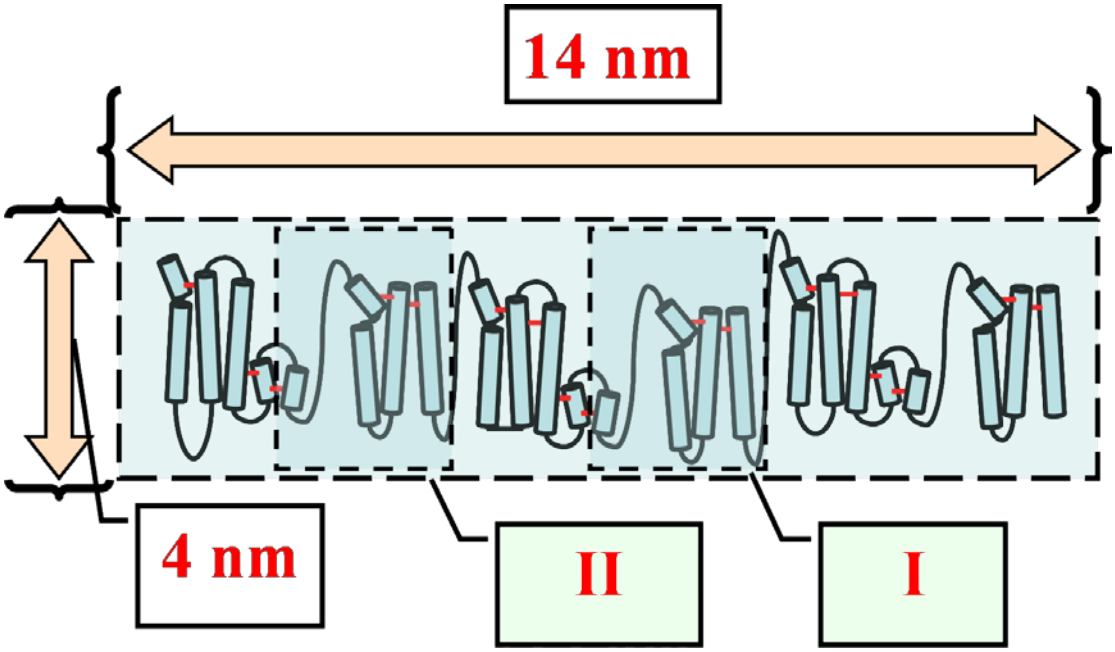

Figure 8. Shows the dimension size of BSA (4 nm × 14 nm) and the location of binding sites, (I) site I and (II) site II.

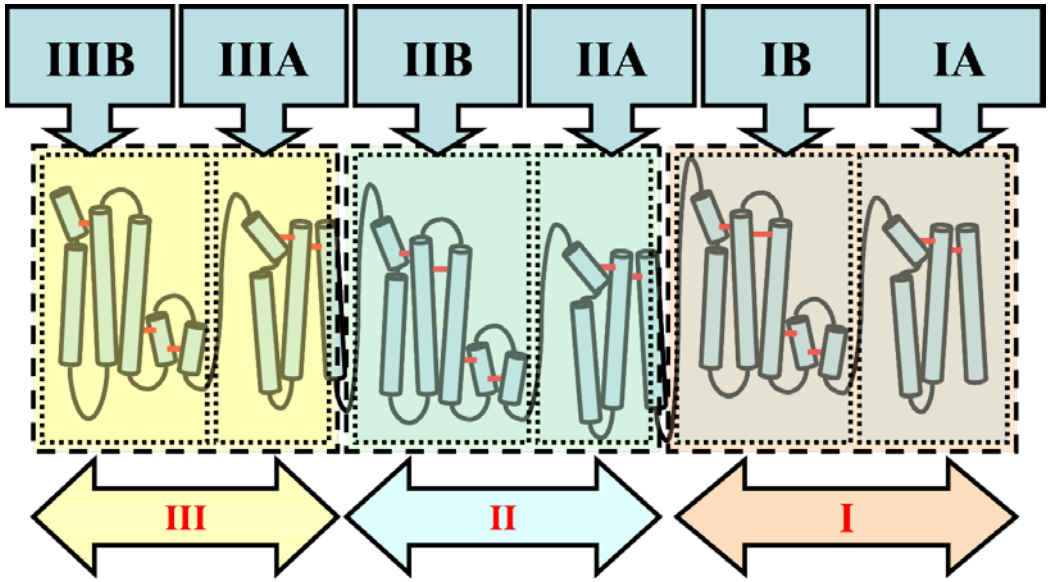

Figure 9. Shows the whole molecule of the BSA with repeated identical domains I) domain I, II) domain II and III) domain III. Each domain can be further divided to IA) and IB) subdomain A and B in domain I, IIA) and IIB) subdomain A and B in domain II, and IIIA) and IIIB) subdomain A and B in domain III respectively.

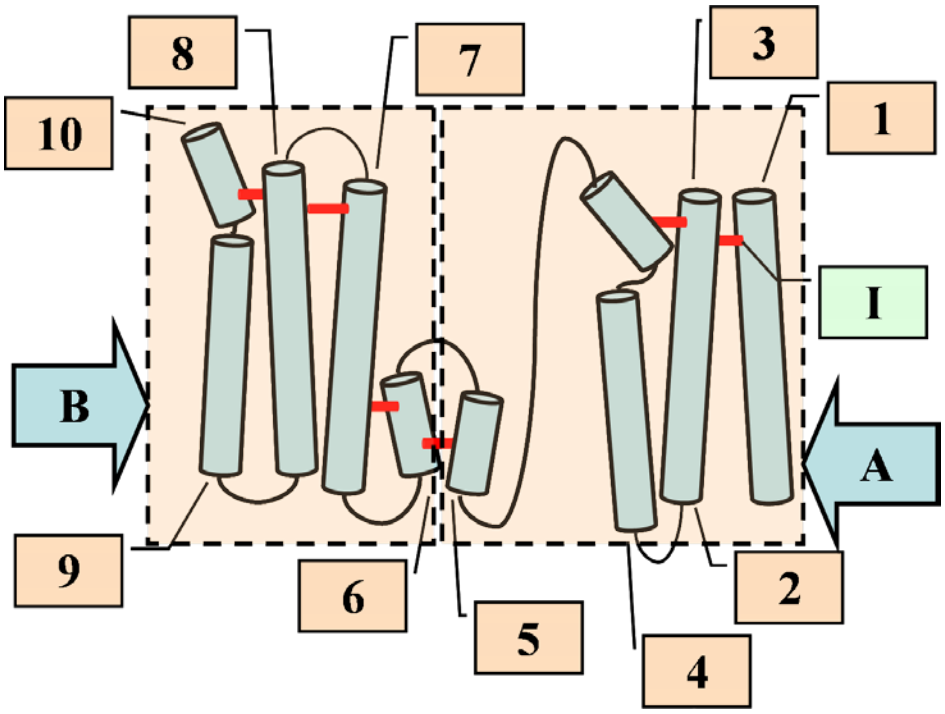

Figure 10. Shows the schematic structure of one repeated domains of BSA which consist of 1-10) principle helices 1-10 separated by I) S-S bond, with A) sub-domain A and B) sub-domain B.

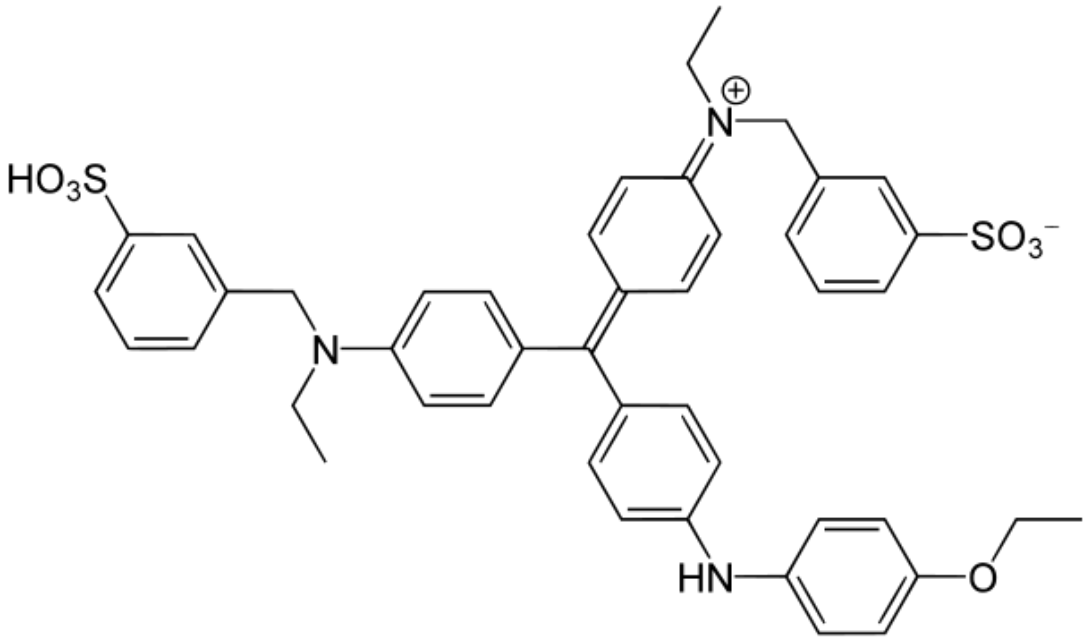

Figure 11. Coomassie brilliant blue R-250.

Zeta potential indicates the surface charge of a material at different pH and represents the value of electrostatic potential at the interface between Stern and diffuse layers. The zeta potential ζ (mV) which expresses the stability of a particle liquid mixture is calculated from the electrophoretic mobility ν_{ε}

$$\zeta = \frac{4\pi\eta\nu_{\varepsilon}}{D} \qquad \textbf{(4)}$$

Where η is the liquid viscosity and D is the dimensionless dielectric constant of the liquid.

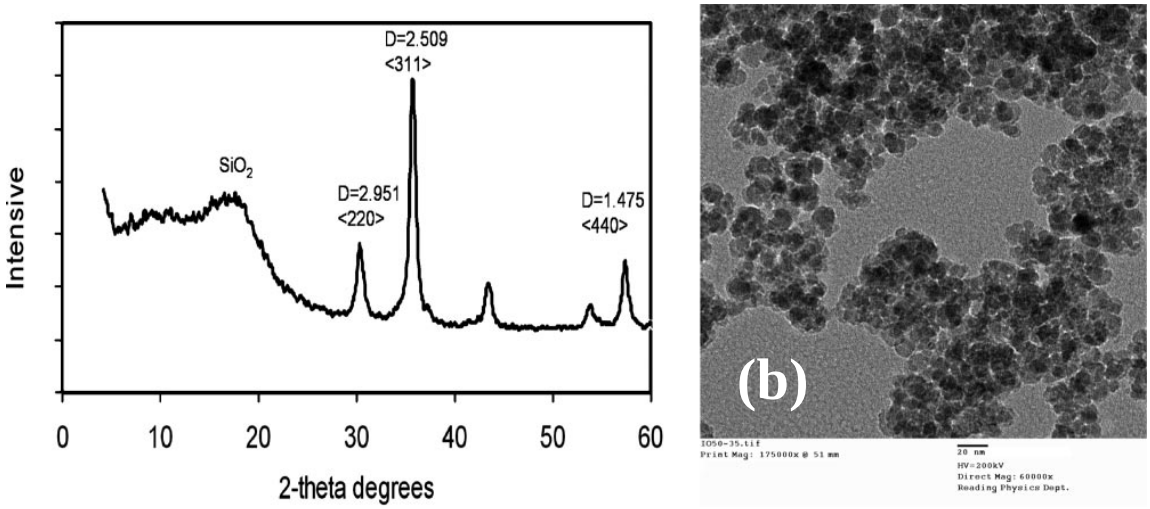

Figure 12. (a) X-ray diffraction pattern of Fe_3O_4 encapsulated in amorphous silica; (b) a typical low-resolution transmission electron image of the core-shell spherical morphology.

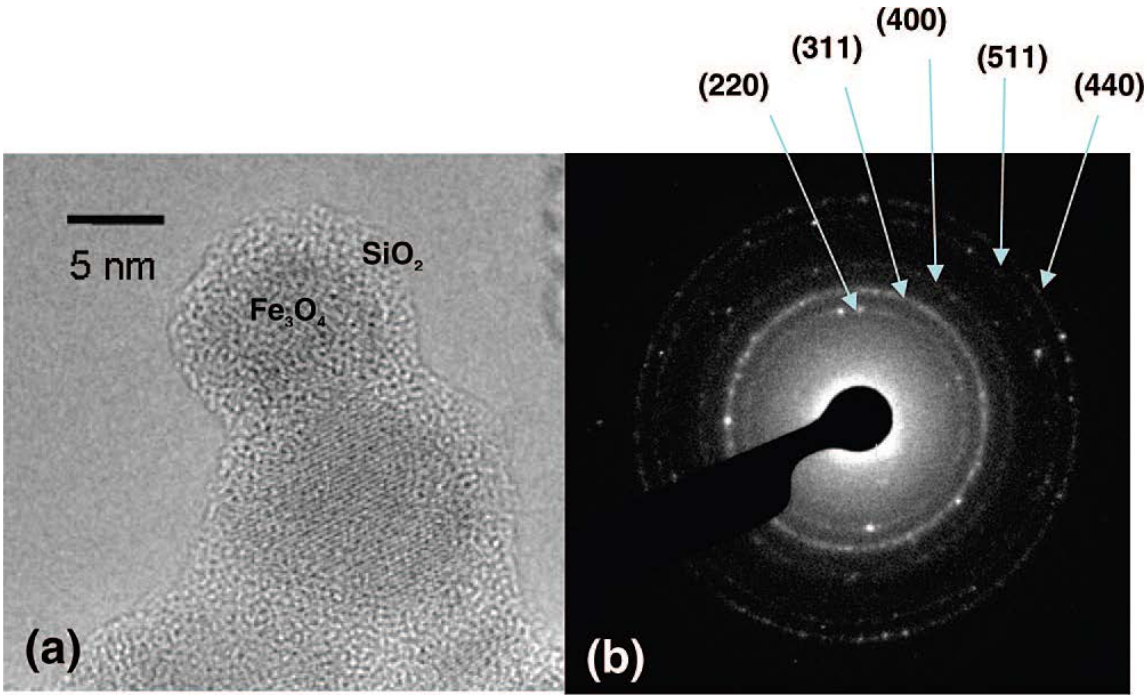

Figure 13. Panels (a) and (b) show high resolution transmission electron micrograph of the silica encapsulated iron oxide nanoparticles (fringe separation of 2.5 ± 0.1 Å of <311> Fe_3O_4 can be clearly visible) and corresponding SAED.

The zeta potential of silica, BSA and silica encapsulated magnetic materials with and without BSA were measured in order to investigate their surface properties. The samples were prepared in various buffered pH solutions at around pH = 1.5-11. The zeta potentials were measured using a Malvern Zeta Master. The measurement of the electrophoretic mobility of the colloidal suspension was used by a helium-neon laser light source in the Malvern instrument. Two coherent beams of red light crossed at the stationary level in the capillary cell with the sample suspension. The particles fluctuated in the applied field. The frequency of the fluctuations of the light scattered was related to the speed of the particles. The scattered light passing through the photomultiplier was analysed by a digital correlator. The frequency component was extracted from the particle mobility.

2.4 Results and Discussion

X-ray Diffraction (XRD) pattern of iron oxide in silica displays three strong peaks corresponding to lattice spacings of 2.951, 2.509, and 1.475 Å (Figure 12a). The peaks matched well with either Fe_3O_4 or γ-Fe_2O_3 phases as compared to the literature. However, assignment to one of these phases (or both) based entirely on XRD is difficult because of similar patterns and peak broadening due to their nano-metric dimension. The particle size was calculated at 7.69 nm using Debye-Scherrer equation from the full width at half maximum (FWHM) of the strongest peak. This was consistent with similar values obtained from TEM (Figure 12b). It was noted that a very broad diffraction hump on the XRD from 9-23^o (2θ) was assigned to amorphous silica. Figure 13a shows a typical high resolution transmission electron microscopic (HRTEM) image of the silica encapsulated iron oxide nanoparticles. The images suggest their size can be successfully tailored by water/surfactant molar ratio. It was observed that the image indeed revealed the highly crystalline structure of the iron oxide core (with a lattice spacing of 2.5± 0.1 Å corresponding to the <311> of Fe_3O_4 in the highly crystalline structure) in an amorphous coating. The selected area electron diffraction patterns (SAED) of the material shown in Figure 13b also agreed with those from XRD.

Figure 4a displays the elemental analysis (EDS) of the isolated particles of the silica encapsulated iron oxide. After taking the correction of the response factor for each element into account, the atomic ratios of the particle was found to be Fe : O : Si = 19.93 : 71.96 : 8.11 with a standard deviation of ± 0.2 %. (excluding carbon analysis because of the use of carbon filmed holder which also affects the oxygen analysis). Hence, the percentage of silica content was less than the iron content. A thin silica with amorphous matrix was observed to surround each core of iron oxide and most of particles were almost spherical (see Figures 12 and 13). Figure 14b showed the porous nature of the particles in the nitrogen BET surface area measurement. According to the Brunauer's classification, a typical type II isotherm was observed at 77 K with a surface area of 123 m^2/g and a pore volume of 0.37 cm^3/g.

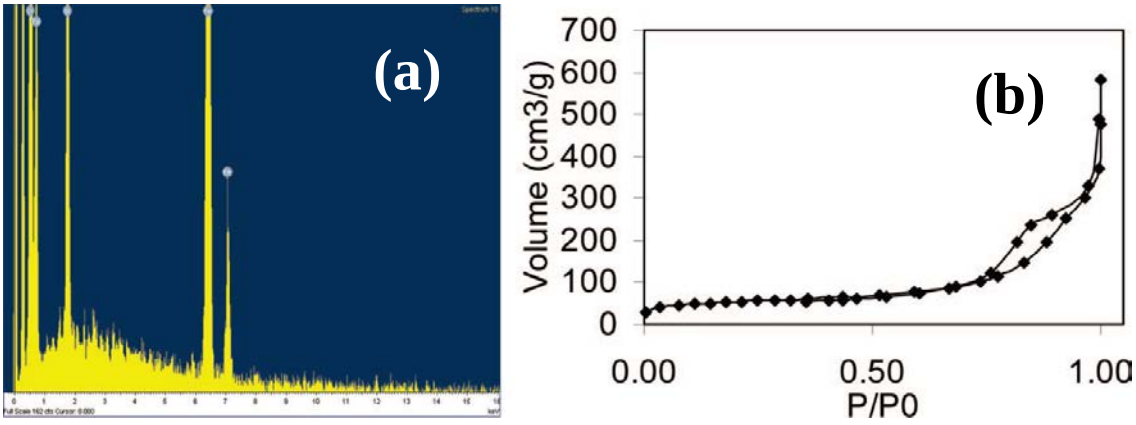

Figure 14. (a) Elemental analysis of the isolated particles of the silica encapsulated iron oxide by EDS. After taking the correction of the response factor for each element into account, the atomic ratios of the particle are found to be Fe/O/Si 19.93:71.96:8.11, with a standard deviation of 0.2%. (excluding carbon)); (b) N_2 adsorption/desorption isothermals.

Figures 15a and 15b showed the general and enlarged vibration saturation magnetization (VSM) responses of the silica encapsulated iron oxide nanoparticle powder upon various external magnetic fluxes. It was evident that the powdered material showed no magnetic hysteresis with both the magnetization and demagnetization curves passing through the origin, which clearly indicated the super-

paramagnetic nature of the material. This means that the magnetic material can only be aligned under an applied magnetic field but will not retain any residual magnetism upon removal of this field. Thus, this silica coated nanoparticle is suitable for repeated magnetic separation purposes.

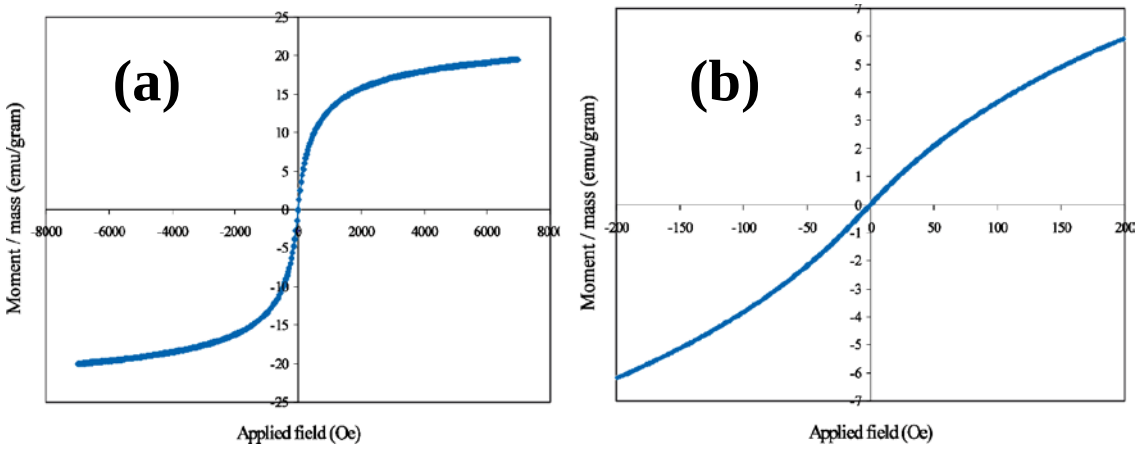

Figure 15. Left (a) and right (b) showed general and enlarged VSM responses, respectively, of the silica-encapsulated iron oxide nanoparticle powder upon application of increasing external magnetic flux. The measurements were collected at room temperature.

The absorption of BSA was studied by placing silica coated iron oxide nanoparticles of different quantities into different batches of 4 mL of 47.31µM of BSA solutions at pH 7.4. The suspensions were placed on a roller at room temperature for 3 h to reach adsorption equilibrium. The amount of BSA adsorbed was expressed in term of concentration loss in total volume 4 mL solution (Figure 16a). Different batches of silica-coated magnetic particles gave an average of 85 mg BSA/g of carrier as shown in Figure 16b, a value is similar to those reported using related nano materials.[18] The amount of BSA adsorbed was calculated by means of mass different of excess BSA deducted from its initial. The mass of BSA was calculated from its volume and concentration, in which these were calculated from its absorbance using its calibration curve shown in figure 4.

Figure 16b showed the amount of BSA adsorbed decreases non-linearly with increasing amount of silica encapsulated iron oxide nanoparticles. This was due to the different orientation of the BSA molecules at different concentrations. At high relative concentration of BSA, the molecules adopt end on end orientation where more BSA can be adsorbed onto the surface of silica. Upon further addition of silica encapsulated nanoparticles, the relative concentration of BSA decreases, where there are few BSA molecules remaining for adsorption and so side by side orientation is favoured which occupy larger surface area per molecule, allowing less number of BSA molecules to be adsorbed for a given surface area.

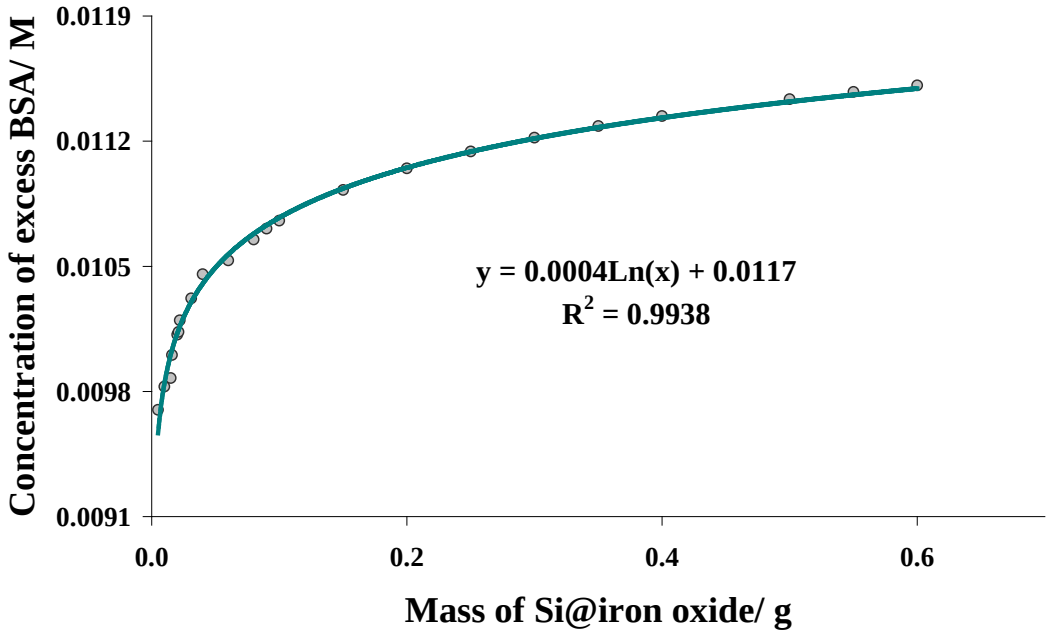

Figure 16a. Adsorption BSA on silica encapsulated iron oxide expressed in terms of an excess of BSA retained after treatment with strong correlation coefficient value.

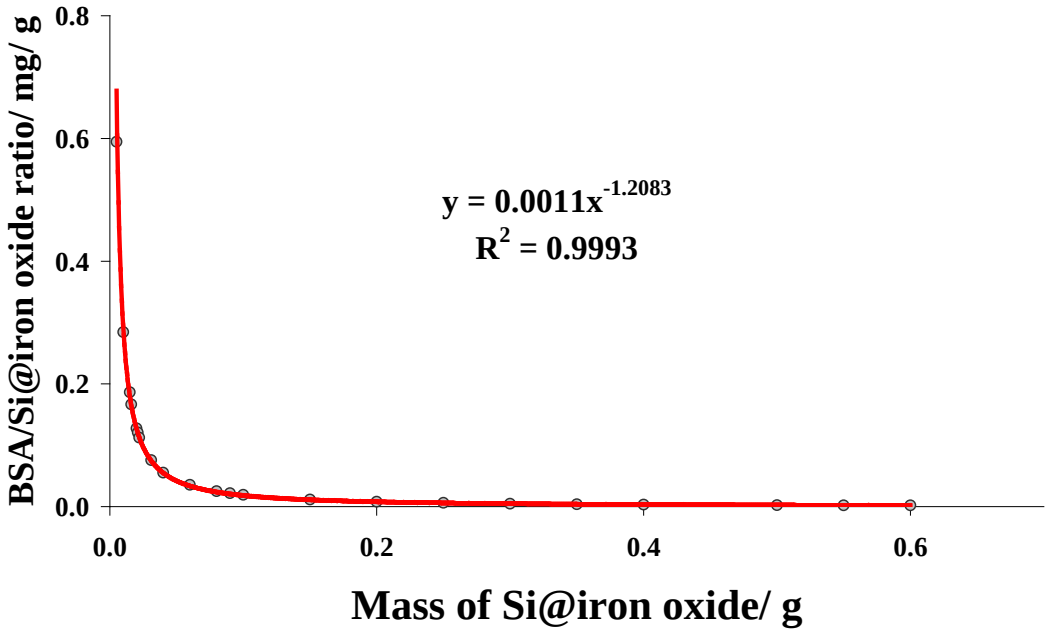

Figure 16b. Varying the amount of BSA adsorbed per gram of silica encapsulated iron oxide when treated with different amount of silica encapsulated iron oxide before equilibration.

It is well known that the isoelectric point (IEP) of iron oxide such as γ-Fe_2O_3 is around 8, which exerts little electrostatic interaction with protein (unable to fix biological species upon the oxide surface) at neutral pH.[18] On the other hand, hydrolytic silica with acidic surface hydroxyl groups, shows IEP between 2-3. The zeta potential of the iron oxide in silica shown in Figure 17a indeed confirmed the IEP at or below 3, clearly indicates the embracement of iron oxide surface by silica.

Figure 17b shows that IR studies of the silica coated iron oxide nanoparticle with and without the BSA attachment. Peaks at 796, 890, 960 and 1074 cm^{-1} were assigned to symmetric and asymmetric stretching vibrations of the terminal group of Si-O-R or Si-OH and the peak at 452 cm^{-1} is assigned to Si-O-Si. Both spectra showed an absorption peak near 960 cm^{-1}, which suggests the presence of hydroxyl groups (υ -OH). Another vibration mode of the hydroxyl group (υ O-H, a broad peak at 3460cm^{-1}) was also recorded which is thought to facilitate attachment of the protein onto silica surface.[19] It is interesting to note that the hydroxyl peaks shifted towards lower

wave-numbers without much attenuation upon the surface attachment of the protein. This suggests the surface hydroxyl groups interacts with the protein primarily through hydrogen bonding and electrostatic interactions. However, the possibility of a small degree of hydrogen bonding between the hydroxyl groups with the terminal amine moieties of the BSA cannot be discounted.

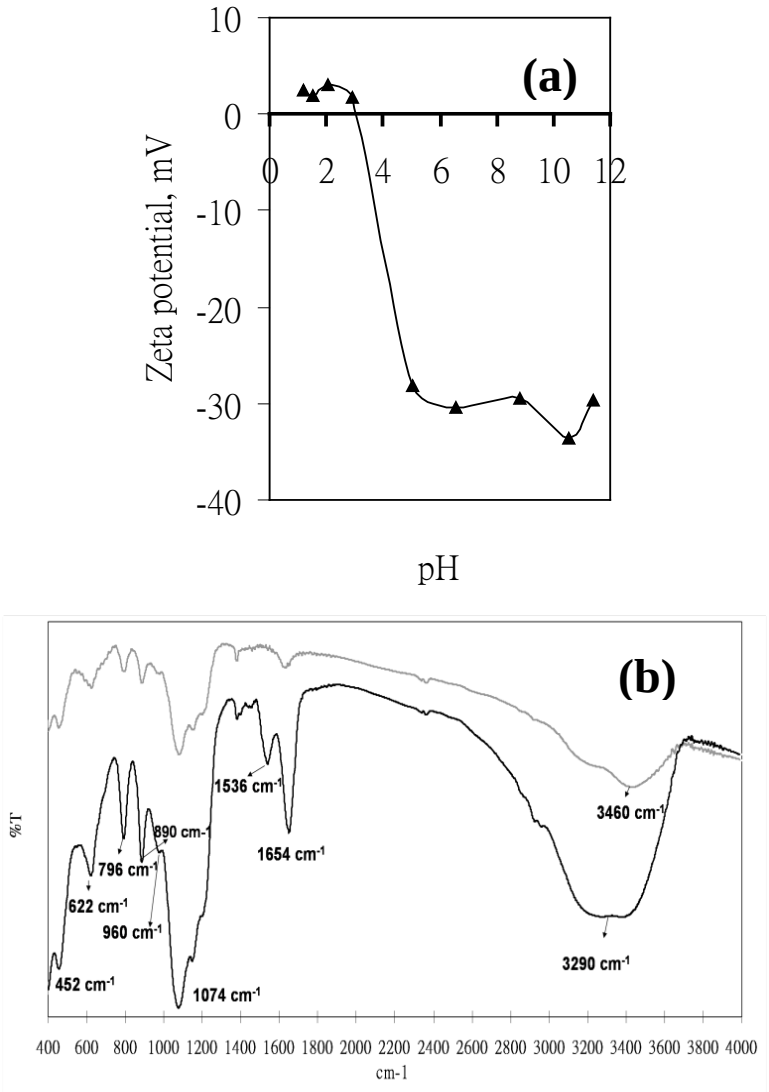

Figure 17a. ξ potential measurements of iron oxide nanoparticle encapsulated in silica coating. *Figure 17b.* IR showing the presence of surface hydroxyl groups (at 960 cm^{-1}) and 3290 cm^{-1} on silica-encapsulated iron oxide with (lower curve) and without BSA (upper curve).

In order to examine the electrostatic interaction between the immobilized BSA and the magnetic nanoparticles, a commercial SDS-PAGE electrophoresis gel analysis was used to investigate the binding pattern between BSA and the nanoparticles. According to Figure 18, the molecular weight of the native BSA of 67kD was clearly seen from the gel column together with the presence of larger aggregates of BSA. However, it observed the immobilised BSA showed the same molecular weight as the native single BSA protein. It is accepted that the mild conditions for the protein treatment and gel electrophoresis would not break extensive covalent linkages, but can separate species that are interacting electrostatically by protein denaturing. Thus, the match of molecular weight between native BSA and immobilised BSA was a result of protein separation from silica encapsulated iron oxide particles suggested primary interaction was indeed electrostatic in nature. It was noted that there was no sign of BSA aggregation from the immobilised BSA, which clearly implied the nanoparticles only captured isolated proteins on the surface through the electrostatic interactions.

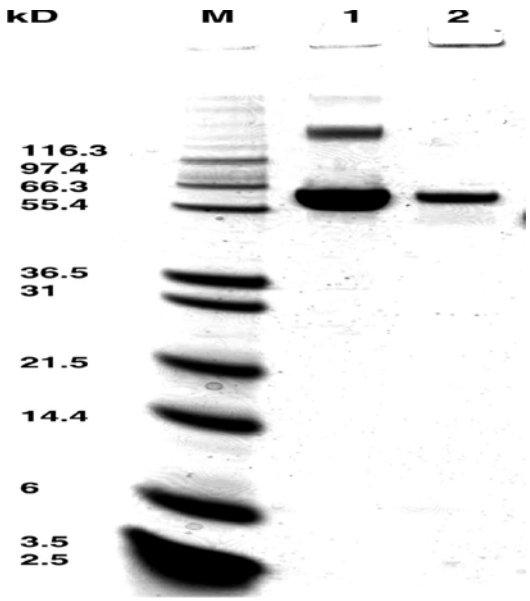

Figure 18. SDS-PAGE analysis of BSA binding to the silica-coated nanomagnet: molecular weight in kilo Daltons, kD; M (protein markers); lane 1, free BSA; lane 2, extensive washed BSA on the encapsulated magnetic nanoparticles.

In proteins, the peptide bonds –CO–NH– have several distinct vibrational modes. Amide I (C=O) and amide II (asymmetric υ of COO-) are the most useful modes for estimating the conformation (secondary structure, i.e., α-helix and β-sheet) of polypeptide backbone chain –CO–NH– in naturally occurring or artificial proteins. Thus, IR investigation of amide I and II regions of the native and immobilized BSA had taken place. For native BSA, it was noted that the peak at 1653 cm^{-1} represents intra-molecular hydrogen bonding interactions of amide I band and the peak at 1538 cm^{-1} corresponding to amide II band. We showed that both peaks in native BSA are not sensitive to a pH change from the range of pH 10 to pH 3 (Figure 19).[8,20] However, at below pH 3, a new peak at 1600 cm^{-1} at the expenses of the Amide peaks was recorded. The dramatic frequency decrease upon exposure to extreme low pH most logically can be explained by the protonation of the protein moieties groups and particularly the concomitant decrease in C=O bond strength in Amide I from 1653 to 1600 cm^{-1}.

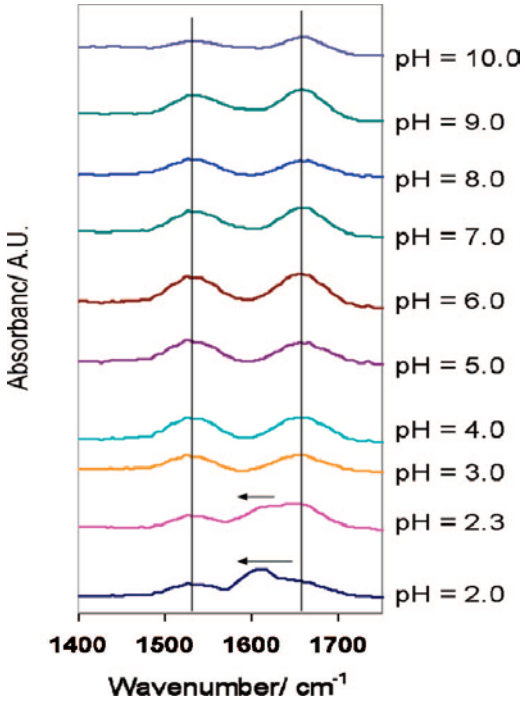

Figure 19. IR of native BSA showing virtually no change of amide I and amide II peaks from pH 10 to pH 3 (nonbuffered), but a new peak at 1600 cm^{-1} at the expense of the amide peaks is recorded at pH 2.3 and pH 2.0.

Upon the protein immobilization it was observed from Figure 20a, that both amide peaks are present but clearly attenuated in magnitude owing to some degree of unwinding α-helices to β-sheet and turn structure. It was interesting to note that a new peak at 1632 cm^{-1} clearly arises between the two amide peaks, which matched with the protonated -C=O (at or below pH 3), despite the fact that the immobilization had taken place in buffer solution of pH 7.4. Despite the external buffering ions of potassium dihydrogen phosphate it was evident that there are more competitive hydrogen bonding interactions of the C=O located on the external sheath of the protein structure with the local surface acidic hydroxyl groups on the nano magnetic body upon the direct immobilization.[20,21]

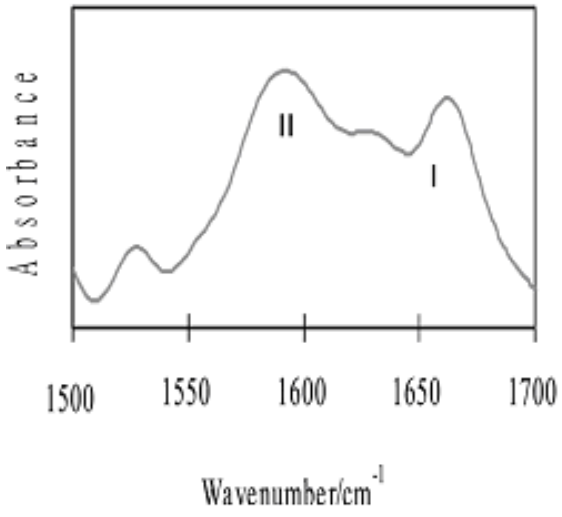

Figure 20. IR of BSA-bound silica-encapsulated iron oxide showing amide I (C=O) and amide II (-COO-) regions with a new peak at 1632 cm^{-1} between them at pH 7.40 (buffered).

The interactions of BSA with and without silica encapsulated iron oxide were examined by circular dichroism (CD) spectroscopy (Figure 21). The free native BSA clearly displayed a sharp absorption at 190 nm and two negative absorption bands: one was attributed to carbonyl excitation in polypeptide chains due to π to π^* parallel to the circular polarized at 209 nm and another one at 222 nm corresponding to n to π^* transition.[22] The characteristic positive sharp peak at 190nm and negative

double humped peaks suggest the high proportion of α-helices of the entire molecular population. It was shown that the characteristic CD patterns of α-helix progressively fade at lower non-buffered pHs indicative of its conversion to other conformations (Figure 22). Again, comparing to the native BSA the CD spectrum of BSA bound silica encapsulated iron oxide nanoparticle at buffered pH 7.4 indicates a similar degree of attenuation in the α-helical peaks as those of at the extreme low pH (pH 3) confirming the partial deformation of α-helical structure upon immobilization. This reinforces the fact that the functional groups (C=O and -NH) of α-helices are stretched by the local acidic surface hydroxyl group on magnetic body owing to the partial impairment or breakage of intra-molecular hydrogen bonds within and between the helical structures.

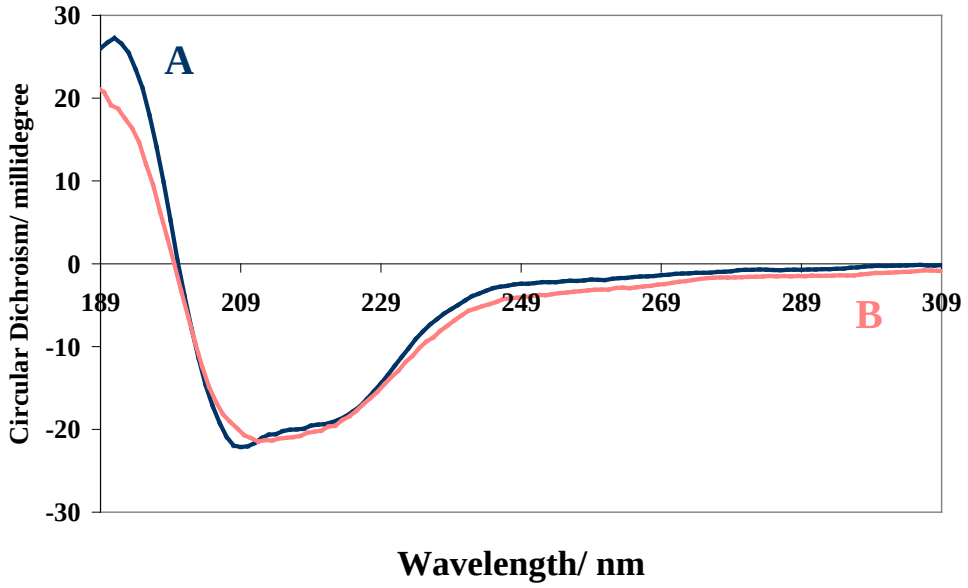

Figure 21. Circular dichroism spectra of A) native BSA and B) BSA-bound silica-encapsulated iron oxide at pH 7.40 (buffered) showing the attenuation in the proportion of R-helices of BSA upon immobilization.

Thus, there was a clear alteration in α-helical structure on the external sheath of the protein in a direct contact with local surface groups on the magnetic particles from

both the IR and CD analysis. One key question was that how far the protein denatured upon immobilization as some strong linkages between polypeptide chains such as disulphide interaction, may be robust enough to retain a degree of protein integrity during the attachment of the BSA.[20-22] In essence, whether the protein still remained functional and active upon immobilization on the nano magnet surface is yet to be answered.

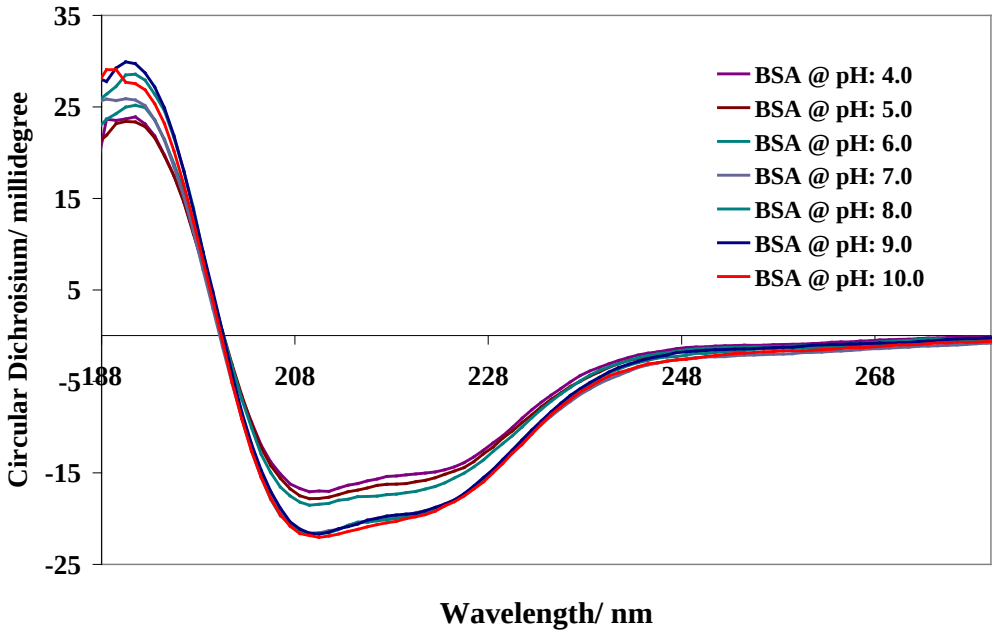

Figure 22. Circular dichroism spectra showing the progressive fading of the characteristic peaks (sharp positive peak at around 190 nm and two negative double humped peaks at 209 and 222 nm) of R-helices in native BSA at lower non-buffered pH's.

The conformation of immobilized protein the binding constants of typical site I and site II drug compounds with anchored BSA were investigated. According to Curry *et. al.*, the binding site of warfarin (site I drug), shown in figure 23, is located in sub-domain II and ibuprofen (site II drugs), shown in figure 24, in site II of sub-domain IIIA.[23] Using site I and site II drug molecules, namely warfarin and ibuprofen, we may differentiate the functionality of these two sites through the study of their binding constants. Since the drug binding property of BSA clearly reflects its biological

activity, which is governed by its tertiary structure. The reaction between the drug and the protein can be expressed mathematically as follows:

$$\mathbf{BSA} + \mathbf{Drug} \underset{\leftarrow}{\overset{\rightarrow}{}} \mathbf{BSA \setminus Drug} \qquad \mathbf{(5)}$$

$$K_a$$

The protein-drug binding affinity is expressed in term of the Log Ka value. The Ka is the equilibrium value of association which is expressed mathematically below:

$$K_a = \frac{\mathbf{[BSA \setminus Drug]}}{\mathbf{[BSA_f]} \times \mathbf{[Drug_f]}} \qquad \mathbf{(6)}$$

Where:

$[BSA_f]$ is free BSA in mol dm^{-3}

$[Drug_f]$ is free Drug in mol dm^{-3}

[BSA\Drug] is the BSA drug complexe in mol dm^{-3}

The drug binding constant between each drug and free BSA was then calculated according to previous UV-visible or other spectroscopic studies provided that the BSA-drug conjugate can be separated from free drug and BSA using dialysis.[24] It should be noted that in our case the slow and inefficient separation step using dialysis membrane can be replaced by magnetic precipitation (placing an external magnet of with BHmax = 38 MGOe under the container) which allowed the supernatant containing free forms of drug molecules to be measured independently from the precipitate of BSA-drug on magnetic bodies on the bottom of the container.

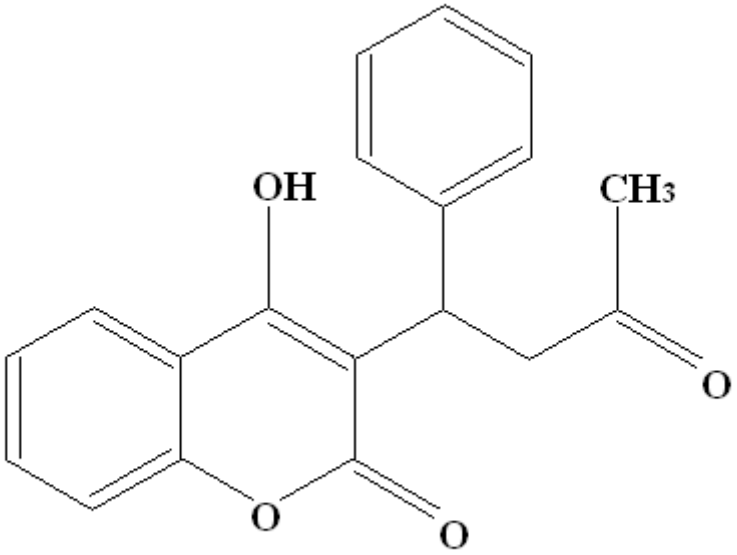

Figure 23. The molecular structure warfarin molecule.

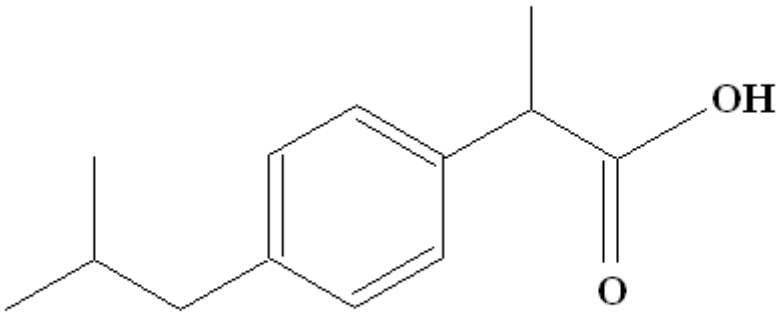

Figure 24. The molecular structure of ibuprofen molecule.

The measured values are shown in Table 1. As seen from the table, the measured binding constants immobilized BSA are close to those values of native BSA implying that the sites are remained active and functional as high binding sites (large Log Ka values).[24-26] An excellent match in the case of site II drug (ibuprofen). However,

there was a small reduction in the binding constant value when using site I drug (warfarin), which indicated that the conformation modification of the immobilized BSA, even these sites, were deeply buried in the tertiary structure. It was noted that Larsericsdotter and his co-workers used NMR to elucidate the structural modifications on the binding sites of the BSA. They found that the domain II (site I) of BSA significantly lost its binding functionality upon immobilisation on extended silica surface. It was postulated that this site was blocked as it directly faces towards the silica surface in the adsorption geometry.[15]

Our small deviation from the literature value of the warfarin molecules with free BSA with the immobilised BSA on $SiO_2@Fe_3O_4$, suggests that such silica surface blockage of this site on BSA indeed takes place, but must be dependent on the size of silica particles. In our case, the use of magnetic core-shell silica nanoparticles instead of the extensive silica surface alleviates the errors in measurement. Also, this small deviation in log Ka value was much smaller than those effects using different buffer concentrations and temperatures.[25] Scheme 1 illustrates the differential binding modes of drug molecules at different locations of BSA. With respect to the use of the immobilized BSA on nano magnetic carrier for screening of drug candidates, it would therefore be desirable to reduce or totally eliminate the blockage of the binding sites by using appropriate smaller size carriers (with calibration curve). Further work is being carried out in our laboratory and results will be reported in due course.

Drug	log *Ka*	literature value
warfarin (site I)	4.26 ± 0.05	4.46[27]
ibuprofen (site II)	4.43 ± 0.05	4.51[28]

TABLE 1: Comparison Protein Binding Constants of Immobilized BSA on Silica-Coated Nano Magnet with Data of Native BSA from the Literature. Log Ka is derived from UV-visible determination of the warfarin or ibuprofen concentration in a buffered solution of pH 7.41 before and after drug binding with a silica-coated nano-magnet with magnetic separation (see Figure 3).

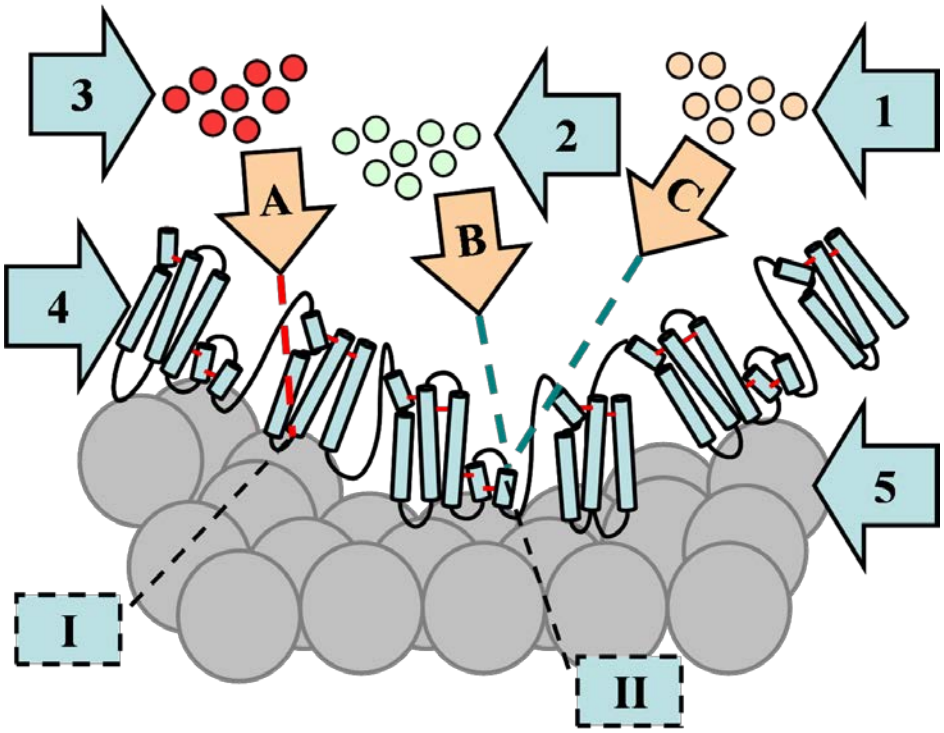

SCHEME 1: A Schematic Presentation of the Respective Locations of BSA with the I) Site I of Silica and Warfarin and the Site II of Ibuprofen and Diazepam, where 1) ibuprofen, 2) diazepam, 3) warfarin, 4) BSA, 5) silica porous material, I) site I and II) site II.

2.5 Drug binding calculations

The drug binding constants for each drug, diazepam, ibuprofen and warfarin were calculated from the drug binding constant expressed in the following equations:

$$\mathbf{BSA} + \mathbf{Drug} \underset{K_a}{\overset{\rightarrow}{\leftarrow}} \mathbf{BSA \setminus Drug} \qquad \mathbf{(7)}$$

$$K_a = \frac{[\mathbf{BSA \setminus Drug}]}{[\mathbf{BSA_f}] \times [\mathbf{Drug_f}]} \qquad \mathbf{(8)}$$

The calibration curve was constructed to measure the concentration of the initial and the excess drugs and protein. For each drug the calibration curves had shown a straight line with strong regression coefficient values between absorbance and concentration at characteristic wavelength, which agrees with the Beer-Lambert law.

$$[BSA_t] = [BSA_f] + [BSA \setminus Drug] \quad (9)$$

$$[Drug_t] = [Drug_f] + [Drug \setminus BSA] \quad (10)$$

Both [BSA\Drug] and [Drug\BSA] are the same complexes and so:

$$[BSA_f] = [BSA_t] - [BSA \setminus Drug] \quad (11)$$

$$[Drug_t] - [Drug_f] = [Drug \setminus BSA] \quad (12)$$

Substituting (10) in (9) the expression above becomes:

$$[BSA_f] = [BSA_t] - ([Drug_t] - [Drug_f]) \quad (13)$$

$$[BSA_f] = [BSA_t] - [Drug_t] + [Drug_f] \quad (14)$$

Substituting the expression above in (8) the expression becomes:

$$K_a = \frac{([Drug_t] - [Drug_f])}{[Drug_f]([BSA_t] - [Drug_t] + [Drug_f])} \quad (15)$$

Where:

K_a	is the affinity constant in dm^3mol^{-1}
$[BSA_t]$	is total BSA in mol dm^{-3}
$[BSA_f]$	is free BSA in mol dm^{-3}
$[Drug_t]$	is total drug mol dm^{-3}
$[Drug_f]$	is free Drug in mol dm^{-3}
[BSA\Drug]	is the BSA drug complexe in mol dm^{-3}

According to the Beer-Lambert law:

$$\mathbf{A} = \varepsilon \times l \times \mathbf{C} \quad \textbf{(16)}$$

$$\mathbf{C} = \frac{\mathbf{A}}{\varepsilon \times l} \quad \textbf{(17)}$$

Where:

A is absorbance in arbitrary unit

ε is molar absorpitivity in $dm^3mol^{-1}cm^{-1}$

l is pathway length in cm

C is the concentration in $moldm^{-3}$

$\mathbf{A_b}$ is absorbance before the experiment in arbitrary unit

$\mathbf{A_a}$ is absorbance after the experiment in arbitrary unit

$$\mathbf{[Drug_t]} = \frac{\mathbf{A_b}}{\varepsilon \times l} \quad \textbf{(18)}$$

$$\mathbf{[Drug_f]} = \frac{\mathbf{A_a}}{\varepsilon \times l} \quad \textbf{(19)}$$

$$\mathbf{[Drug_t]} = \frac{\mathbf{A_a}}{\varepsilon \times l} \quad \textbf{(20)}$$

$$\mathbf{[Drug_t] - [Drug_f] = [BSA \setminus Drug]} \quad \textbf{(21)}$$

$$\mathbf{[BSA \setminus Drug]} = \frac{\mathbf{A_b}}{\varepsilon \times l} - \frac{\mathbf{A_a}}{\varepsilon \times l} \quad \textbf{(22)}$$

$$\mathbf{[BSA \setminus Drug]} = \frac{\mathbf{A_b - A_a}}{\varepsilon \times l} \quad \textbf{(23)}$$

According to equation (11)

$$\mathbf{[BSA_f] = [BSA_t] - [BSA \setminus Drug]}$$

$$\mathbf{[BSA_f] = [BSA_t] - (\frac{A_b - A_a}{\varepsilon \times l})} \quad \textbf{(24)}$$

Substituting equation equations (18), (19), and (24) in (15) the expression becomes

$$K_a = \frac{\left(\frac{A_b - A_a}{\varepsilon \times l}\right)}{\left(\frac{A_a}{\varepsilon \times l}\right) \times ([BSA_t] - \left(\frac{A_b - A_a}{\varepsilon \times l}\right)} \quad (25)$$

The mathematical expression above simplifies to:

$$K_a = \frac{(A_b - A_a)}{(A_a) \times ([BSA_t] - \left(\frac{A_b - A_a}{\varepsilon \times l}\right)} \quad (26)$$

$$\text{Drug binding constant} = -\log K_a \quad (27)$$

$$\text{Drug binding constant} = -\log\left(\frac{(A_b - A_a)}{(A_a) \times ([BSA_t] - \left(\frac{A_b - A_a}{\varepsilon \times l}\right)}\right) \quad (28)$$

2.6 Conclusion

It is demonstrated that encapsulation of magnetic iron oxide nanoparticles in a thin amorphous silica as a core shell nanostructure, can uptake a high loading of BSA protein. The nano carrier covering with silanol groups assists the immobilization of BSA as active surface species through primarily electrostatic interaction. However, a partial unfolding of secondary structure on the external sheath of the protein is taking place due to competitive hydrogen bonding interactions of functional groups of the BSA (C=O, -NH) with the local acidic surface hydroxyl groups on the nano magnetic body despite the use of buffered pH 7.4 solution. However, the internal hydrophobic sites I and II of the protein still remain intact to a high degree for specific drug molecule bindings.

2.7 References

(1) H. Larsericsdotter, S. Oscarsson, J. Buijs, *J. Colloid Interface Sci*. **2005**, *289*, 26-35.

(2) F. C. Meldrum, B. R. Heywood, S. Mann, *Science*. **1992**, *257*, 522-523.

(3) B. Orioni, M. Roversi, C. La Mesa, F. Asaro, G. Pellizer, G. D'Errico, *J. Phys. Chem. B*. **2006**, *110*, 12129-12140.

(4) L. Yang, R. M. Xing, Q. M. Shen, K. Jiang, F. Ye, J. Y. Wang, Q. S. Ren, *J. Phys. Chem. B*. **2006**, *110*, 10534-10539.

(5) J. M. Perez, F. J. Simeone, Y. Saeki, L. Josephson, R. Weissleder, *J. Am. Chem. Soc*. **2003**, *125*, 10192-10193.

(6) S. C. Tsang, V. Caps, I. Paraskevas, D. Chadwick, D. Thompsett, *Angew. Chem. Int. Ed. Engl*. **2004**, *43*, 5645-5649.

(7) J. Buijs, C. C. Vera, E. Ayala, E. Steensma, P. Håkansson, S. Oscarsson, *Anal. Chem*. **1999**, *71*, 3219-3225.

(8) A. Kondo, S. Oku, F. Murakami, K. Higashitani, *Colloids Surf. B. Biointerfaces*. **1993**, *1*, 197-201.

(9) H. Larsericsdotter, S. Oscarsson, J. Buijs, *J. Colloid Interface Sci*. **2001**, *237*, 98-103.

(10) S. C. Tsang, C. H. Yu, X. Gao, K. Tam, *J. Phys. Chem. B*. **2006**, *110*, 16914-16922.

(11) C. K. Kim, Y. S. Chun, W. L. Lah, *Arch. Pharmacal Res*. **1989**, *12*, 160-165.

(12) Kragh-Hansen, *U. Pharmacol. Rev*. **1981**, *33*, 17-53.

(13) C. E. Petersen, C. E. Ha, S. Curry, N. V. Bhagavan, *Proteins*. **2002**, *47*, 116-125.

(14) V. S. Jisha, K. T. Arun, M. Hariharan, D. Ramaiah, *J. Am. Chem. Soc*. **2006**, *128*, 6024-6025.

(15) V. Lhiaubet-Vallet, Z. Sarabia, F. Bosca, M. A. Miranda, *J. Am. Chem. Soc*. **2004**, *126*, 9538-9539.

(16) S. Curry, H. Mandelkow, P. Brick, N. Franks, *Nat. Struct. Biol*. **1998**, *5*, 827-835.

(17) X. M. He, D. C. Carter, *Nature*. **1992**, *358*, 209-215.

(18) X. Q. Liu, J. M. Xing, Y. P. Guan, G. B. Shan, H. Z. Liu, *Colloid Surf. A-Physicochem. Eng. Asp*. **2004**, *238*, 127-131.

(19) C. H. Yu, N. Caiulo, C. C. H. Lo, K. Tam, S. C. Tsang, *Adv. Mater*. **2006**, *18*, 2312-2314.

(20) V. Militello, C. Casarino, A. Emanuele, A. Giostra, F. Pullara, M. Leone, *Biophys. Chem*. **2004**, *107*, 175-187.

(21) K. Murayama, M. Tomida, *Biochemistry*. **2004**, *43*, 11526-11532.

(22) L.Yang, R. Xing, Q. Shen, K. Jiang, F. Ye, J. Wang, Q. Ren, *J. Phys. Chem. B*. **2006**, *110*, 10534-10539.

(23) C. E. Petersen, C. E. Ha, S. Curry, N. V. Bhagavan, *Proteins: Struct., Funct., Bioinf*. **2002**, *47*, 116-125.

(24) M. Takaka, Y. Asahi, S. Masuda, T. Ota, *Chem. Pharm. Bull*. **1991**, *39*, 1-4.

(25) C. Dufour, O. Dangles, *Biochim. Biophys. Acta, Gen. Subj*. **2005**, *1721*, 164-173.

(26) P. Sun, A. Hoops, R. A. Hartwick, *J. Chromatogr., B: Biomed. Appl*. **1994**, *661*, 335-340.

(27) C. Dufour, O. Dangles, *Biochim. Biophys. Acta*. **2005**, *1721*, 164-.

(28) Sun, P.; Hoops, A.; Hartwick, R. A. *J. Chromatogr. B*. **1994**, *661*, 335-.

Chapter Three

Electrostatic Entrapment of Protein Molecules on Fe_3O_4 Nanoparticles

Contents

3.1 Overview

Recently, there is an interest to use inorganic-based magnetic nanoparticles as a vehicle to carry biomolecules for various biophysical applications. However, the direct attachment of the molecules is known to alter their conformation, leading to attenuation in activity. Furthermore, surface immobilization has been limited to monolayer coverage. Here, it is shown that alternate depositions of negatively charged protein molecules, typically bovine serum albumin (BSA) with a positively charged aminocarbohydrate template such as glycol chitosan (GC) on magnetic iron oxide nanoparticle surface as a colloid, could be accomplished at pH 7.4. Circular dichroism (CD) clearly reveals that the secondary structure of the entrapped BSA sequential depositions in this manner remain unaltered, which is in contrast to previous literature. Probing the binding properties of the entrapped BSA using small molecules (Site I and Site II drug compounds) confirms *for the first time* the full retention of its biological activity as compared with native BSA, implying the ready accessibility of the entrapped protein molecules through the porous overlayers. This work suggests a new method to immobilize and store protein molecules beyond monolayer adsorption on a magnetic nanoparticle surface without structural alteration. This may open applications in magnetic recoverable enzymes or protein delivery.

3.2 Introduction

Encapsulation of biomolecules within inorganic host materials has been extensively investigated due to many potential biotechnological applications.[1] Recent reports on surface-functionalized superparamagnetic iron oxides as a nanosize vehicle to carry biomolecules have demonstrated their feasibility for use in a variety of biological applications, for example in magnetic resonance imaging,[2] bioseparation,[3-5] tissue repairing, drug/gene delivery [6-8] and thermal tumor therapy [9]. In these applications, the biomolecules are first immobilized onto magnetic particle surfaces with high loading to allow the magnetic guidance followed by usage of a small amount of biologically active sample. Although a large numbers of groups reported the synthesis and potential applications of biomolecules tagged on the magnetic vehicles, few have focused on the immobilization of biomolecules on their surfaces. In the past decade, a variety of experimental methods have been developed to immobilize biomolecules (proteins) on bulk solid surfaces, which include noncovalent,[10] covalent,[11,12] and bioaffinity[13,14] immobilizations. However the unfolding and/or denaturation of proteins under perturbation by an extensive surface are some of the key issues. There are advantages as well as drawbacks for the above immobilization methods, depending on the affinity of the protein for a particular surface, preparation complexity, as well as the extent of structural alteration. For example, most proteins adsorb with higher affinity to hydrophobic surfaces may result in a higher degree of structural alternation [15,16] whereas excessive affinity with hard acidic/basic sites on inorganic surfaces may also be accompanied by a reduction in native structures.[17] It is noted that most of the above immobilization techniques can only allow the deposition of protein molecules of below monolayer coverage. For the applications using magnetic nanovehicles to deliver biomolecules or to support functional proteins for catalysis (enzymes), the most important challenge is to retain the conformation and activity of the molecules on a particle surface, which has not yet been ascertained in many previous studies. Ulman *et. al.* reported a successful method for immobilizing proteins on pure γ-Fe_2O_3 magnetic nanoparticles for biological use.[18] However, the proteins were immobilized directly on these surfaces, their stability and activity were affected by the chemical environment in a close proximity. Attachment of proteins on silica-based nanoparticles or silica-coated magnetic nanoparticles has been developed as an alternative approach,[19-21] However, recent work suggested they could introduce

undesirable alteration in protein conformation and blockage of active biological sites upon immobilization on the silica surface.[3,17] On the other hand, extensive films could be fabricated on the substrate surface by alternating adsorption of oppositely charged polyions. Owing to its simplicity and versatility, many polyions have been used to fabricate films including synthesized and natural polyelectrolytes.[22,23] In this work, we report the immobilization on magnetic iron oxide nanoparticles, which was achieved *via* a simple electrostatic deposition of amino-carbohydrate template followed by BSA (figure 1-3) in alternate layers. Chitosan, a linear polysaccharide composed of ß-(1-4)- linked glucosamine (figure 4), may be applied as a template, but suffers from limited solubility in water. As a result, glycol chitosan (GC) was chosen for co-immobilisation with BSA on the magnetic nanoparticle surface. The structure and morphology of these magnetic assembly nanoparticles are characterized and reported herein.

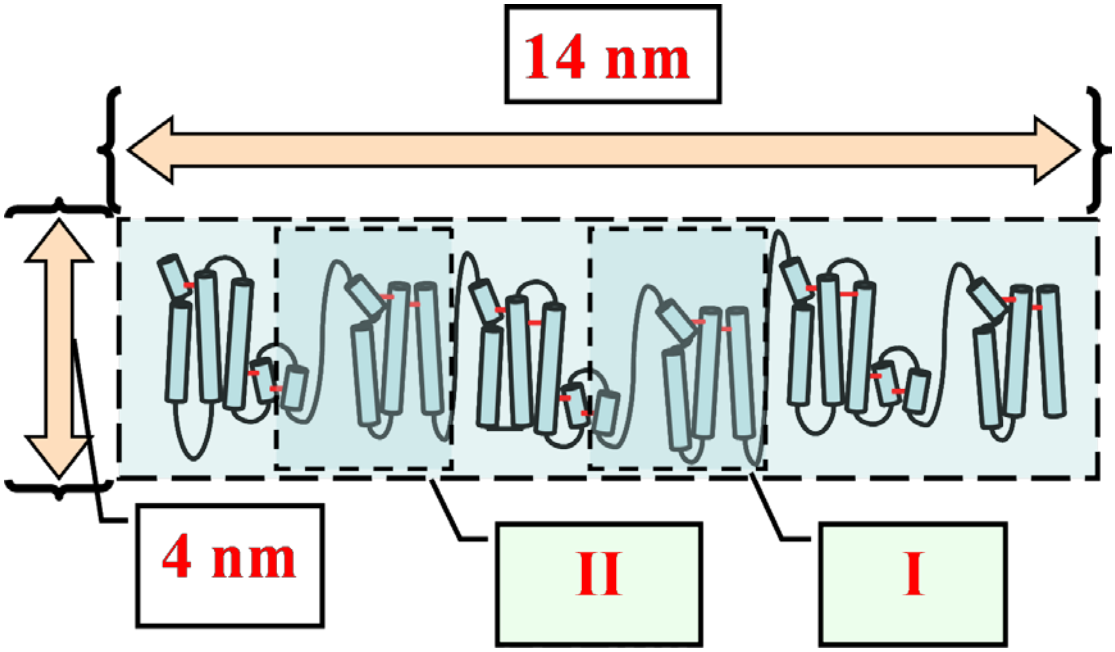

Figure 1. Dimension of BSA (14 nm × 4 nm) and the location of binding sites, (I) site I and (II) site II.

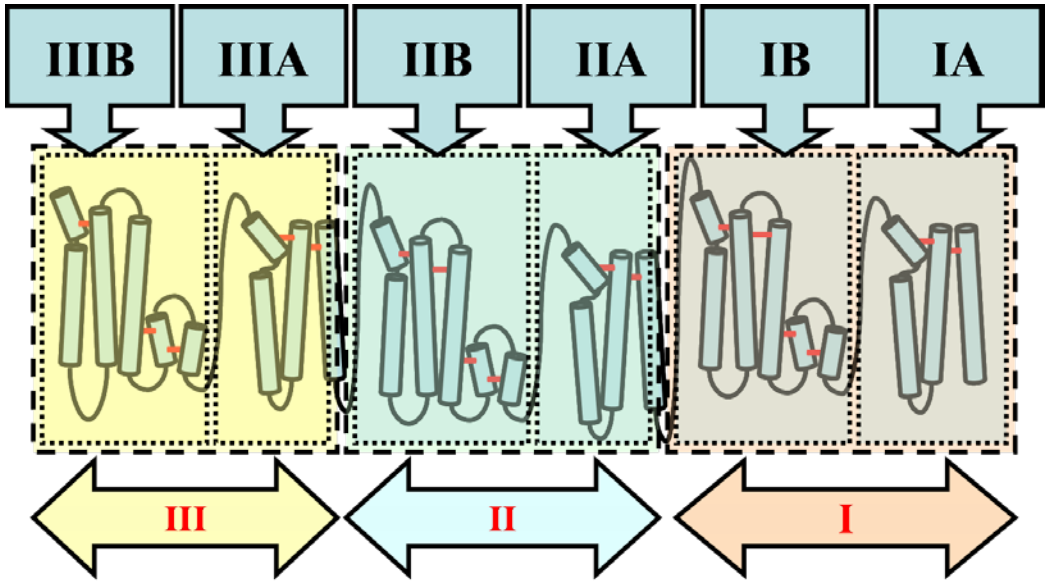

Figure 2. BSA with repeated identical domains I) domain I, II) domain II and III) domain III. Each domain can be further divided to IA) and IB) subdomain A and B in domain I, IIA) and IIB) subdomain A and B in domain II, and IIIA) and IIIB) subdomain A and B in domain III respectively.

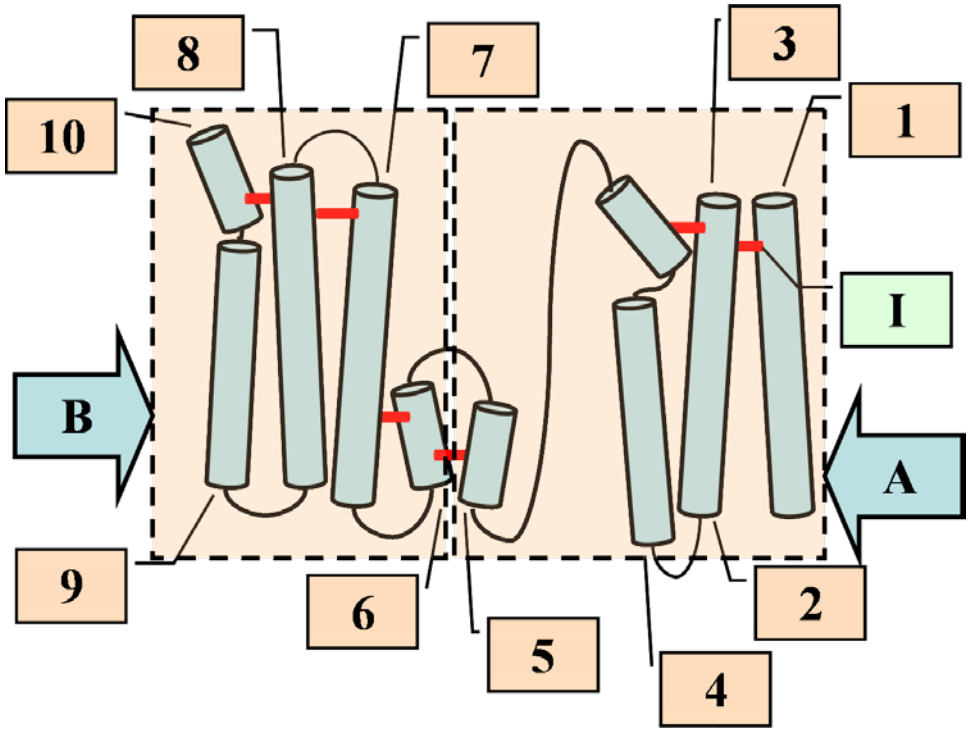

Figure 3. Schematic structure of one of the repeated domains of BSA which consist of 1-10) principle helices 1-10, adjacent helices are bonded by I) S-S bond, and the domain is divided to A) sub-domain A and B) sub-domain B.

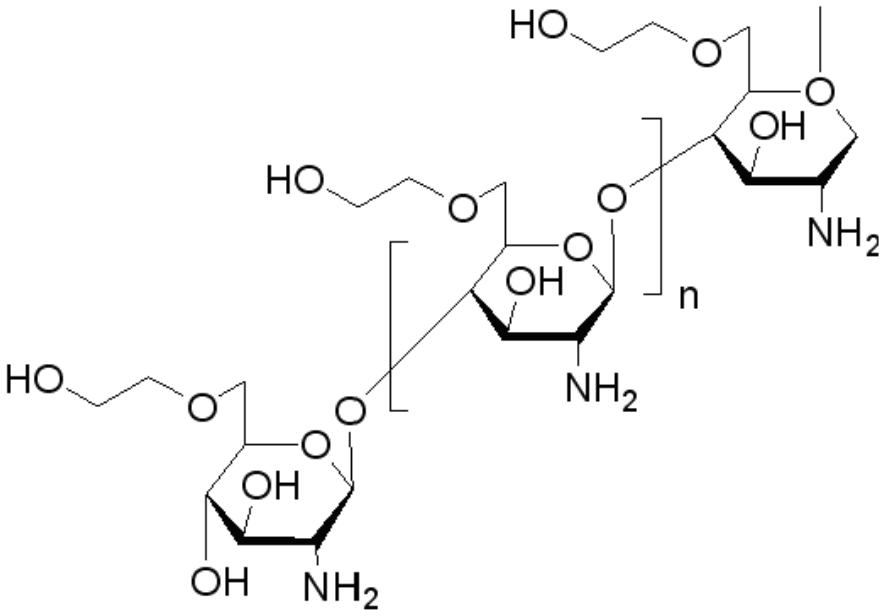

Where n ≥400

Figure 4. Repeated unit structure of glycol chitosan.

3.3 Experimental Section

3.3.1 Sources of Chemicals

All chemicals were purchased from Aldrich Sigma. BSA was graded ~99% which was γ-globulin free. Iron (II) chloride tetrahydrate and iron (III) chloride hexahydrate were used. Ammonia (35%) and concentrated hydrochloric acid solutions were purchased from Fisher. Bovine serum albumin (BSA) is a well-characterized protein with molar mass of 67 000 Da of isoelectric point of 4.9. Glycol chitin, deacetylated (GC) with a degree of polymerization > 400 (average molar mass of 500 000 Da), was obtained from Aldrich Sigma.

3.3.2 Sample Preparation

The iron oxide nanoparticle as a colloid was prepared via coprecipitation of iron (II) and iron (III) chlorides in aqueous solution with the addition of ammonia

$$Fe^{2+}_{(aq)} + 2Fe^{3+}_{(aq)} + 8OH^{-}_{(aq)} \rightarrow Fe_3O_{4(s)} + 4H_2O_{(l)} \quad (1)$$

The typical procedure for the preparation of iron oxide stock solution was as follows: 1.7 g of iron (II) salt and 2.7 g of iron (III) salt were dissolved in 200 mL of water at 50 °C and stirred for 1 h under a nitrogen atmosphere before the addition of 4 mL of 35% ammonia solution. The ammonium hydroxide solution was added in very small proportion (0.1 mL) over a long period of time (approximately 0.05 mL/s) while the mixed solution was stirring vigorously. The solution of iron (II) and iron (III) was originally yellowish in color, but upon the addition of ammonia, the solution turned dark brown indicative of the formation of iron oxide nanoparticles.

The entrapment of BSA by immobilized GC on the iron oxide nanoparticle was carried out as follows: 5 mL of 0.1 mg/mL of iron oxide solution (diluted from the stock), 5 mL of 1.0 mg/ mL of GC solution, and 5 mL of 1.0 mg/mL BSA solution were prepared separately. All the solutions were prepared using double distilled water presonicated for 10 min at 25 °C. Solutions of 0.1 M HCl and 0.1 M NaOH were prepared for the adjustment of pH values accordingly. Thus, 5 mL of iron oxide colloid solution was slowly added to the 5mL GC solution with constant stirring in a dropwise manner. It is very important to add the iron oxide particle to the GC and not vice versa, to ensure the layer-by-layer growth. The final mixed solution was sonicated at 25 °C for 10 min. An external magnet was placed underneath the container to induce magnetic precipitation of the iron oxide/GC particles. After separation, the excess of supernatant GC solution was decanted. The collected iron oxide/GC particle was washed with pH 7.4 solution three times. The solution was then sonicated at 25 °C for 10 min to ensure all the colloid particles entered the solution phase. Repeated application of external magnetic field to sediment the coated particles, washing, and decanting of the particles were carried out. Similarly, the same

procedure was applied for the subsequent deposition of the iron oxide/GC particle with 5 mL of prepared BSA solution.

2.3.2 Experimental procedure for constructing GC calibration curves

0.0500 grams of GC was weighed in 50 ml volumetric flask. Approximately 10 ml of phosphate buffer at pH 7.4 was added to dissolve the GC powder into clear solution. A further phosphate buffer was added to the 50 ml mark to make up 1 mg/ml GC stock solution. 2.5 ml aliquot of GC stock solution was transferred to 10 ml disposable glass Vials, each diluted at different volumes. The absorbance of each diluted solution was taken against a reference cell containing phosphate buffer at pH 7.4. Thus, the GC absorption peaks at different concentrations are shown in figure 5 with the straight line plot of concentration against absorbance in the inset graph.

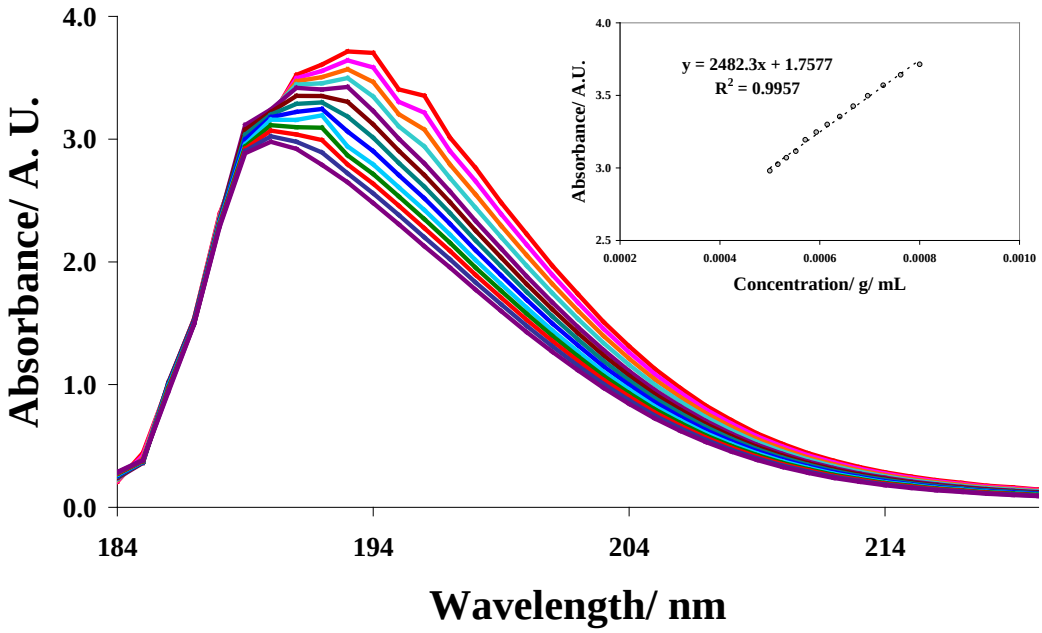

Figure 5. Absorption peak for GC at 190 nm wavelength at different concentrations, the plot of concentration against absorption gives a straight line in the inset graph.

2.3.3 Experimental procedure for constructing BSA calibration curves

0.0500 grams of BSA was weighed in 50 ml volumetric flask. Approximately 10 ml of phosphate buffer at pH 7.4 was added to dissolve the BSA powder into clear solution. A further phosphate buffer was added to the 50 ml mark to make up 1 mg/ml BSA stock solution. 2.5 ml aliquot of BSA stock solution was transferred to 10 ml disposable glass Vials, each diluted at different volumes. The absorbance of each diluted solution was taken against a reference cell containing phosphate buffer at pH 7.4. Thus, the BSA absorption peaks at different concentrations are shown in figure 6 with the straight line plot of concentration against absorbance in the inset graph.

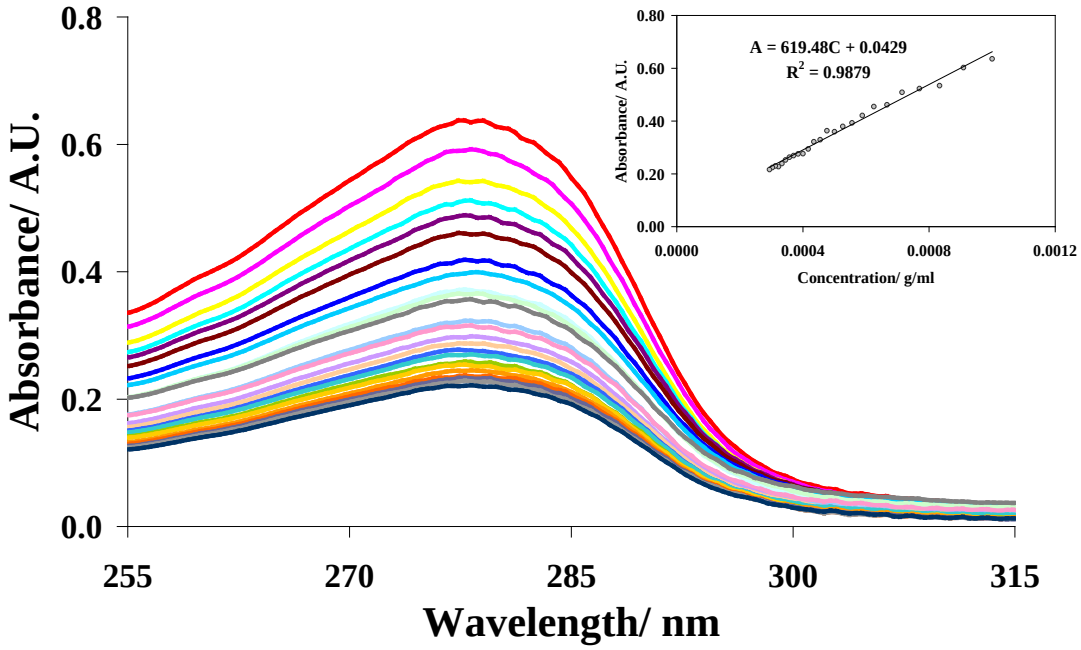

Figure 6. Absorption peak for BSA at 278 nm wavelength at different concentrations, the plot of concentration against absorption gives a straight line in the inset graph.

2.3.4 Experimental procedure for constructing ibuprofen calibration curves

0.0500 grams of ibuprofen was weighed in 50 ml volumetric flask. Approximately 10 ml of phosphate buffer at pH 7.4 was added to dissolve the ibuprofen powder into clear solution. A further phosphate buffer was added to the 50 ml mark to make up 1 mg/ml ibuprofen stock solution. 2.5 ml aliquot of ibuprofen stock solution was

transferred to 10 ml disposable glass Vials, each diluted at different volumes. The absorbance of each diluted solution was taken against a reference cell containing phosphate buffer at pH 7.4 using Perkin Elmer Lambda 19. Thus, the ibuprofen absorption peaks at different concentrations are shown in figure 7 with the straight line plot of concentration against absorbance in the inset graph.

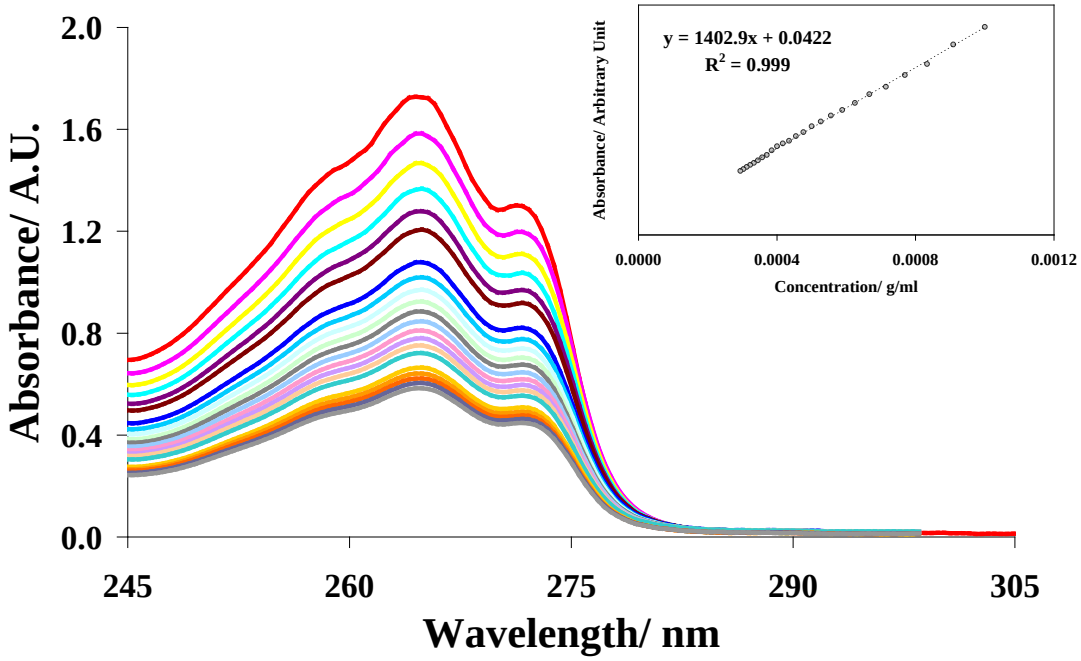

Figure 7. Absorption peak for ibuprofen at 273 nm wavelength at different concentrations, the plot of concentration against absorption gives a straight line in the inset graph.

2.3.5 Experimental procedure for constructing diazepam calibration curves

0.0500 grams of diazepam was weighed in 100 ml volumetric flask. Approximately 10 ml of phosphate buffer at pH 7.4 was added to dissolve the diazepam powder into clear solution. A further phosphate buffer was added to the 100 ml mark to make up 0.05 mg/ml diazepam stock solution. 2.5 ml aliquot of diazepam stock solution was transferred to 10 ml disposable glass Vials, each diluted at different volumes. The absorbance of each diluted solution was taken against a reference cell containing phosphate buffer at pH 7.4. Thus, the diazepam absorption peaks at different

concentrations are shown in figure 8 with the straight line plot of concentration against absorbance in the inset graph.

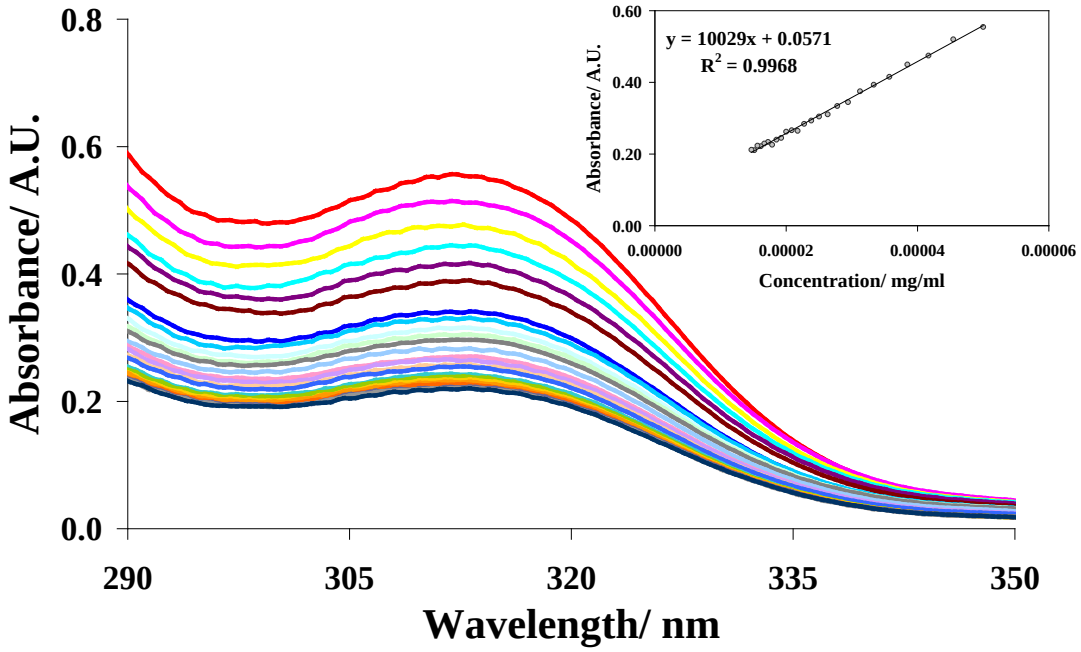

Figure 8. Absorption peak for diazepam at 311 nm wavelength at different concentrations, the plot of concentration against absorption gives a straight line in the inset graph.

2.3.6 Experimental procedure for constructing warfarin calibration curves

0.0017 grams of warfarin was weighed in 100 ml volumetric flask. Approximately 10 ml of phosphate buffer at pH 7.4 was added to dissolve the warfarin powder into clear solution. A further phosphate buffer was added to the 100 ml mark to make up 0.017 mg/ml warfarin stock solution. 2.5 ml aliquot of warfarin stock solution was transferred to 10 ml disposable glass Vials, each diluted at different volumes. The absorbance of each diluted solution was taken against a reference cell containing phosphate buffer at pH 7.4. Thus, the warfarin absorption peaks at different concentrations are shown in figure 9 with the straight line plot of concentration against absorbance in the inset graph

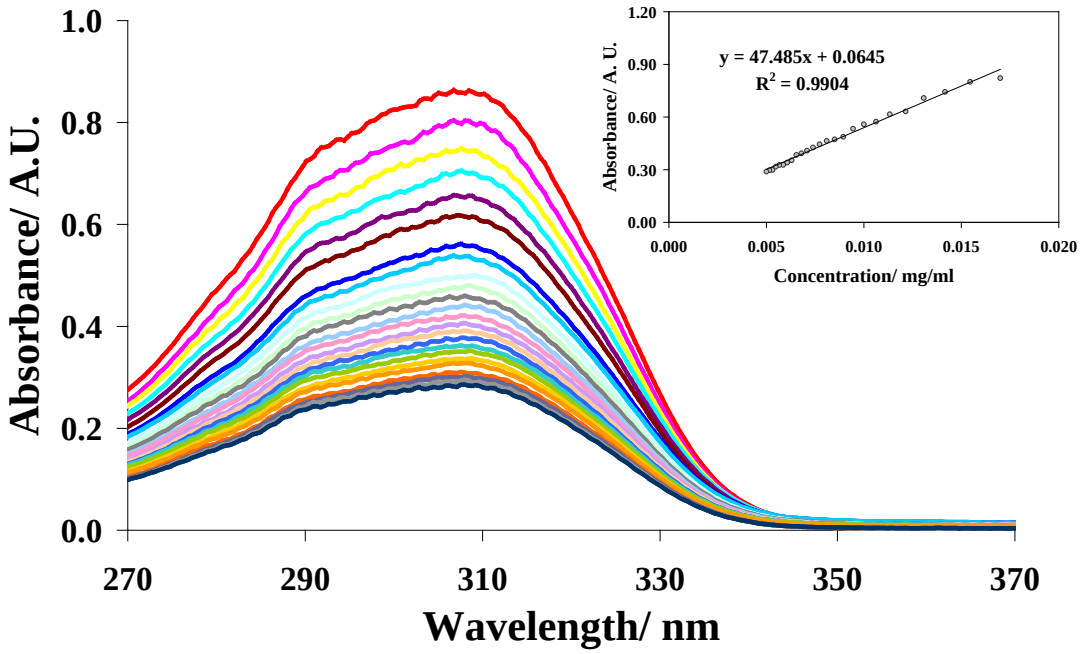

Figure 9. Absorption peak for warfarin at 306 nm wavelength at different concentrations, the plot of concentration against absorption gives a straight line in the inset graph.

3.3.3. Material Characterization

X-ray diffraction data were collected using a Philips PW1729 diffractometer, operating in Bragg-Brentano focusing geometry and using Cu Kα radiation (λ = 1.5418 Å) from a generator operating at 40 kV and 30 mA. Samples were prepared by placing a drop of nanoparticle suspension on a glass slide and allowing the solvent to evaporate naturally at room temperature. This process was repeated many times until a smooth layer of material was deposited on the slide surface. The Scherrer equation was used to estimate average iron oxide particle size from the mean value derived from the (311) peak taking the instrumental line broadening into account. TEM images were obtained using a JEOL 3000FX microscope with a high-resolution pole piece. The samples were prepared by placing a drop of nanoparticle suspension onto a carbon-coated copper grid and allowing the solvent to evaporate naturally at room temperature. Vibrating sample magnetometry (VSM) measurements were conducted using a VSM instrument (model 4500, Princeton Applied Research equipped with a

7000 Oe electromagnet). For all samples, measurements were made using a maximum field of 7000 Oe to determine magnetic moments of the samples. For selected samples which appear to be superparamagnetic with no coercivity, another round of measurements with higher-field resolution were made using a smaller maximum applied field (100 or 200 Oe) for more accurate measurements of their coercivities. The measurement times varied a lot due to different signal-to-noise ratios for different samples (longer measurement times for weaker signals). Zeta potential measurements of the unmodified magnetic nanoparticles and GC and BSA coated magnetic materials were carried out to determine the surface properties of particles. Samples were prepared in various pH value solutions at around pH = 2-11. The zeta potentials were performed using a Malvern Zetasizer Nano.

The FTIR measurements were carried out using a Nicolet 6700 ATR-IR spectrometer with a liquid-nitrogen-cooled MCT detector. A small drop of the iron oxide sample was placed on a smart golden gate-ZeSe/diamond crystal surface and evaporated naturally at room temperature. The spectrum was collected over the wavenumbers ranging from 650 to 4000 cm^{-1}.

Superconducting quantum interference device (SQUID) measurement was carried out as follows: 40 mg of an iron oxide nanoparticle sample was transferred into a plastic capsule. The loaded capsule was contained inside a plastic straw. The loaded straw was placed inside a magnetometer SQUID, using a Quantum Design MPMS XL dc SQUID magnetometer. The magnetization was measured over the temperature range 5 e *T*/K e 300 in an applied field of 1000 Oe. Data were collected after cooling the sample in both zero field (ZFC) and in the measuring field (FC).

It is well accepted that the conformation change of macromolecules can be monitored by circular dichroism (CD) in the far-UV region between 190 and 250 nm. The chromophores at these wavelengths are the peptide bonds, with the signals corresponding to their folding arrangements. Therefore, structures such as α-Helix, ß-sheet, and random coil give rise to characteristic shapes and magnitudes in the CD spectrum. Thus, the CD measurement was conducted as follows: concentrations of 0.1 and 0.01 mg/mL for GC and BSA were prepared in deionized water at pH 7.40. The secondary structures of GC and BSA and their corresponding immobilized colloids

were analyzed by Chirascan & Chirascan-plus CD spectroscopy (Applied Photophysics) at room temperature, using a 10 mm optical path length. Data were obtained from 170 to 300 nm with a CD measured every 1.0 nm with an integration time of 1.0 s, and each experiment was repeated three times.

3.4 Evaluation of Binding Constant of Iron Oxide Immobilized GC-BSA with Drug Molecules

Diazepam, ibuprofen, and warfarin were each prepared as a diluted solution due to their low solubility limit in water. Their concentrations were ca. 0.05, 1, and 0.017 mg/mL, respectively. All the drugs were prepared in 0.1 M phosphate pH 7.4. The amount of drug added to iron oxide/glycol chitosan/bovine serum albumin or iron oxide/glycol chitosan/bovine serum albumin/glycol chitosan/bovine serum albumin nanocomposites was kept at a 1:1 molar ratio. The reaction mixture was heated to 37 ^{o}C for 3 h at pH 7.4. The unbound drug molecules were separated from the solid nanocomposites using a magnet, and their concentration was determined from a calibrated curve using UV-visible spectroscopy (Lambda 19 Spectrometer UV-vis NIFR Perkin-Elmer). A 10 mm × 10 mm × 45 mm quvette was used. On the basis of mass balance, the amount of bound drug can be deduced. The binding reaction between the drug and the BSA is as follows

$$\mathbf{BSA} + \mathbf{Drug} \underset{\leftarrow}{\overset{\rightarrow}{}} \mathbf{BSA \setminus Drug} \qquad \mathbf{(2)}$$

$$K_a$$

The protein-drug binding affinity can be expressed in terms of log K_a value. K_a is the equilibrium value of association which is expressed mathematically below

$$K_a = \frac{[\mathbf{BSA \setminus Drug}]}{[\mathbf{BSA_f}] \times [\mathbf{Drug_f}]} \qquad \mathbf{(3)}$$

Where:

K_a is the affinity constant in dm^3mol^{-1}

[BSA_f] is free BSA in mol dm^{-3}

[$Drug_f$] is free Drug in mol dm^{-3}

[BSA\Drug] is the BSA drug complexe in mol dm^{-3}

The drug binding constant between each drug and free BSA was calculated according to previous UV-visible or other spectroscopic studies, on the basis that the BSA-drug complex can be separated from free drug/ BSA using dialysis[24]. It can be seen from Table 1 that the protein-drug binding log K values of BSA entrapped in iron oxide/GC were very close to the values of the native BSA. This is consistent with the results obtained from the CD study where no conformation change in BSA upon entrapment by iron oxide/GC is deduced. In contrast, the deviations in binding constants were apparent in the case of the direct immobilization of BSA on silica coated iron oxide without the GC template at pH 7.4 (BSA was unable to directly attach on iron oxide under this pH condition).

3.5 Results and Discussion

Figure 10 shows the TEM images of the synthesized nanoparticles. Particle sizes ranged from 9 to 15 nm (most particles lying between 8 and 10 nm) were observed in Figure 11a. This size range falls in a typical size distribution obtained from the precipitation method. An average size of 9.4 nm with fairly narrow size distribution (standard deviation: 1.63 nm) was derived by measuring 300 nanoparticles in the micrographs. The XRD pattern (Figure 11b) of the particles was also collected, which matched the magnetite-based nanoparticles with spinel structure according to the literature.[5,25] The selected area high-resolution TEM and electron diffraction patterns, SAED, of the material shown in Figure 10 matched with the structure derived from the XRD. From the full width at half maximum of the <311> peak in the XRD, an average particle size of 9.2 nm (with standard deviation of 2.5 nm) using Scherrer equation from XRD was obtained.

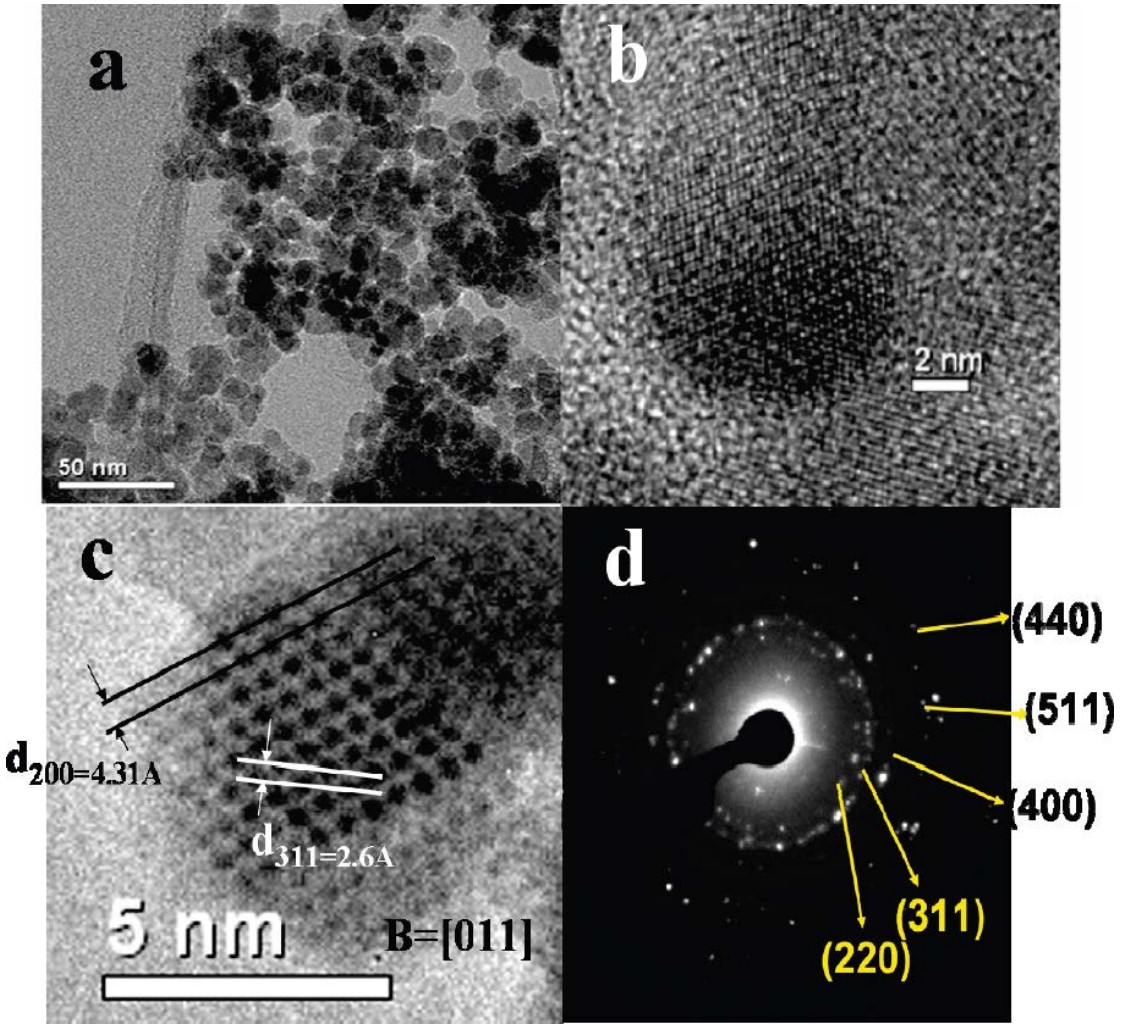

Figure 10. TEM images of (a) the uniform size of magnetite nanoparticles (average 9.4 nm); (b) the high magnification of a single magnetite nanoparticle; (c) the high resolution image where lattice points along the <200> and <311> crystallographic planes are visible; (d) the corresponding SAED pattern and indices.

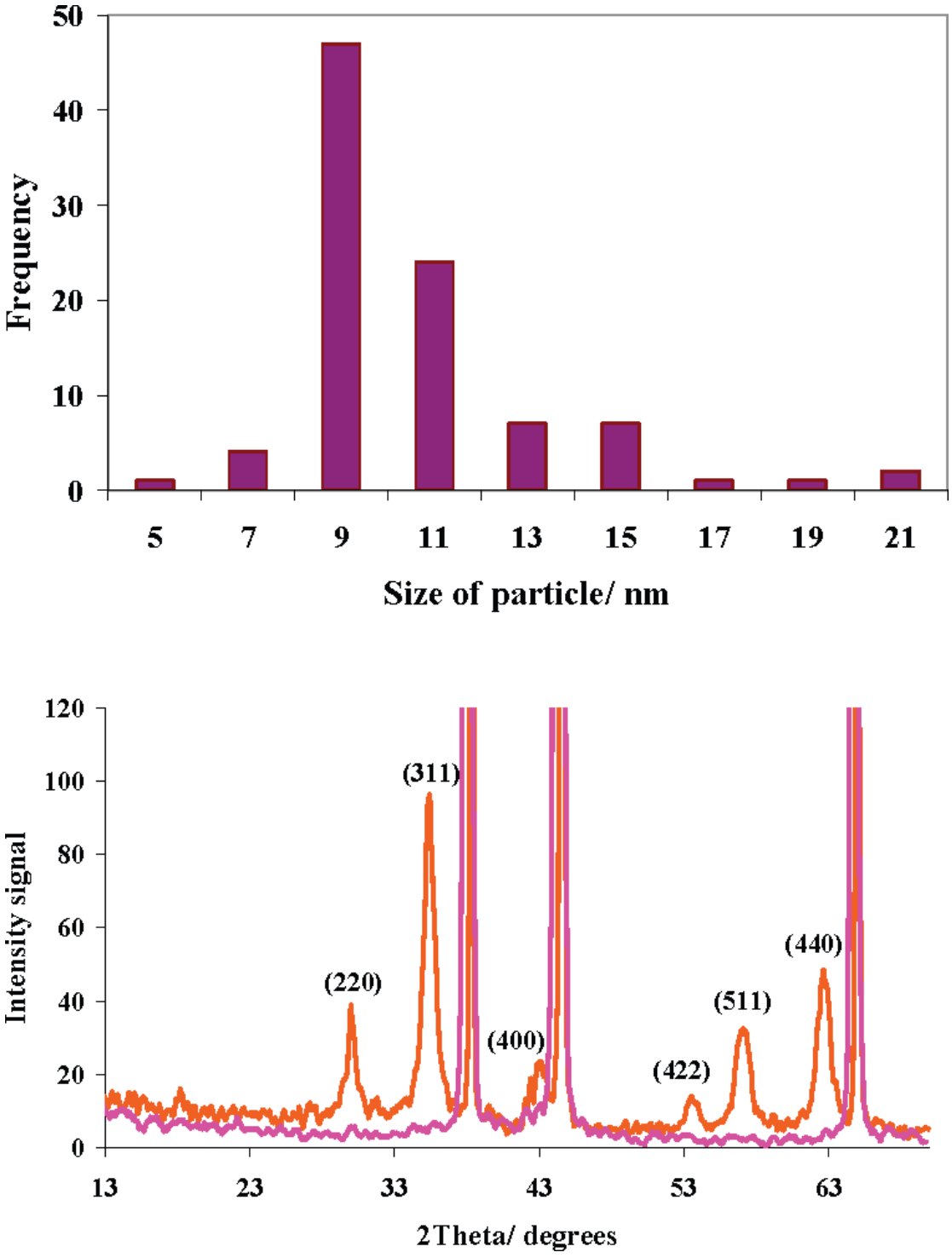

Figure 11. (a) (upper) Size distribution of iron oxide particles from TEM. (b) (lower) XRD diffraction pattern of iron oxide nanoparticles (phases labelled) prepared via coprecipitation and that of the aluminum sample holder (red non-labelled lines).

Magnetic measurements of the particles by vibration saturation magnetization, VSM, shown in Figure 12a indicates that the nanoparticles showed no magnetic hysteresis with both the magnetization and demagnetization curves passing through the origin. This indicates the superparamagnetic nature of the material, such that the magnetic material can only be aligned under an applied magnetic field but will not retain any residual magnetizm upon removal of the field. Superconducting quantum interference device (SQUID) spectra of the iron oxide nanoparticles were taken under an external magnetic field of 1000 Orested, where the two sets of repeated measurements indicated progressive decrease in magnetic moment at increasing temperatures (Figure 12b). Thus, both of these techniques confirmed that the iron oxide nanoparticles are indeed superparamagnetic, giving a high saturation magnetization value (>35 emu g^{-1}) and suitable for repeated magnetic separation. Energy dispersion X-ray analysis, EDX, indicated the composition of 47% oxygen and 53% iron, implying a small degree of oxidation had taken place from magnetite to maghemite phase during the transfer.

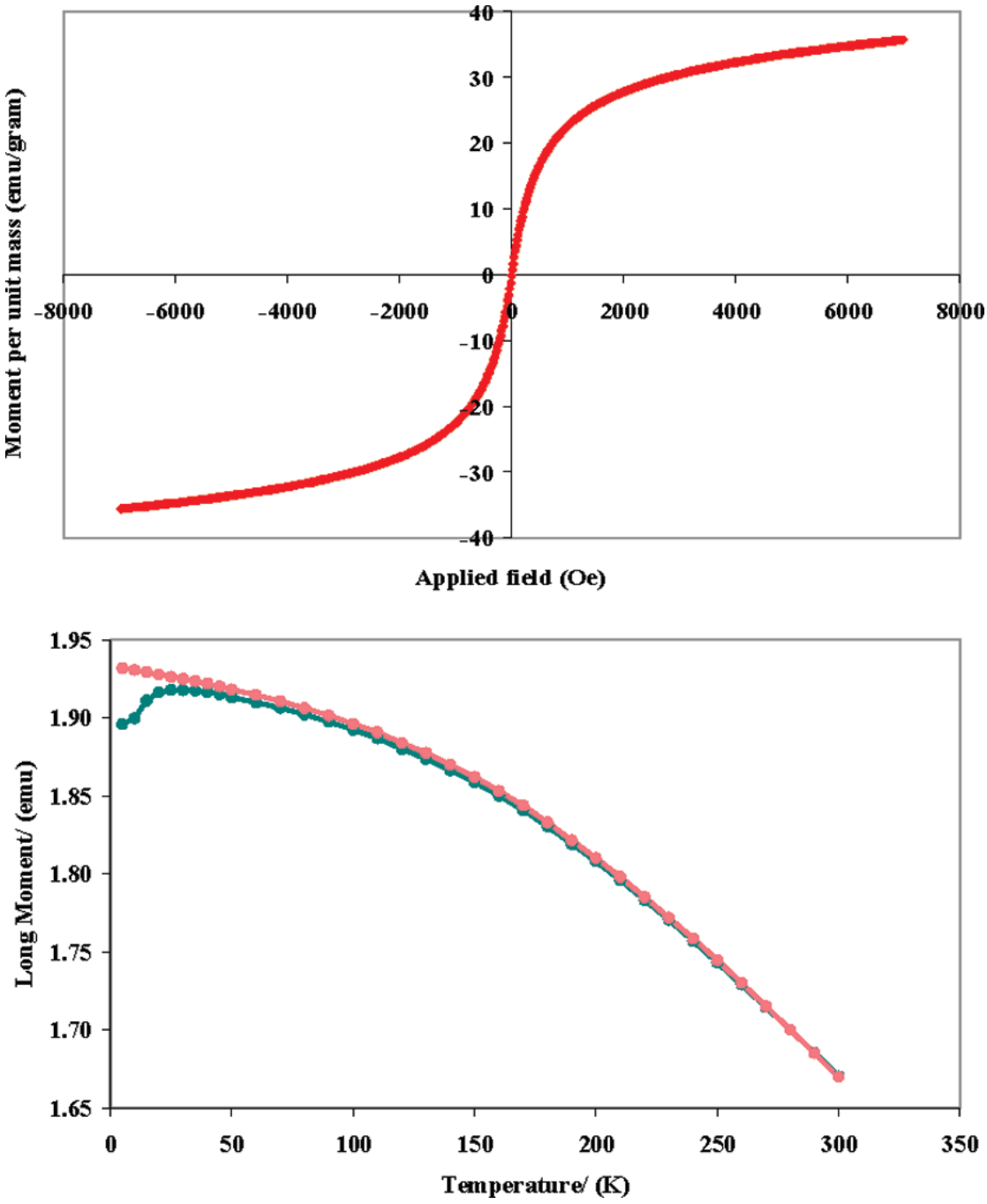

Figure 12. (a) (upper) VSM spectrum of iron oxide where the magnetization line passes through the origin indicative that the sample is superparamagnetic in nature. (b) (lower) Superconducting quantum interference device (SQUID) spectra of the iron oxide nanoparticles were taken under an external magnetic field of 1000 Orested, where the two sets of repeated measurements indicated the progressive decrease in magnetic moment at increasing temperature confirming that the sample is indeed superparamagnetic in nature.

In order to carry out electrostatic deposition of GC and BSA on this magnetic iron oxide, the surface potentials of the particles and the macromolecules at different pH values have been determined. Figure 13 shows the change in zeta potential at different pH values of the iron oxide nanoparticle, GC and BSA, respectively. The isoelectric point is defined as the pH value where the surface potential is zero. As shown in Figure 13, the isoelectric points of iron oxide, GC and BSA are 6.1, 8.8 and 4.9, respectively. These measured values were in agreement with previous reported values.[26] This indicates under normal physiological conditions at pH 7.4 the surfaces of iron oxide nanoparticle and the BSA are both negatively charged. In contrast, GC is positively charged at this pH and therefore, it may be suitable to create alternating layers of GC with BSA on the magnetic iron oxide surface.

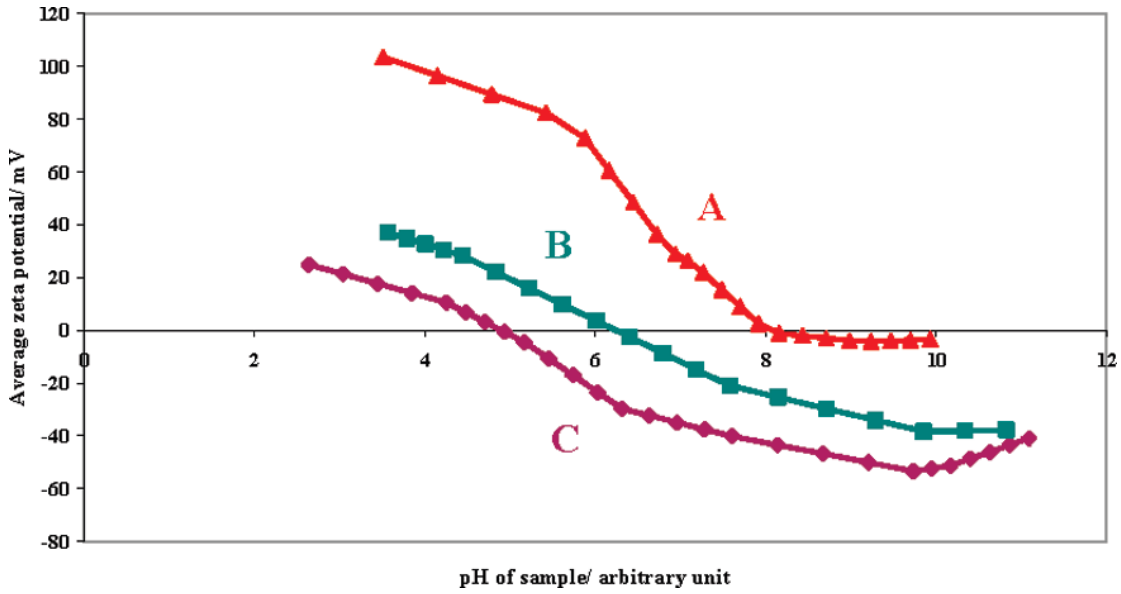

Figure 13. Zeta potential change as a function of pH for (A) GC, (B) iron oxide, and (C) BSA, respectively.

Figure 14 shows dramatic changes in zeta potential of magnetic iron oxide nanoparticles after different pretreatments with GC and BSA solutions followed by magnetic precipitation and rinsing. The negative charge of the naked particle (-22 mV) at pH 7.4 switched to +15 mV when treated with GC solution, implying the iron oxide is likely to be covered with the GC molecules, thus giving the resulting outer surface characteristics of the GC nature. On the other hand, further treatment of the

nanocomposite particles with BSA followed by magnetic precipitation followed by rinsing showed the surface potential of about -15 mV which is considerably lower than that of the naked particle and the BSA surface potentials. This suggests that BSA molecules are entrapping within the GC layer giving the external surface with intermix feature. Interestingly, subsequent treatment with GC reverted to the surface characteristic of the GC layer (+15 mV). The second deposition of BSA again gave the external surface with the same intermix surface potential.

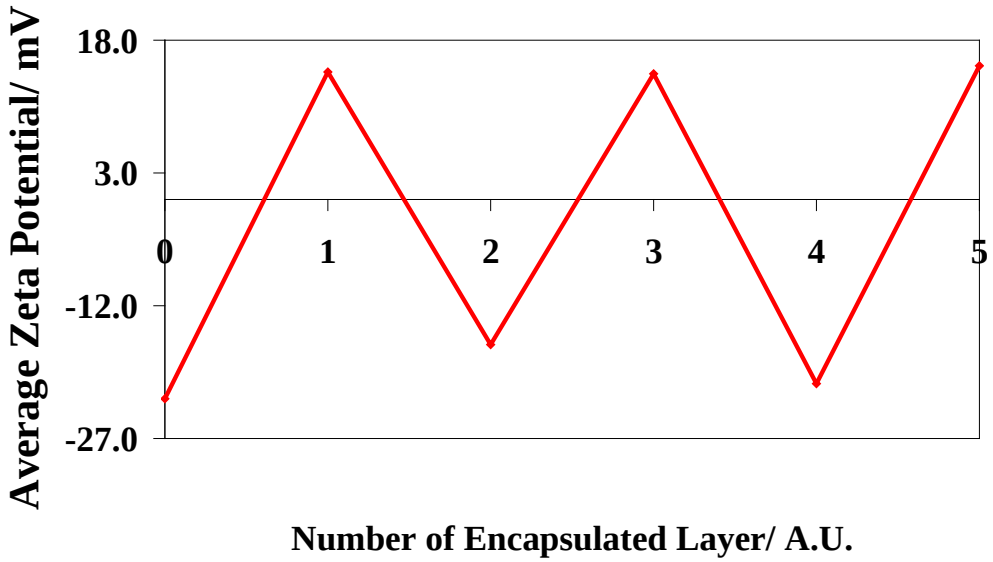

Figure 14. Change in zeta potential of the magnetic iron oxide nanoparticle after different sequential pretreatments with the 1st layer of GC (5.98×10^{-9} mole adsorbed per 3 mg of iron oxide); 1st BSA (3.95×10^{-9} mole); 2nd GC (4.49×10^{-9} mole); 2nd BSA (4.25×10^{-9} mole); and 3rd GC (4.45×10^{-9} mole).

The sequential adsorption values of GC and BSA by 3 mg magnetic iron oxide were monitored by UV-visible absorption at 185 and 190 nm, respectively. Apart from the larger initial value of GC uptake probably due to unselective binding, the subsequent uptakes suggested that the GC and BSA are maintained in nearly 1:1 ratio as shown in Figure 15. As a result, the positively charged GC and negatively charged BSA must form a stoichiometric complex, and their layer-by-layer depositions beyond

monolayer adsorption on a small magnetic vehicle were demonstrated. A separate experiment showed that at pH 7.4 the two species when mixed at 1:1 molar ratio indeed formed a complex, which lead to a dramatic increase in turbidity, while no turbidity change was observed at pH 10.0 and 6.6.

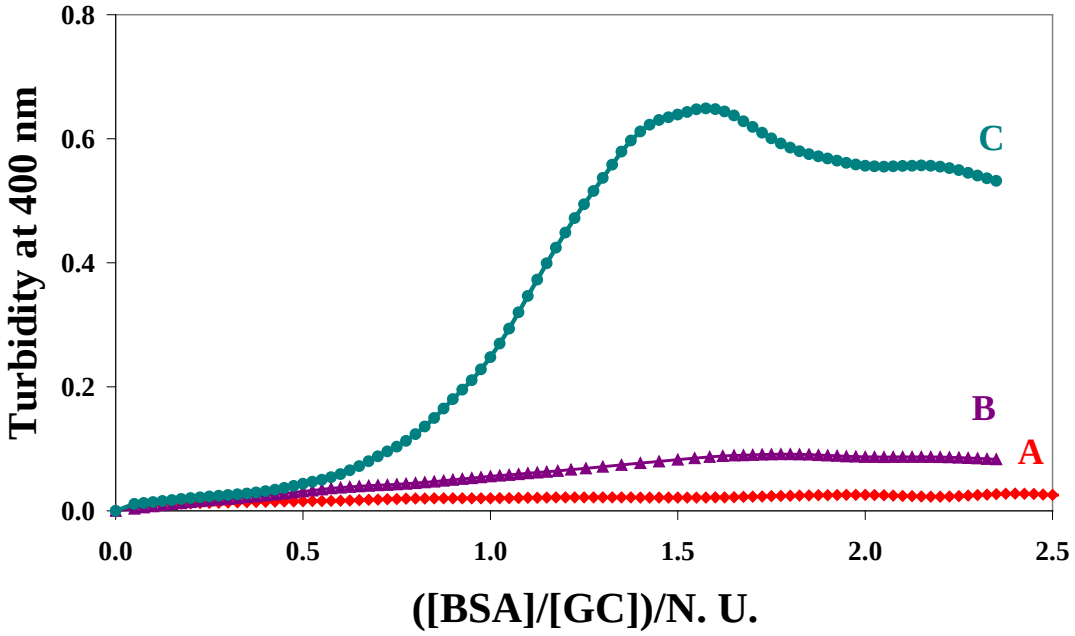

Figure 15. Glycol chitosan/ bovine serum albumin titration observed at 400 nm wavelength at (A) pH 10.0, (B) pH 7.4, and (C) pH 6.6.

Dramatic changes in surface potential of the iron oxide upon adsorptions of GC and BSA at a significant quantity clearly suggest the encapsulation of iron oxide by these macromolecules must take place at high surface coverage. However, it is not yet known whether the encapsulation is homogeneously distributed on the iron oxide surface or preferentially taken on certain sites on the nanoparticle (corners, edges, or terraces).

Figure 16 shows the Fourier transformed infrared spectra of iron oxide immobilized GC and BSA. Both free forms of GC and BSA show amide I (1650 cm^{-1}) and amide II (1540 cm^{-1}) peaks, but the GC exhibits a unique ether linkage feature (peak at about 1050 cm^{-1}), while the BSA shows only the two amide linkages. The FTIR spectrum for the first layer of immobilized GC on iron oxide showed the ether peak at 1050 cm^{-1}, accounting for 40.9% of the total area of the three peaks (spectrum A). The sequential deposition of first BSA layer reduced the relative ether peak area to 27.4% (spectrum B). Depositions of the second layer of GC raised the peak area to 30.6% (spectrum C), followed by decreasing to 24.7% upon the second layer BSA deposition (spectrum D) and finally 25.7% in the third layer of GC (spectrum E). Although it is difficult to correlate the FTIR data with the measured adsorption values (quoted in Figure 6) in a quantitative manner, depositions of GC and BSA multilayers reflected the sum of the characteristic FTIR peaks of their respective forms. Their relative ratios of ether to amide peaks undoubtedly depend on sequential treatments. Therefore it is evident that the GC and BSA were successfully encapsulated on the iron oxide particle. BSA is a sensitive bovine blood protein can easily subject to a conformation change according to a slight change in the environment.(3)

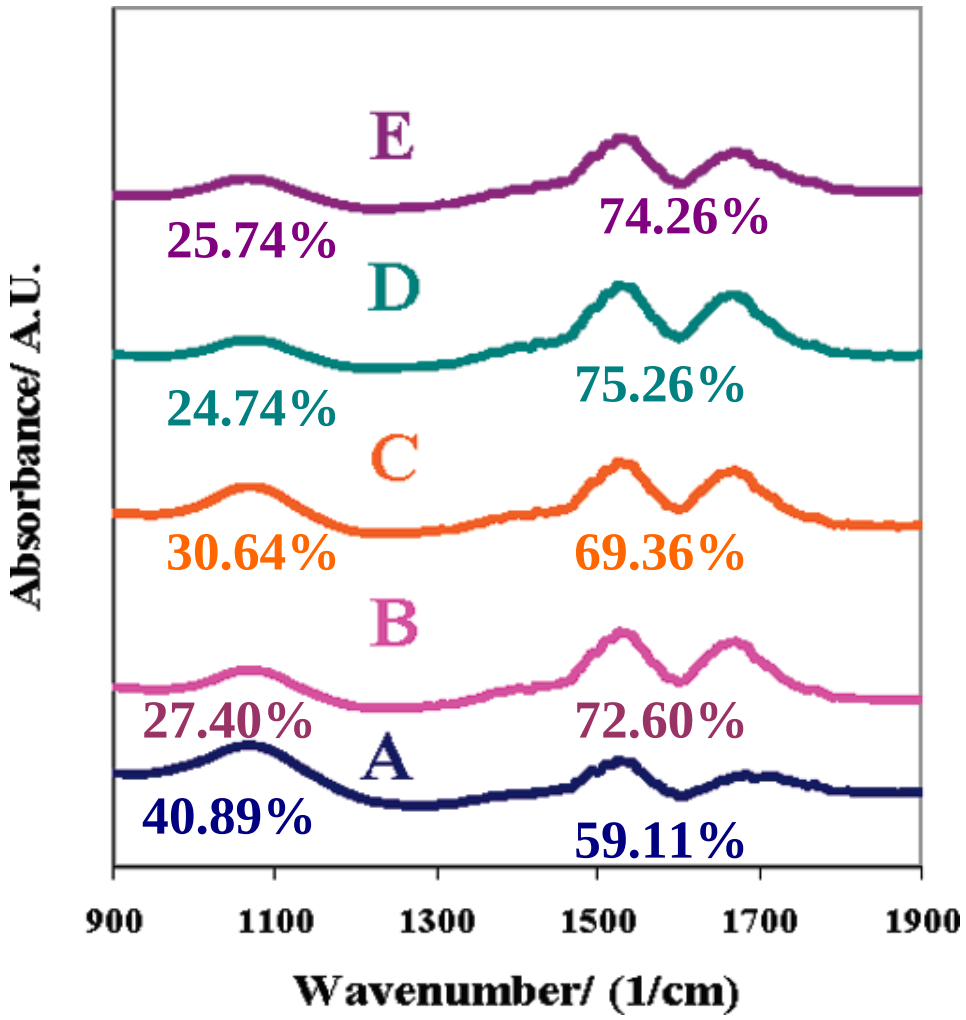

Figure 16. FTIR spectra of the encapsulated iron oxide nanoparticle with five depositions of alternate GC and BSA at pH 7.4. (A) GC; (B) GC + BSA; (C) GC + BSA + GC; (D) GC + BSA + GC + BSA; (E) GC + BSA + GC + BSA + GC.

Figure 17a showed the CD spectra which monitor the confirmation of immobilized BSA on an iron oxide-GC composite and its native free form. Background of iron oxide nanoparticles with and without the GC immobilization is provided. As seen from Figure 17b, the free form of BSA clearly displays an α-helix with three transitions: π to π^* leads to positive absorption perpendicular to the direction of the circular polarized light at 192 nm and transition leads to two negative absorption humps due to π to π^* parallel to the circular polarized light at 209 nm and n to π transition at 222 nm, respectively. It is interesting to note that the immobilized BSA,

both one- (iron oxide/GC/BSA) and two-layered (iron oxide/GC/BSA/GC/BSA), displayed identical negative double humped features as the free BSA, indicative of the retention in their conformation at a high degree. In particular, the inner BSA in the two-layered nanocomposites did not affect the CD spectra, which suggests its coverage by further overlayers (GC/BSA) did not induce much structural alteration. In contrast, direct immobilization of BSA either on naked iron oxide at pH 5.5 as shown in Figure 17b or on silica-coated iron oxide shown in Figure 18 demonstrates an alteration in the BSA conformation.[3] The characteristic three transitions of the α-helix were diminished due to the immobilization. Notice that the native BSA conformation was affected over a wide range of pH. This suggests the present simple immobilization is less hostile to the protein than those of direct immobilization on inorganic-based magnetic particle surfaces.

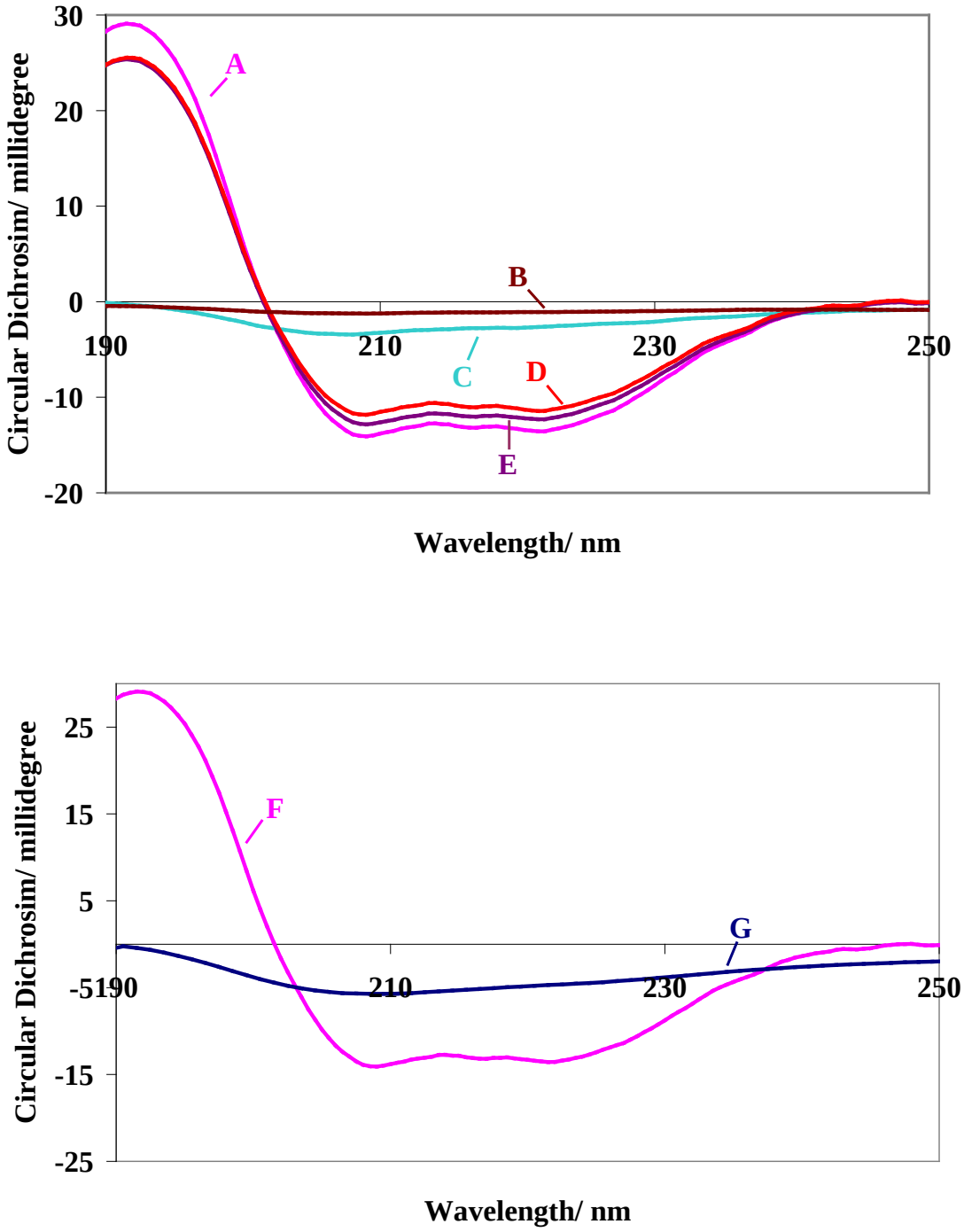

Figure 17. (a) (upper) Normalized CD spectra at pH 7.4: (A) native BSA, (B) naked iron oxide nanoparticles, (C) iron oxide/GC, (D) iron oxide/GC/BSA, and (E) iron oxide/GC/BSA/GC/BSA. (b) (lower) Shows CD spectra: (F) native BSA and (G) iron oxide/BSA at pH 5.5.

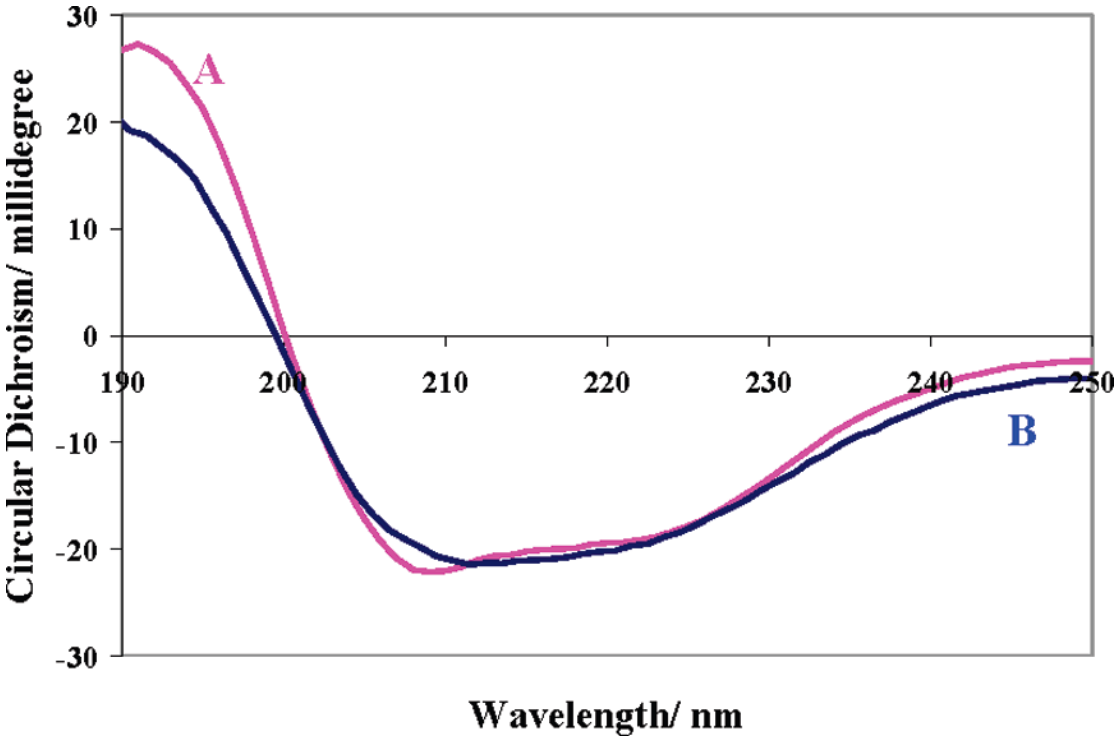

Figure 18. Circular dichroism normalized spectra of (A) native BSA and (B) BSA-bound silica encapsulated iron oxide at pH 7.40 (buffered) showing the smoothing and attenuation in the regions of negative absorption of π to π^* parallel at 209 nm and at 189 nm of BSA upon immobilization on silica.[3]

To confirm the retention of the secondary structure conformation of the immobilized BSA by this electrostatic entrapment with GC on iron oxide nanoparticles, the binding properties of immobilized BSA with small drug molecules compared to native BSA were investigated. According to Curry *et. al.*, the BSA protein molecule has two clearly defined binding sites for small organic molecules; their binding values were highly sensitive to conformation. Accordingly, the binding site of warfarin, shown in figure 19, (site I drug) was located in subdomain II and ibuprofen, shown in figure 20, and diazepam, shown in figure 21, (site II drugs) in site II of subdomain IIIA.[27] Thus, using site I and site II drug molecules, one can differentiate the functionality of these two sites by studying their binding constants. The drug binding property of BSA clearly reflects its biological activity, which is governed by its tertiary structure. The binding affinity between the drug and the protein can be expressed in terms of the log *K* value.[3] The procedure for the measurement of drug binding constant between each drug and free BSA was then carried out according to previous reports.[3,30]

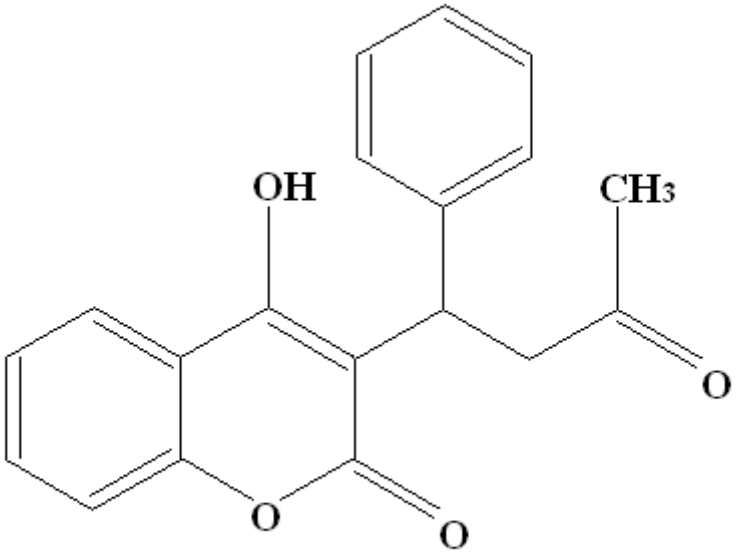

Figure 19. The molecular structure of warfarin.

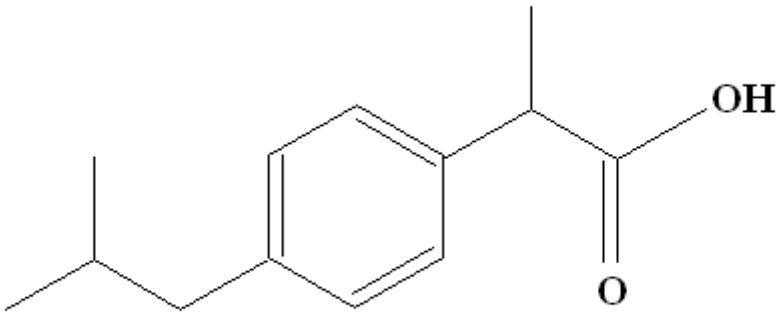

Figure 20. The molecular structure of ibuprofen.

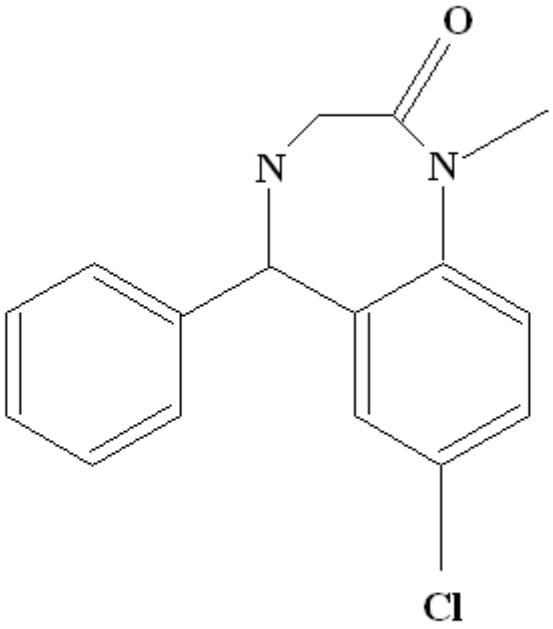

Figure 21. The molecular structure of diazepam.

As seen from Table 1, the protein-drug binding log *K* values of one and two BSA layers entrapped in iron oxide/GC for all three drug molecules showed almost identical log *K* values to the native BSA within experimental error. This information is consistent with the results obtained from CD where no conformation change in BSA upon entrapment by iron oxide/GC by this technique was observed. Since the quantity of BSA in the two-layer nanocomposites was doubled as compared with the single layer, the same drug binding constant obtained clearly implied that the inner BSA binds the same way as the single BSA layer without structural alteration (no change in CD spectra) and diffusion problem (imposed by the GC). Thus, the entrapped proteins within the layers on the composites are still accessible by the small drug molecules. In contrast, the deviations in binding constants were apparent in the case of the direct immobilization of BSA on silica-coated iron oxide without the GC template at pH 7.4, where BSA was unable to attach on iron oxide under this pH condition.

Name of Drug	Log K literature value	Log K iron oxide in SiO_2	Log K iron oxide /GC/BSA	Log K iron oxide /GC/BSA/GC/BSA
Diazepam	4.08[28]	4.59 ± 0.05	4.07 ± 0.05	4.05 ± 0.05
Ibuprofen	4.51[29]	3.93 ± 0.05	4.55 ± 0.05	4.53 ± 0.05
Warfarin	4.46[28]	3.91 ± 0.05	4.55 ± 0.05	4.55 ± 0.05

TABLE 1: Comparison of the Log Binding Constants for Small Drug Molecules of One Immobilized Layer of BSA on Iron Oxide (Fe_3O_4/GC/BSA) and Two Immobilized Layers of BSA on Iron Oxide (Fe_3O_4/GC/BSA/GC/BSA) with Native BSA (Literature Values) and BSA with Silica-Coated Iron Oxide.[a] The protein-drug binding affinity is expressed in terms of the log K_a, where K_a is the equilibrium value of association at pH 7.4.

3.6 Drug binding calculations

The drug binding constants for each drug, diazepam, ibuprofen and warfarin were calculated from the drug binding constant expressed in the following equations:

$$\mathbf{BSA} + \mathbf{Drug} \underset{\leftarrow}{\overset{\rightarrow}{}} \mathbf{BSA \setminus Drug} \qquad \textbf{(7)}$$

$$K_a$$

$$K_a = \frac{[\mathbf{BSA \setminus Drug}]}{[\mathbf{BSA_f}] \times [\mathbf{Drug_f}]} \qquad \textbf{(8)}$$

A calibration curve was constructed to measure the concentration of the initial and the excess drugs and protein. For each drug the calibration curves had shown a straight line with strong regression coefficient values between absorbance and concentration at characteristic wavelength, which agrees with the Beer-Lambert law.

$$[BSA_t] = [BSA_f] + [BSA \setminus Drug] \quad (9)$$

$$[Drug_t] = [Drug_f] + [Drug \setminus BSA] \quad (10)$$

Both [BSA\Drug] and [Drug\BSA] are the same complexes and so:

$$[BSA_f] = [BSA_t] - [BSA \setminus Drug] \quad (11)$$

$$[Drug_t] - [Drug_f] = [Drug \setminus BSA] \quad (12)$$

Substituting (10) in (9) the expression above becomes:

$$[BSA_f] = [BSA_t] - ([Drug_t] - [Drug_f]) \quad (13)$$

$$[BSA_f] = [BSA_t] - [Drug_t] + [Drug_f] \quad (14)$$

Substituting the expression above in (8) the expression becomes:

$$K_a = \frac{([Drug_t] - [Drug_f])}{[Drug_f]([BSA_t] - [Drug_t] + [Drug_f])} \quad (15)$$

Where:

K_a	is the affinity constant in dm^3mol^{-1}
$[BSA_t]$	is total BSA in mol dm^{-3}
$[BSA_f]$	is free BSA in mol dm^{-3}
$[Drug_t]$	is total drug mol dm^{-3}
$[Drug_f]$	is free Drug in mol dm^{-3}
[BSA\Drug]	is the BSA drug complexe in mol dm^{-3}

According to the Beer-Lambert law:

$$\mathbf{A} = \varepsilon \times \boldsymbol{l} \times \mathbf{C} \quad \textbf{(16)}$$

$$\mathbf{C} = \frac{\mathbf{A}}{\varepsilon \times \boldsymbol{l}} \quad \textbf{(17)}$$

Where:

A is absorbance in arbitrary unit

ε is molar absorptivity in $dm^3mol^{-1}cm^{-1}$

l is pathway length in cm

C is the concentration in $moldm^{-3}$

$\mathbf{A_b}$ is absorbance before the experiment in arbitrary unit

$\mathbf{A_a}$ is absorbance after the experiment in arbitrary unit

$$\mathbf{[Drug_t]} = \frac{\mathbf{A_b}}{\varepsilon \times \boldsymbol{l}} \quad \textbf{(18)}$$

$$\mathbf{[Drug_f]} = \frac{\mathbf{A_a}}{\varepsilon \times \boldsymbol{l}} \quad \textbf{(19)}$$

$$\mathbf{[Drug_t]} = \frac{\mathbf{A_a}}{\varepsilon \times \boldsymbol{l}} \quad \textbf{(20)}$$

$$\mathbf{[Drug_t] - [Drug_f] = [BSA \setminus Drug]} \quad \textbf{(21)}$$

$$\mathbf{[BSA \setminus Drug]} = \frac{\mathbf{A_b}}{\varepsilon \times \boldsymbol{l}} - \frac{\mathbf{A_a}}{\varepsilon \times \boldsymbol{l}} \quad \textbf{(22)}$$

$$\mathbf{[BSA \setminus Drug]} = \frac{\mathbf{A_b - A_a}}{\varepsilon \times \boldsymbol{l}} \quad \textbf{(23)}$$

According to equation (11)

$$\mathbf{[BSA_f] = [BSA_t] - [BSA \setminus Drug]}$$

$$\mathbf{[BSA_f] = [BSA_t] - (\frac{A_b - A_a}{\varepsilon \times l})} \quad \textbf{(24)}$$

Substituting equation equations (18), (19), and (24) in (15) the expression becomes

$$K_a = \frac{(\frac{A_b - A_a}{\varepsilon \times l})}{(\frac{A_a}{\varepsilon \times l}) \times ([BSA_t] - (\frac{A_b - A_a}{\varepsilon \times l})} \quad (25)$$

The mathematical expression above simplifies to:

$$K_a = \frac{(A_b - A_a)}{(A_a) \times ([BSA_t] - (\frac{A_b - A_a}{\varepsilon \times l})} \quad (26)$$

$$\text{Drug binding constant} = -\log K_a \quad (27)$$

$$\text{Drug binding constant} = -\log(\frac{(A_b - A_a)}{(A_a) \times ([BSA_t] - (\frac{A_b - A_a}{\varepsilon \times l})}) \quad (28)$$

3.7 Conclusion

In conclusion, it was shown that alternate layer-by-layer depositions of GC and BSA can take place on the magnetic iron oxide nanoparticle surface, as evidenced from zeta potential, UV-vis adsorption, and FTIR spectroscopy. Thus, the entrapment of the protein molecules by aminocarbohydrate polymers through the alternate mild electrostatic interactions greater than monolayer adsorption on the magnetic carrier was evidenced. The formation of this assembly was pH dependent, a result of which the assembled layer could be unstable leading to a cascade release of the protein molecules for potential delivery purpose.[31] Preliminary experiment suggested 75% of the entrapped BSA molecules can be released from the iron oxide/GC/BSA composites to the solution upon acid treatment (pH = 2.5). In addition, circular dichroism spectroscopy and binding constant measurements with small molecules suggested that the conformation of the entrapped BSA by this new but simple immobilization method is still maintained at high integrity. In contrast, direct immobilization of BSA on naked inorganic iron oxide or silica-coated iron oxide covered with high coverage of strong inorganic oxide or hydroxyl sites (hard Lewis and Bronsted groups) altered its secondary structure, which lead to deactivation in activity. In terms of potential applications, we present a new strategy to immobilize and store protein molecules beyond monolayer adsorption on a magnetic nanoparticle surface without much structural alteration. Such immobilization may facilitate the transport of protein molecules and maintain biological activity by a nanosize magnetic vehicle.

3.8 References

(1) J. F. Berret, N. Schonbeck, F. Gazeau, D. El Kharrat, O. Sandre, A. Vacher, M. Airiau, J. Am. Chem. Soc. 2006, 128, 1755-1761.

(2) C. H. Dodd, H. C. Hsu, W. J. Chu, P. G. Yang, H. G. Zhang, J. D. Mountz, K. Zinn, J. Forder, L. Josephson, R. Weissleder, J. Immunol. Methods. 2001, 256, 89-105.

(3) C. H. Yu, A. Al-Saadi, S-J. Shih, L. Qiu, K. Y. Tam, S. C. Tsang, J. Phys. Chem. C. 2009, 113, 537-543.

(4) S. J. Son, J. Reichel, B. He, M. Schuchman, S. B. Lee, J. Am. Chem. Soc. 2005, 127, 7316-7317.

(5) S. C. Tsang, C. H. Yu, X. Gao, K. Tam, J. Phys. Chem. B. 2006, 110, 16914-16922.

(6) T. J. Yoon, J. S. Kim, B. G. Kim, K. N. Yu, M. H. Cho, J. K. Lee, Angew. Chem. Int. Ed. 2005, 44, 1068-1071.

(7) T. Neuberger, B. Schopf, H. Hofmann, M. Hofmann, B. von Rechenberg, J. Magn. Mag. Mater. 2005, 293, 483-496.

(8) A. K. Gupta, A. S. G. Curtis, J. Mater. Sci. 2004, 15, 493-496.

(9) L. R. Hirsch, R. J. Stafford, J. A. Bankson, S. R. Sershen, B. Rivera, R. E. Price, J. D. Hazle, N. J. Halas, J. L. West, P. Natl. Acad. Sci. USA 2003, 100, 13549-13554.

(10) M. Slim, N. Durisic, P. Grutter, H. F. Sleiman, Chem. Biochem. 2007, 8, 804-812.

(11) A. Azioune, A. Ben Slimane, L. A. Hamou, A. Pleuvy, M. M. Chehimi, Perruchot C, Armes S.P, Langmuir 2004, 20, 3350-3356.

(12) C. Beck, W. Hartl, R. Hempelmann, Angew. Chem. Int. Ed. 1999, 38, 1297-1300.

(13) J. Wang, Small. 2005, 1, 1036-1043.

(14) T. Schalkhammer, Monatshefte. Fur. Chemie. 1998, 129, 1067-1092.

(15) A. Kondo, F. Murakami, K. Higashitani, Biotechnol. Bioeng. 1992, 40, 889-894.

(16) A. Kondo, S. Oku, F. Murakami, K. Higashitani, Colloids. Surf. B Biointerfaces, 1993, 1, 197-201.

17) H. Larsericsdotter, S. Oscarsson, J. Buijs, J. Colloid Interface Sci. 2005, 289, 26-35.

(18) A. Dyal, K. Loos, M. Noto, S. W. Chang, C. Spagnoli, K. V. P. M. Shafi, A. Ulman, M. Cowman, R. J. Gross, J. Am. Chem. Soc. 2003, 125, 1684-1685.

(19) D. Ma, M. Li, A. J. Patil, S. Mann, Adv. Mater. 2004, 16, 1838-1841.

(20) H. H. Yang, S. Q. Zhang, X. L. Chen, Z. X. Zhuang, J. G. Xu, X. R. Wang, Anal. Chem. 2004, 76, 1316-1321.

(21) S. Giri, B. G. Trewyn, M. P. Stellmaker, V. S. Y. Lin, Angew. Chem. Int. Ed. 2005, 44, 5038-5044.

(22) G. Decher, Science. 1997, 277, 1232-1237.

(23) F. Caruso, H. Mohwald, J. Am. Chem. Soc. 1999, 121, 6039-6046.

(24) Y. Cheng, E. Ho, B. Subramanyam, J. L. Tseng, J. Chromatogr. B, 2004, 809, 67-73.

(25) C. H. Yu, K. Y. Tam, C. C. H. Lo, S. C. Tsang, IEEE, T. Magn. 2007, 43, 2436-2438.

(26) J. Rangsansarid, K. Fukada, J. Colloid Interface Sci. 2007, 316, 779-786.

(27) C. E. Petersen, C. E. Ha, S. Curry, N. V. Bhagavan, Proteins 2002, 47, 116-125.

(28) C. Dufour, O. Dangles, BBA-GEN Subjects 2005, 1721, 164-173.

(29) P. Sun, A. Hoops, R. A. Hartwick, J. Chromatogr. B. 1994, 661, 335-340.

(30) M. Tanaka, Y. Asahi, S. Masuda, T. Ota, Chem. Pharm. Bull. 1991, 39, 1-4.

(31) A. M. Derfus, G. von Maltzahn, T. J. Harris, T. Duza, K. S. Vecchio, E. Ruoslahti, S. N. Bhatia, Adv. Mater. 2007, 19, 3932-3936.

Chapter Four

Synthesis of Magnetic Fe_3O_4 in ZnS Nanoparticles

Contents

4.1 Overview

Here we report, *for the first time* the synthesis of a magnetic Fe_3O_4 particle encapsulated in porous, photocatalytically active ZnS as a core/ shell structure. The average size of the particles is in the nano region with a large surface area to volume ratio, giving high catalytic activity. Each particle is stabilised by poly(N-vinyl-2-pyrrolidone) (PVP) to prevent agglomeration in solution. This synthetic method can keep the particles in a highly dispersed colloidal form, which is essential for maximizing the UV excitation during photocatalytic reactions. The intrinsic energy gap of ZnS between the ground state and excited state is also increased due to the synthesised particles in nanometric regime as compared to bulk material. Incorporating a magnetic core can clearly facilitate separation, recovery and reuse of the composite materials, hence widening the practical applications of ZnS based materials.

4.2 Introduction

The use of transition metal ZnS based materials in photocatalysis has attracted increasing attention over the past few decades. Particularly, the tailoring of size, shape and structure of zinc sulphide based materials allows fine-tuning of its semiconducting and photocatalytic properties. [1-11] ZnS was one of the most widely studied materials for photocatalytic reduction of CO_2, [12- 20] photocatalytic reduction of toxic halogenoalkanes, photocatalytic production of H_2 from water, [21-30] and photodegradation of organic pollutants, etc. [31-44] Previous studies clearly indicated that the unique photocatalytic effect of ZnS is the result of a rapid and efficient generation of electrons and holes over the material upon irradiation than other candidates. This photo-catalytic excitation is demonstrated to be more efficient than conventional excitation methods such heating or electrical means. Electrons at high energy band states of a n-type semiconductor including the ZnS can be generated by the photo-excitation in the UV region although the use of visible excitation source is mostly preferred. Some studies reported exciting shifts in absorption bands towards visible region by doping the ZnS nanoparticle with various metal ions such as Eu^{3+}, Ni^{2+}, Mg^{2+}, Cu^{2+}, etc. [45- 58] However, the estimated operational cost of using ZnS is still very high as the nanosize ZnS is difficult to be recovered, and unprotected ZnS, if used is also easily dissolved in solution due to photo-corrosion. Thus, the search for a new method in retaining ZnS based nanocatalysts by reversible magnetic precipitation in solution could create a major impact in these areas. Furthermore, a porous nature of high surface area ZnS layer may be useful to entrap chemicals and biochemicals of interests. Such materials and associated technology may find exciting applications in chemical and biomedical areas. For example, photo-excitation of radicals over these materials to attack target sites i.e. cancer cells in living tissue can be pursued. The recovery of ZnS based materials may be achieved by incorporating a superparamagnetic centre into the ZnS as a core-shell structure, which is the focus of this chapter.

The uses of magnetic nanoparticles in chemical, mechanical and biomedical areas are wide ranging. Iron oxide is of particular interests due to its ease availability and have been exploited for many applications including ferro-fluids,[59-67] magnetic density

storage,[68] magnetic resonance imaging,[69-78] tissue engineering, [79-93] bio-separation,[94-109] cancer therapy hyperthermia, etc.[110-120] There are two forms of iron oxides that can be co-existed at ambient conditions, namely, γ-Fe_2O_3 (maghemite) the most stable form and Fe_3O_4 (magnetite). Both forms display typical ferromagnetic properties, but the maghemite gives a slightly lower magnetic saturation value (M_{sat}) when an external magnetic field is applied. As their particle size is synthesised below 20-30 nm a single magnetic moment exhibiting superparamagnetic behaviour can be obtained. This size dependent magnetic behaviour is extensively explored for magnetic storage and drug delivery applications. [121, 122]

In this chapter, the study to place iron oxide nanoparticle as a core material in porous ZnS is described.

4.3 Experimental Section

Preparation of iron oxide nanoparticles: Iron (II) chloride ($FeCl_2$) and iron (III) chloride ($FeCl_3$) were purchased from Sigma-Aldrich Chemical Co., USA. Deionised water was used in all experiments. Iron oxide nanoparticles were produced by precipitation of iron (II) and iron (III) chlorides in aqueous solution with the addition of ammonium hydroxide solution following with extensive washings to remove impurities prior to their encapsulation in ZnS. The preparation of ZnS nanoparticles was carried out using zinc acetate, thiourea, ethylene glycol and poly(N-vinyl-2-pyrrolidone), see figure 1. PVP (99% purity, M_W= 40000) was obtained from Sigma-Aldrich Chemical Co., USA, without further purification.

The detailed synthesis procedure adopted in this thesis is given as follows: Iron oxide nanoparticles were produced by co-precipitation method in aqueous medium according to the balanced chemical equation (1). Iron (II) chloride (1.7 g) and iron (III) chloride (2.7 g) were dissolved in 200 mL of deionised water at 50 °C and stirred for 1 h under a nitrogen atmosphere before the addition of 4 mL of (35% w/w) ammonium hydroxide solution. This solution was added in sequential portions (0.1 mL) over a constant period of time with stirring. The initial yellow/ orange color of

the iron (II) and iron (III) solution turned to dark brown precipitate upon the addition of 35% ammonium hydroxide solution (4 mL). The solution was allowed to stir for further 1 h before it was separated from solution by centrifugation. The nanoparticles were washed in deionized water followed by centrifugation three times.

$$Fe^{2+}_{(aq)} + 2Fe^{3+}_{(aq)} + 8OH^{-}_{(aq)} \rightarrow Fe_3O_{4(s)} + 4H_2O_{(l)} \quad (1)$$

The above experimental procedure was adopted from a published method.[30] ZnS nanoparticles were then synthesised by thermolysis of zinc precursor in the presence of ethylene glycol. Thus, zinc acetate (6 mmol) and thiourea (12 mmol) were dissolved in ethylene glycol (150 mL) and PVP was added as a stabiliser (5.0 g). The mixture was stirred until a clear solution was obtained before it was heated to 180 ^{o}C. The hot solution turned milky white after 5 minutes, indicating the formation of ZnS nanoparticles. The temperature of the reaction was kept at 180 ± 3 ^{o}C for 7 h. Over this time, the colour of the solution became slightly yellow. The mixture was allowed to cool to room temperature with stirring and the formed ZnS nanoparticles were separated by centrifugation, washed with deionised water and ethanol to remove the excess PVP. The ZnS nanoparticles were air dried overnight.

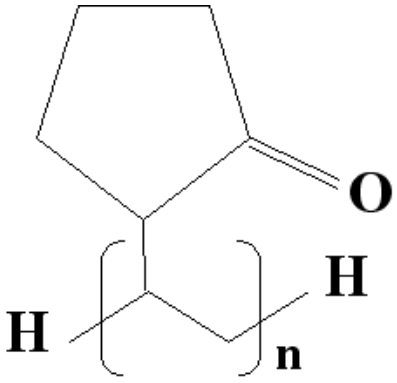

Figure 1. Repeated unit structure of poly(*N*-vinyl-2-pyrrolidone) (PVP).

Nanosize iron oxide in porous ZnS (iron oxide/ZnS) was synthesised by combining the two procedures with the first preparation of iron oxide, followed by the preparation steps of ZnS. Thus, iron oxide nanoparticles acted as seeds for the formation of ZnS material on them as so called 'seed-mediated growth method'. [123, 124] The self nucleated ZnS nanoparticle without the iron oxide core can be selectively

removed by magnetic means as only the encapsulated iron oxide in ZnS can be magnetically precipitated. Diagrammatic representations of the experimental procedure are shown in figure 2 and 3.

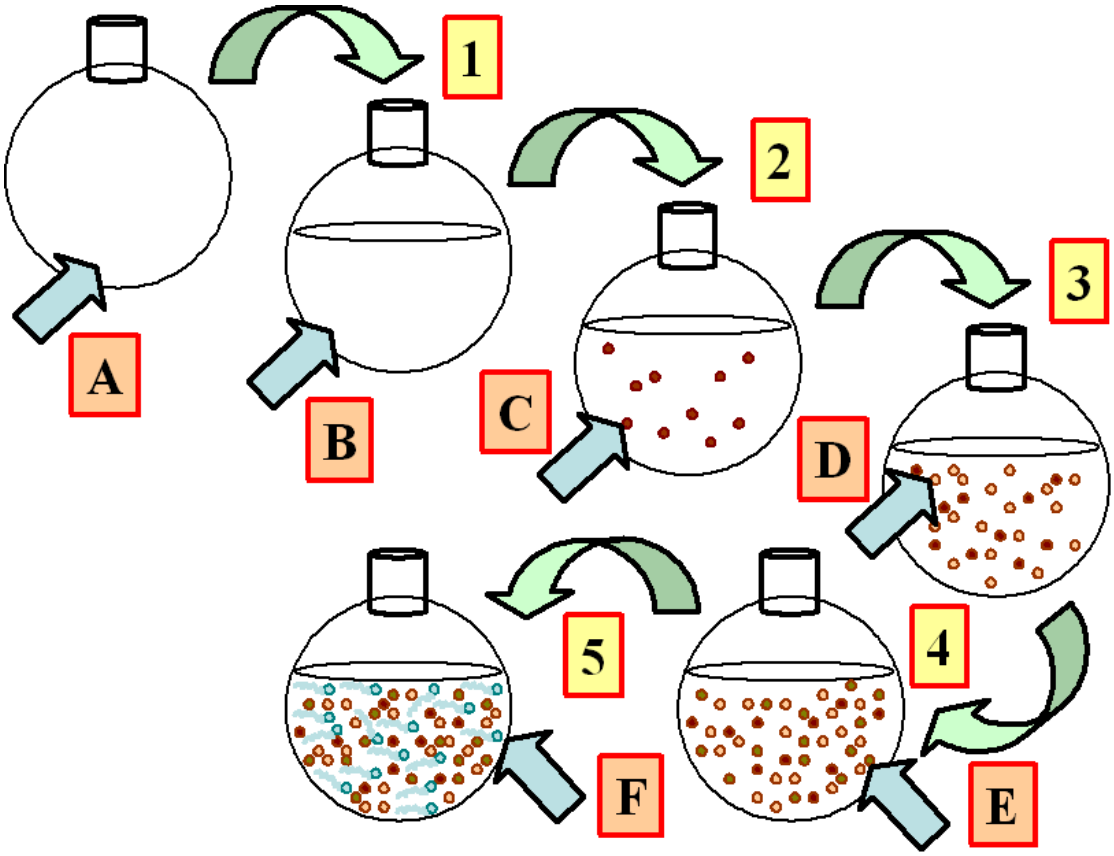

Figure 2 shows the first stage in preparation of encapsulated iron oxide in zinc sulphide. The step 1) solvent in a round bottom flask A) with ethylene glycol B), step 2) the addition of iron oxide nanoparticle C), step 3) the addition of zinc acetate D), step 4) the addition of thiourea E) and step 5) the addition of PVP stabiliser.

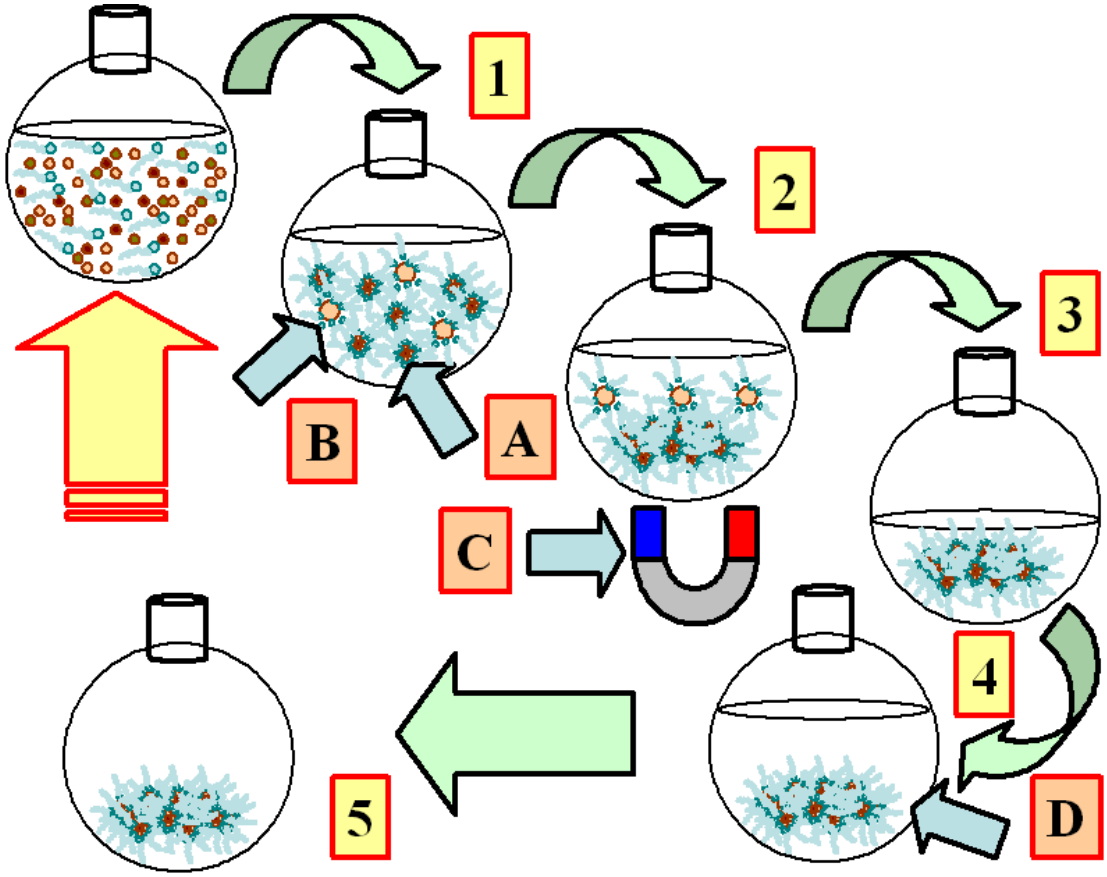

Figure 3 shows the two stage preparation of encapsulated iron oxide in zinc sulphide. The step 1) heating the reaction solution in round bottom flask to produce encapsulated iron oxide nanoparticle A) and free ZnS nanoparticles B), step 2) separation of encapsulated iron oxide nanoparticles from ZnS nanoparticles using a magnet C), step 3) decanting the impure solution, step 4) washing the nanoparticles with deionised water and ethanol D) and step 5) centrifugation and drying of the sample particles.

A JEOL 3000 XL electron microscope operated at 200 KV and fitted with energy dispersive for SAED analysis and X-ray analyzer (Phoenix) for EDX analysis was used. The TEM images showed that the average particle size of as-prepared iron oxide was 14.4 nm. Similarly, an average 70nm aggregated ZnS and 52.8 nm particles of iron oxide in ZnS were also observed.

The samples were also characterised by X-ray powder diffraction (XRD) using the Philips XRD diffractometer. Lambda 19 UV-Vis/ NIR spectrophotometer was used to collect the UV spectra of all the samples synthesised in this work.

4.4 Results and Discussion

The samples of ZnS nanoparticles and iron oxide were synthesised according to the methods described. The morphology and structure of the both particles prepared were characterised by a TEM technique at both low and high magnifications. The ZnS nanpaarticle was prepared by the thermolysis of zinc acetate in the presence of poly(N-vinyl-2-pyrrolidone) (PVP). The PVP was added to prevent the aggregation of ZnS nanoparticles. The molar ratio of PVP to zinc precursor at 0.06:1 was used according to a published study.[30] The iron oxide in ZnS sample was prepared with 40:1 mass ratio of iron oxide and ZnS. This large ratio was used to ensure the homogeneous encapsulation without much self nucleation of the ZnS.

Figure 4a shows the typical TEM image of ZnS nanoparticles and Figure 5a shows the corresponding size histogram of ZnS nanoparticles. The average particle size of ZnS was 70 nm with a broad size distribution (standard deviation: 11.9 nm). These data was based on the measurements of over 300-400 nanoparticles from the corresponding TEM images.

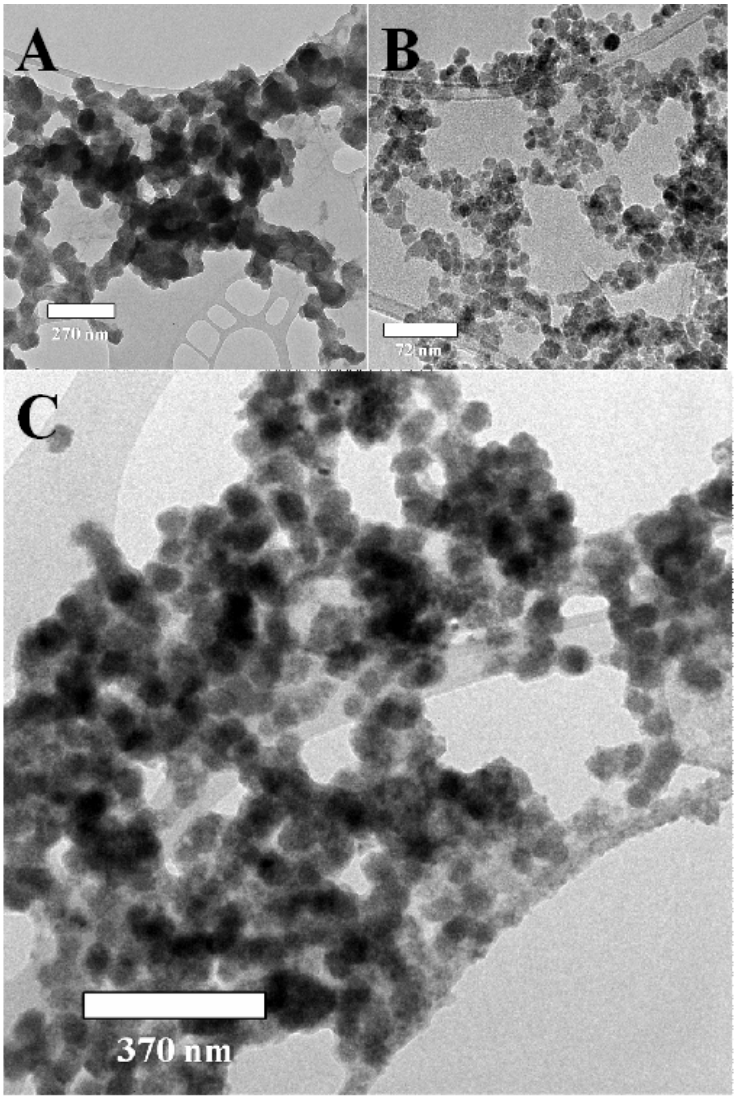

Figure 4 (a) TEM characterisation of ZnS nanoparticles; (b) iron oxide nanoparticles and (c) encapsulated iron oxide in ZnS.

Figure 4b shows the typical TEM image of iron oxide nanoparticles, which indicates that the particles were well dispersed with a narrow size distribution. Figure 5b shows the particle size histogram of the iron oxide particles. The average size was 14.4 nm with a standard deviation of 2.8 nm.

The large differences in size and distribution between these two materials could be due to the fact that ZnS is more thermal and photosensitive than iron oxide leading to a severe degree of aggregation. It is interesting to note that Figure 4c shows the TEM image of encapsulated iron oxide in ZnS as a core/shell structure with the average size

of 52.8 nm. Figure 5c reveals that the composite particles are characterised with a broader degree of size distribution (standard deviation: 9.05 nm). The average size of the ZnS coating on iron oxide appeared to be smaller than those of the ZnS nanoparticles. This could be attributed to the introduction of smaller nuclei of iron oxide particles to initate the growth of ZnS.

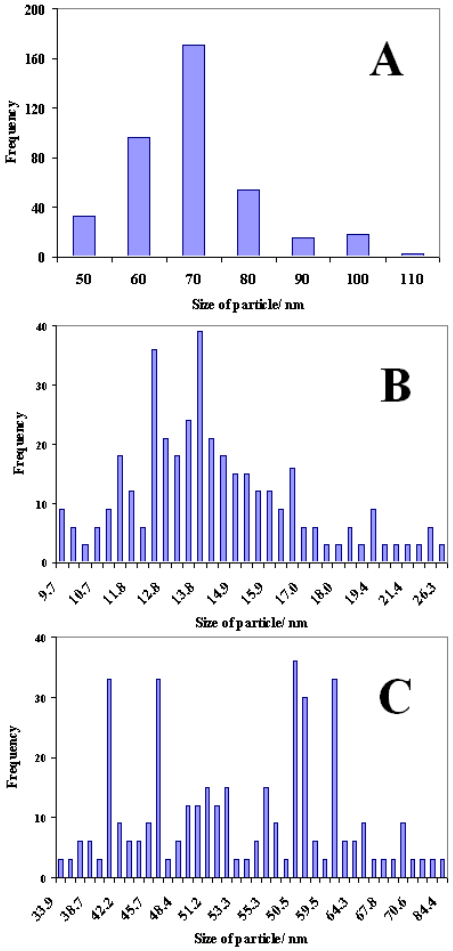

Figure 5 shows the size distribution of ZnS nanoparticle at a), iron oxide nanoparticle at b) and encapsulated iron oxide in ZnS nanoparticle at c).

Selected-area electron diffractions (SAED) of iron oxide and ZnS were presented in Figure 6. The SAED concentric rings of ZnS nanoparticles shown in Figure 6a indicate a low degree of crystallinity of the highly porous material. The diffraction rings were indexed to (100), (002), (110), and (112) planes of ZnS. On the other hand, the concentric rings for the iron oxide with some bright spots suggested a highly crystalline material, as shown in Figure 6b. The diffraction rings were indexed to

(111), (220), (311), (400), (422), (511) and (440) planes of the iron oxides. Figure 6c shows the SAED of the encapsulated iron oxide in ZnS, which gives mixed concentric rings of the porous ZnS with sharp spots of small crystallites of iron oxide.

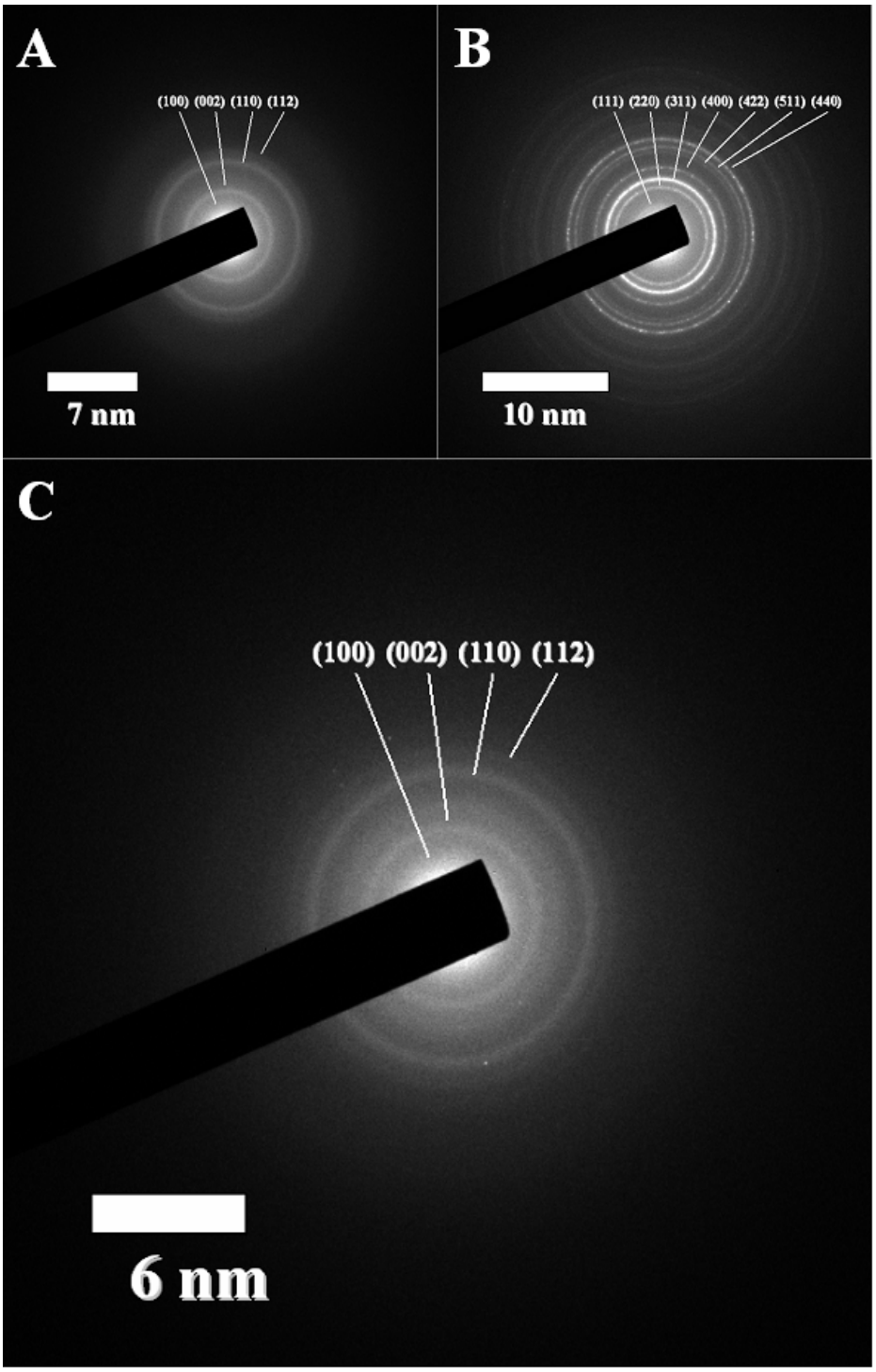

Figure 6 (a) shows the SAED of ZnS nanoparticle; (b) iron oxide nanoparticles and (c) encapsulated iron oxide in ZnS.

Figure 7, Figure 8a and 8b present XRD patterns for iron oxide, ZnS nanoparticles and encapsulated iron oxide in ZnS, respectively. There are seven reflection peaks at 2θ values of 18.075°, 30.075°, 35.375°, 43.175°, 53.675°, 57.275° and 62.675° in the Figure 7 corresponding to (111), (220), (311), (400), (422), (511) and (440) diffraction planes of iron oxide, respectively. Theses peaks correspond to the magnetite particles with a spinel structure, which is in agreement with the previously reported studies.[125- 135] Using the full width at half maximum analysis of the (311) peak, the average size of the nanoparticles was calculated to be 15.6 nm from the Scherrer equation. This is comparable to the average size of 14.4 nm derived from the TEM analysis. Figure 8a presents the XRD pattern peaks of the hexagonal ZnS.[136-145] Three major peaks appear at 2θ value of 28.675°, 47.675° and 55.925° corresponding to (002), (110) and (112) of the ZnS phase, respectively. Identical XRD patterns for iron oxide encapsulated in ZnS were shown in Figure 8b. The XRD peaks for the iron oxide were not seen due to the domination of ZnS and the low concentration of iron oxide. The size of ZnS particles was estimated from the (002) peak broadening, which indicated approximately 2 nm particle size was formed. This value was in agreement with those derived from the high resolution TEM images (highlighted as white circles) shown in Figure 9a and 9c. The small ZnS nanoparticles with poor crystallinity appear to aggregate to form a highly porous of ZnS interconnected material.[30] The diffraction patterns of ZnS nanoparticles with and without iron oxide core were found to be identical due to the dominant ZnS phase.

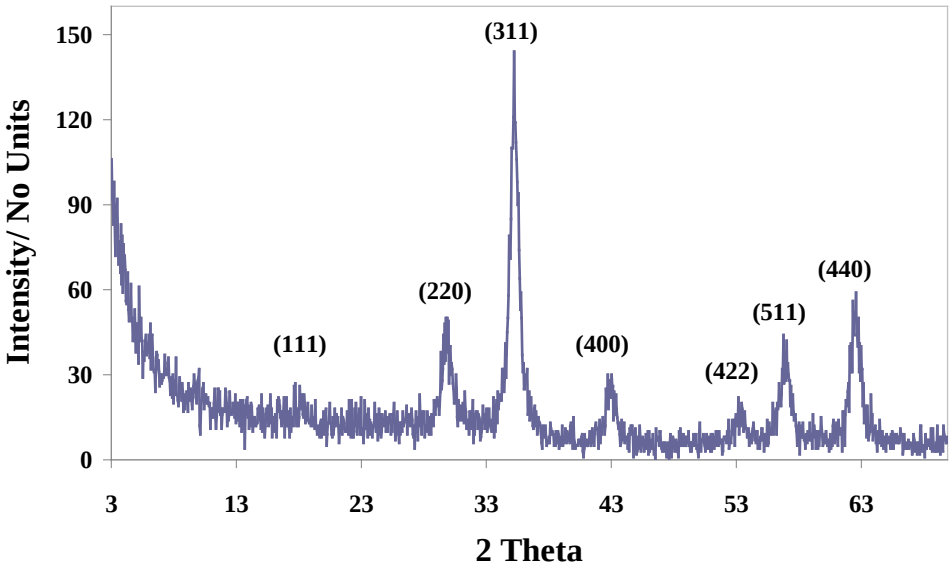

Figure 7 shows the XRD patterns of iron oxide nanoparticles acquired at room temperature.

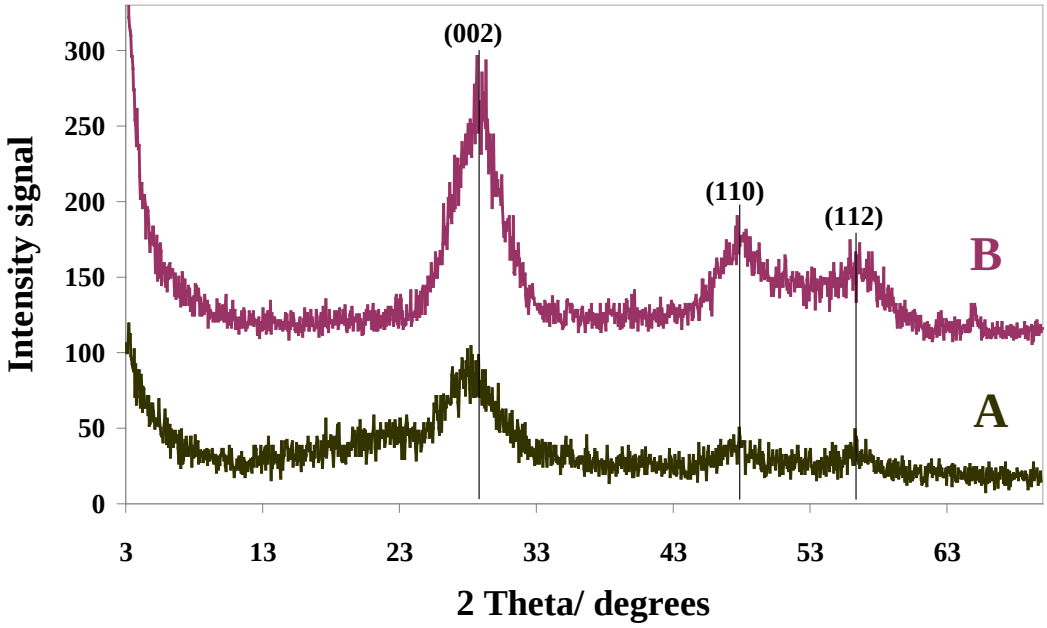

Figure 8 shows the XRD patterns of ZnS acquired at room temperature B) and that of encapsulated iron oxide in ZnS at room temperature A).

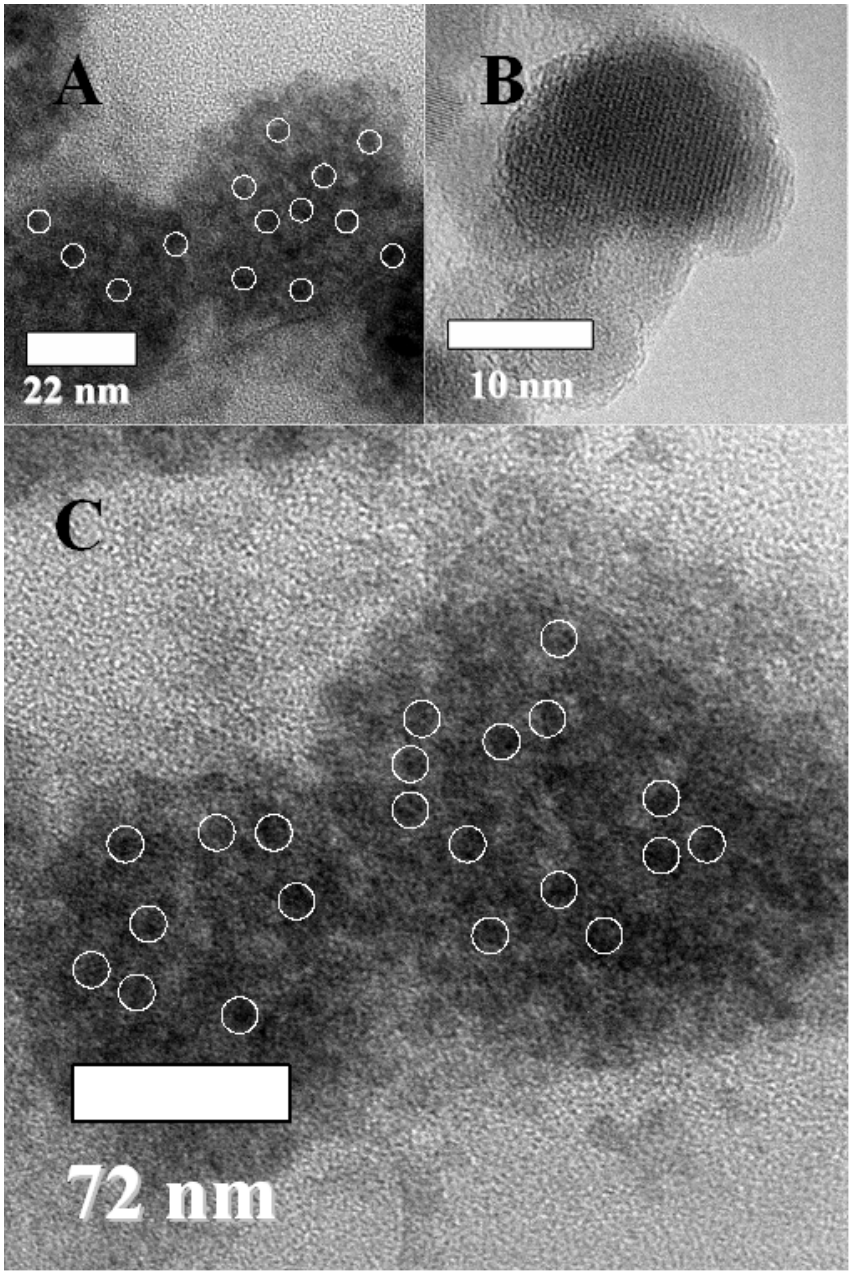

Figure 9 shows the high resolution TEM images of a) ZnS nanoparticle, b) iron oxide nanoparticle and c) encapsulated iron oxide in ZnS nanoparticle.

Energy-dispersive X-ray (EDX) analysis of iron oxide showed the presence of the two elements, the Fe and O. Similarly, two elements, namely Zn and S were detected in the case of ZnS sample. Fe, O, Zn and S were clearly identified in those samples containing encapsulated iron oxide in ZnS, as shown in Figure 10. It should be noted that C, O and Cu were also present in all samples due to the use of carbon-coated copper TEM grid as the sample holder (with oxygen-containing functionalities on the

carbon surface). The composition of ZnS particles was estimated to contain 47% to 53% ratio of sulphur to zinc as compared to the theoretical values of 33.9% to 67.1%. The discrepancy was due to the presence of sulphur as a contaminant in the zinc acetate starting material that accounted for the higher atomic weight ratio of sulphur to zinc. The composition of iron oxide was estimated to contain 63.8% (Fe) to 36.2% (O) atomic ratio, as shown in Figure 10b. This ratio of Fe/O was slightly lower compared to the theoretical values of Fe_3O_4 of 72.4% to 27.6%. The higher oxygen content in our sample was due to the some degree of air oxidation of magnetite to maghemite. Figure 10c shows the EDX spectra of encapsulated iron oxide in ZnS, the atomic ratio of iron to oxygen was 50.1% to 49.9% respectively, and that of sulphur to zinc was 73.0% to 27.0% respectively as a result of the presence of the sulphur contaminant. It was envisaged that the excess S was derived from the use of thiourea.

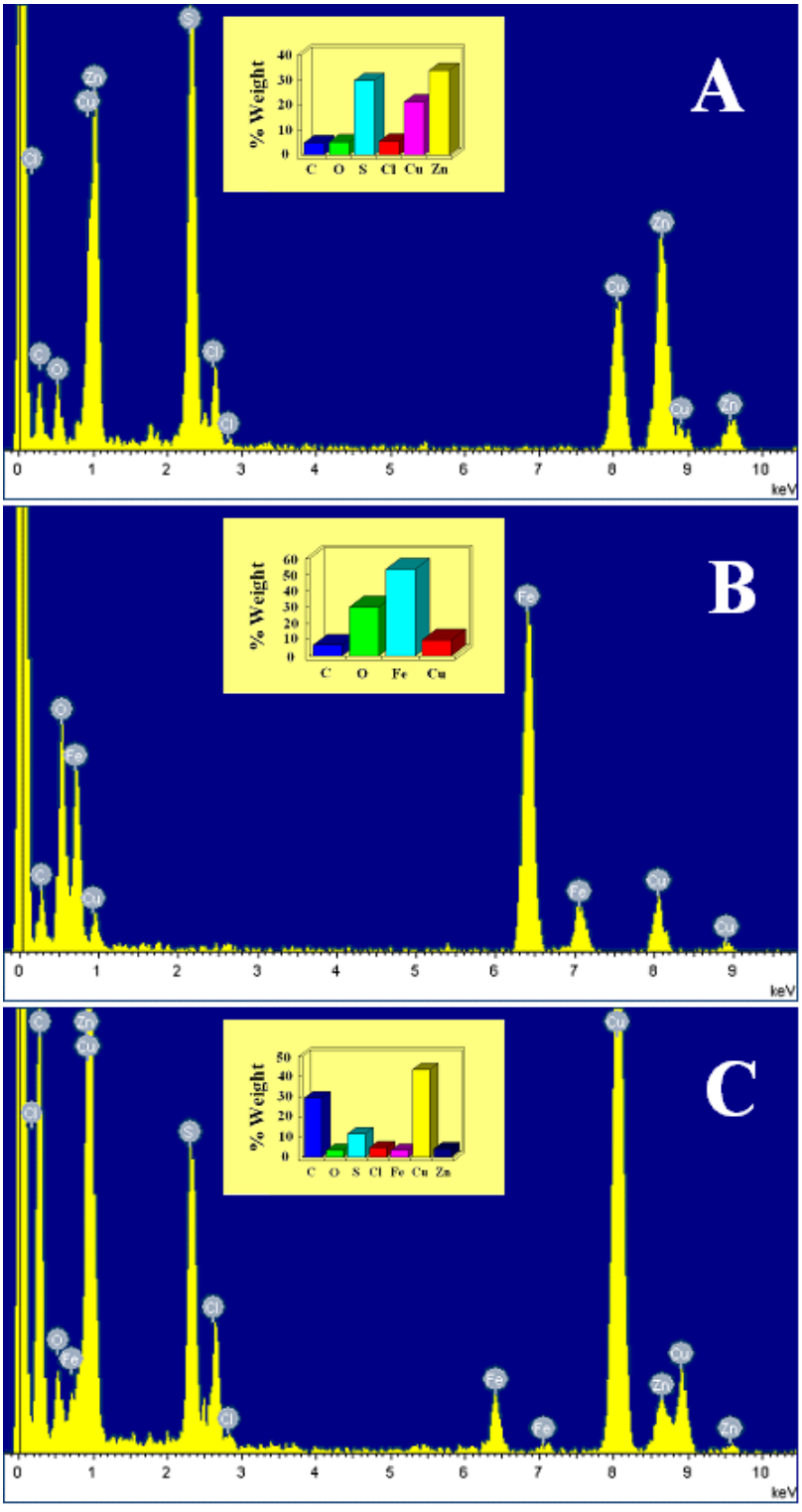

Figure 10 shows the EDX spectra for a) ZnS nanoparticles, b) iron oxide nanoparticle and c) encapsulated iron oxide in ZnS nanoparticle.

Further proof of the encapsulation of iron oxide in ZnS was obtained by using the attenuated total reflection Fourier transformer infrared spectroscopy (ATR-FTIR).

Three major characteristic peaks are shown in Figure 11 A. The broad band located at 3400 cm^{-1} can be attributed to the vibration mode of υ (OH) of water adsorbed in the porous material. The peaks at 1560 cm^{-1} and 1450 cm^{-1} can be attributed to the asymmetric and symmetric stretching modes of the carboxylate, which came from the use of zinc acetate for the sol-gel synthesis of ZnS. [146] The peaks at 680 cm^{-1} is assigned to the Zn-S bond stretching vibrations, which are in agreement with the previously reported value. [147] Figure 11 B shows FTIR spectra of encapsulated iron oxide in ZnS, which is similar to that of pure ZnS nanoparticles with relatively lower intensity peaks. This shows a successful encapsulation of the iron oxide in ZnS. It is noted that iron oxide as a control shows no characteristic peak at the regions of 3400 and 680 cm^{-1} in its FTIR spectrum, as shown in Figure 11 C.

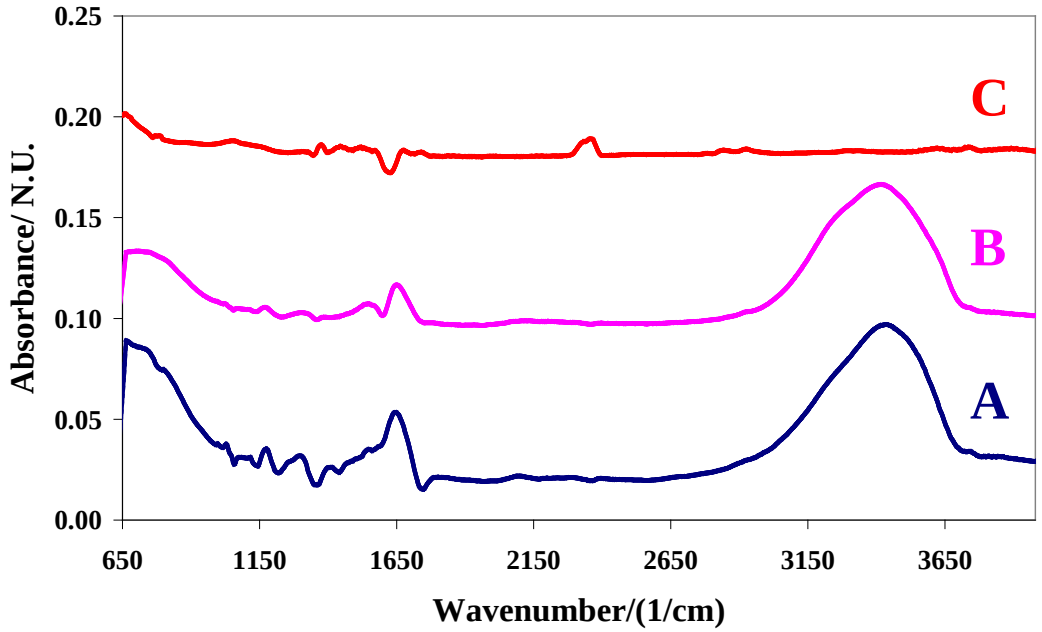

Figure 11 shows the ATR-FTIR spectra for (A) ZnS nanoparticles, (B) encapsulated iron oxide in ZnS, (C) naked iron oxide nanoparticles.

Figure 12 shows the UV spectra of the corresponding three samples. An observed peak in Figure 12 a at 190 nm is assigned to the electron transition from HOMO to LUMO excitation of nanosize ZnS as compared to the 345 nm of the bulk ZnS due to quantum confinement effect in the nano regime.[148] A similar peak also appears but with a slight shift to the longer wavenumber for the encapsulated iron oxide in ZnS shown in Figure 12 b. On the other hand, pure iron oxide shows no characteristic

peaks but a continuous absorption drift due to its opaque optical properties (Figure 12 c). The characteristic absorption peak of iron oxide in ZnS clearly suggests the maintenance of intrinsic optical properties of ZnS in the core/shell structure of iron oxide in ZnS. Although we have neither carried out further photocatalytic study for this new composite material nor assessing its magnetic recovery due to the time constraint of this DPhil work, the novel synthesis is clearly accomplished.

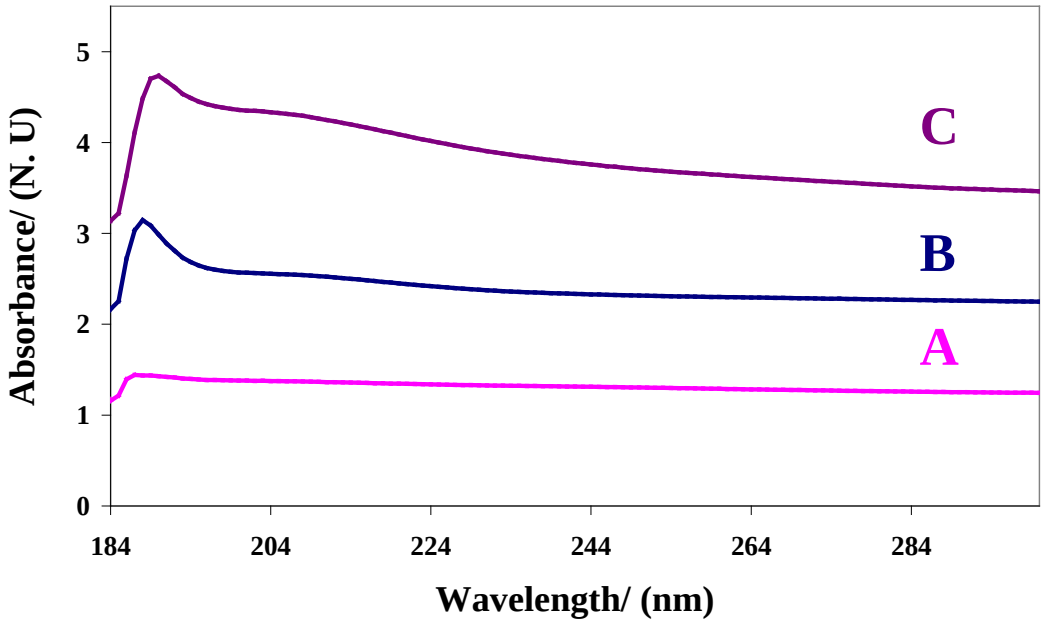

Figure 12 shows the UV spectra for (A) naked iron oxide nanoparticle, (B) ZnS nanoparticle and (C) encapsulated iron oxide nanoparticle in ZnS.

4.5 Conclusions

A simple seed mediated method for the preparation of encapsulated iron oxide in porous ZnS is reported in this chapter. The composite nanoparticles are uniform and spherical in shape. It is found that such engineered particles can retain the intrinsic physiochemical properties of ZnS and can be magnetically separated due to the presence of iron oxide. It is anticipated that this new composite can offer a major technical advantage over the other ZnS based photocatalysts in recycling the material after a photocatalysis reaction by cost effective magnetic means.

4.6 References

(1) P. P. Hankare, P. A. Chate, D. J. Sathe, *J. Alloy. Comp*. **2009**, *487*, 367-369.

(2) I. Tsuji, H. Kato, A. Kudo, *Angew. Chem. Int. Ed*. **2005**, *44*, 3565-3568.

(3) R. E. Galian, M. Guardia, J. Perez-Prieto, *J. Am. Chem. Soc*. **2009**, *131*, 892.

(4) T. Torimoto, T. Adachi, K. Okazaki, M. Sakuraoka, T. Shibayama, B. Ohtani, A. Kudo, S. Kuwabata, *J. Am. Chem. Soc*. **2007**, *129*, 12388-12389.

(5) J. H. Song, T. Atay, S. F. Shi, H. Urabe, A. V. Nurmikko, *Nano. Lett*. **2005**, *5*, 1557-1561.

(6) A. I. Kryukov, N. P. Smirnova, A. V. Korzhak, A. M. Eremenko, and S. Ya. Kuchmii, *Theor. Exp. Chem*, **1997**, *33*, 30.

(7) I. Tsuji, H. Kato, H. Kobayashi, A. Kudo, *J. Am. Chem. Soc*. **2004**, *126*, 13406-13413.

(8) R. Freeman, T. Finder, I. Willner, *Angew. Chem. Int. Ed*. **2009**, *48*, 7818.

(9) P. T. Snee, R. C. Somers, G. Nair, J. P. Zimmer, M. G. Bawendi, D. G. Nocera, *J. Am. Chem. Soc*. **2006**, *128*, 13320.

(10) J. A. Hansen, R. Mukhopadhyay, J. O. Hansen, K. V. Gothelf, *J. Am. Chem. Soc*. **2006**, *128*, 3860.

(11) T. Pons, I. L. Medintz, X. Wang, D. S. English, H. Mattoussi, *J. Am. Chem. Soc*. **2006**, *128*, 15324-15331.

(12) H. Fujiwara, H. Hosokawa, K. Murakoshi, Y. Wada, S. Yanagida, *Langmuir*. **1998**, *14*, 5154-5159.

(13) H. Ohde, M. Ohde, F. Bailey, H. Kim, C. M. Wai, *Nano. Lett*. **2002**, *2*, 721-724.

(14) L. G. Wang, S. J. Pennycook, S. T. Pantelides, *Phys. Rev. Lett*. **2002**, *89*, 075506.

(15) H. Fujiwara, H. Hosokawa, K. Murakoshi, Y. Wada, S. Yanagida, T. Okada, H. Kobayashi, *J. Phys. Chem. B*. **1997**, *101*, 8270-8278.

(16) H. Yoneyama, *Catal. Today*. **1997**, *39*, 169-175.

(17) O. K. Varghese, M. Paulose, T. J. LaTempa, C. A. Grimes, *Nano. Lette*. **2009**, *9*, 731.

(18) Masakazu Anpo, *Bull. Chem. Soc. Jpn*. **2004**, *77*, 1427-1442.

(19) T. W. Woolerton, S. Sheard, E. Reisner, E. Pierce, S. W. Ragsdale, F. A. Armstrong, *J. Am. Chem. Soc*. **2010**, *132*, 2132.

(20) C. J. Wang, R. L. Thompson, J. Baltrus, C. Matranga, *J. Phys. Chem. Lett*. **2010**, *1*, 48-53.

(21) D. W. Hwang, H. G. Kirn, J. S. Lee, J. Kim, W. Li, S. H. Oh, *J. Phys. Chem. B*, **2005**, *109*, 2093-2102.

(22) S. M. Lam, J. C. Sin, A. R. Mohamed, *Recent. Pat. Chem. Eng*. **2008**, *1*, 209-219.

(23) J. M. Herrmann, C. Guillard, P. Pichat, *Catal.Today*, **1993**,*17*, 7.

(24) A. Koca, M. Sahin, *Int J. Hydrogen Energ*. **2002**, *27*, 363-367.

(25) F. Lakadamyali, E. Reisner, *Chem. Commun.* **2011**, *47*, 1695-1697.

(26) I. Tsuji, H. Kato, H. Kobayashi, A. Kudo, *J. Am. Chem. Soc*. **2004**, *126*, 13406-13413.

(27) H. Kato, K. Asakura, A. Kudo, *J. Am. Chem. Soc*. **2003**, *125*, 3082-3089.

(28) F. E. Osterloh, *Chem. Mater*. **2008**, *20*, 35-54.

(29) A. J. Bard, M. A. Fox, Acc. *Chem. Res*. **1995**, *28*, 141.

(30) J. S. Hu, L. L. Ren, Y. G. Guo, H. P. Liang, A. M. Cao, L. J. Wan, C. L. Bai. *Angew. Chem. Int. Ed*. **2005**, *44*, 1269-1273.

(31) S. D. Miao, Z. M. Liu, B. X. Han, H. W. Yang, Z. J. Miao, Z. Y. Sun, *J. Colloid. Interf. Sci*. **2006**, *301*, 116-122.

(32) C. Kim, S. J. Doh, S. G. Lee, S. J. Lee, H. Y. Kim, *Appl. Catal. A-Gen* . **2007**, *330*, 127-133.

(33) F. L. Zhang, J. C. Zhaoa, T. Shen, H. Hidakab, E. Pelizzettic, N. Serponed, *Appl. Catal. B- Environ*. **1998**, *15*, 147-156.

(34) S. H. Zhou, A. K. Ray, *Ind. Eng. Chem. Res*. **2003**, *42*, 6020-6033.

(35) M. Ghiaci, M. E. Sedaghat, H. Aghaeia, A. Gilb, *J. Chem. Technol. Biotechnol*. **2009**, *84*, 1908–1915.

(36) V. Goetz, J. P. Cambon, D. Sacco, G. Plantard, *Chem. Eng. Process*. **2009**, *48*, 532-537.

(37) D. Wang, Y. H. Zou, S. C. Wen, D. Y. Fan, *Appl. Phys. Lett*, **2009**, *95*, 012106.

(38) C. He, D. Shu, M. H. Su, D. H. Xia, M. Abou Asi, L. Lin, Y. Xiong, *Desalination*. **2010**, *253*, 88-93.

(39) J. Senthilnathan, L. Philip, *Chem. Eng. J*. **2010**, *161*, 83–92.

(40) R. T. Koodali, D. Zhao, *Energy. Environ. Sci*. **2010**, *3*, 608-614.

(41) R. A. Doong, T. C. Hsieh, C. P. Huang, *Sci. Total. Environ*. **2010**, *408*, 3334–3341.

(42) M. A. Gondal, M. N. Sayeed, *J. Environ. Sci. Heal. A*. **2008**, *43*, 70–77.

(43) J. M. Dona, C. Garriga, J. Arana, J. Perez, G. Colon, M. Macias, J. A. Navio, *Res. Chem. Intermediat*. **2007**, *33*, 351-358.

(44) A. Kudo, M. Sekizawa, *Catal. Lett*. **1999**, *58*, 241-243.

(45) W. Q. Peng, G. W. Cong, S. C. Qu, Z.G. *Wang, Opt. Mater*. **2006**, *29*, 313-317.

(46) M. Ahmadi, S. Javadpour, A. Khosravi, A. Gharavi, *Jpn. J. Appl. Phys*. **2008**, *47*, 5089-5092.

(47) M. Logar, B. Jancar, A. Recnik, D. Suvorov, *Nanotechnology*. **2009**, *20*, 275601.

(48) P. Yang, M. K. Lu, D. Xu, D. R. Yuan, C. F. Song, S. W. Liu, X. F. Cheng, *Opt. Mater*. **2003**, *24*, 497-502.

(49) D. D. Papakonstantinou, J. Huang, P. Lianos, *J. Mater. Sci. Lett*. **1998**, *17*, 1571-1573.

(50) P. H. Borse, N. Deshmukh, R. F. Shinde, S. K. Date, S. K. Kulkarni, *J. Mater. Sci*. **1999**, *34*, 6087-6093.

(51) P. Yang, M. K. Lu, D. Xu, D. L. Yuan, G. J. Zhou, *Chem. Phys. Lett*. **2001**, *336*, 76-80.

(52) K. Manzoor, S. R. Vadera, N. Kumar, T. R. N. Kutty, *Mater. Chem. Phys*. **2003**, *82*, 718-725.

(53) C. Corrado, Y. Jiang, F. Oba, M. Kozina, F. Bridges, J. Z. Zhang, *J. Phys. Chem. A*. **2009**, *113*, 3830-3839.

(54) L. W. Zhu, P. Chen, Y. Guo, Y. Y. Song, X. D. Xue, X. B. Cao, Colloid. Surface. A. 2010, 360, 111-119.

(55) H. Soni, M. Chawda, D. Bodas, Mater. Lett. 2009, 63, 767-769.

(56) P. Yang, M. Lu, D. Xu, D. Yuan, J. Chang, G. Zhou, M. Pan, *Appl. Phys. A-Mater*. **2002**, *74*, 257-259.

(57) A. Koca, M. Sahin, *Int. J. Hydrogen Energy*. **2002**, *27*, 363-367.

(58) X. F. Wang, J. J. Xu, H. Y. Chen, *J. Phys. Chem. C*. **2008**, *112*, 17581- 17585.

(59) A. P. Liu, X. Li, L. H. Duan, G. P. Qin, H. H. Guo, *J. Supercond. Nov. Magn* . **2010**, *23*, 967-970.

(60) P. Bian, T. J. McCarthy, *Langmuir*. **2010**, *26*, 6145-6148.

(61) L. Slavov, M. V. Abrashev, T. Merodiiska, C. Gelev, R. E. Vandenberghe, I. Markova-Deneva, I. Nedkov, *J. Magn. Magn. Mater*. **2010**, *322*, 1904-1911.

(62) O. E. Ayala-Valenzuela, J. A. Matutes-Aquino, J. T. E. Galindo, C. E. Botez. *J. Appl. Phys*. **2009**, *105*, 07B524.

(63) N. Jain, Y. J. Wang, S. K. Jones, B. S. Hawkett, G. G. Warr, *Langmuir*. **2010**, *26*, 4465- 4472.

(64) T. Hosono, H. Takahashi, Y. Sato, K. Tohji, B. Jeyadevan, *Water. Dynamics*. **2007**, *898*, 135-138.

(65) A. Grants, A. Irbitis, G. Kronkalns, M. M. Maiorov, *J. Magn. Magn. Mater*. **1990**, *85*, 129-132.

(66) K. J. Carroll, M. D. Shultz, P. P. Fatouros, E. E. Carpenter, *J. Appl. Phys*. **2010**, *107*, 09B304.

(67) J. Lu, S. H. Yang, K. M. Ng, C. H. Su, C. S. Yeh, Y. N. Wu, D. B. Shieh, *Nanotechnology*. **2006**, *17*, 5812-5820.

(68) H. Zeng, J. Li, J. P. Liu, Z. L. Wang, S. H. Sun, *Nature*. **2002**, *420*, 395 – 398.

(69) C. Y. Haw, F. Mohamed, C. H. Chia, S. Radiman, S. Zakaria, N. M. Huang, H. N. Lim, *Ceram. Int*. **2010**, *36*, 1417-1422.

(70) S. A. Corr, S. J. Byrne, R. Tekoriute, C. J. Meledandri, D. F. Brougham, M. Lynch, C. Kerskens, L. O'Dwyer, Y. K. Gunko, *J. Am. Chem. Soc*. **2008**, *130*, 4214-4215.

(71) N. Arsalani, H. Fattahi, M. Nazarpoor, *Express. Polym. Lett*. **2010**, *4*, 329-338.

(72) A. F. Rebolledo, S. Laurent, M. Calero, A. Villanueva, M. Knobel, J. F. Marco, P. Tartaj, *ACS. Nano*. **2010**, *4*, 2095-2103.

(73) Y. Zhang, J. Y. Liu, S. Ma, Y. J. Zhang, X. Zhao, X. D. Zhang, Z. D. Zhang, *J. Mater. Sci-Mater. M*. **2010**, *21*, 1205-1210.

(74) J. H. Gao, G. L. Liang, J. S. Cheung, Y. Pan, Y. Kuang, F. Zhao, B. Zhang, X. X. Zhang, E. X. Wu, B. Xu, *J. Am. Chem. Soc*. **2008**, *130*, 11828-11833.

(75) B. Basly, D. Felder-Flesch, P. Perriat, C. Billotey, J. Taleb, G. Pourroya, S. Begin-Colin, *Chem. Commun*. **2010**, *46*, 985-987.

(76) M. R. J. Carroll, R. C. Woodward, M. J. House, W. Y. Teoh, R. Amal, T. L. Hanley, T. G. St Pierre, *Nanotechnology*. **2010**, *21*, 035103.

(77) R. Nishiyabu, N. Hashimoto, T. Cho, K. Watanabe, T. Yasunaga, A. Endo, K. Kaneko, T. Niidome, M. Murata, C. Adachi, Y. Katayama, M. Hashizume, N. Kimizuka, *J. Am. Chem. Soc*, **2009**, *131*, 2151-2158.

(78) J. Wan, W. Cai, X. Meng, E. Liu, *Chem. Commun*. **2007**, 5004-5006.

(79) N. Bock, A. Riminucci, C. Dionigi, A. Russo, A. Tampieri, E. Landi, V. A. Goranov, M. Marcacci, V. Dediu, *Acta. Biomater*. **2010**, *6*, 786-796.

(80) K. Shimizu, A. Ito, T. Yoshida, Y. Yamada, M. Ueda, H. Honda, *J. Biomed. Mater. Res. B*. **2007**, *82B*, 471-480.

(81) A. Ito, K. Ino, M. Hayashida, T. Kobayashi, H. Matsunuma, H. Kagami, M. Ueda, H. Honda, *Tissue. Eng*. **2005**, *11*, 1553-1561.

(82) A. Ito, E. Hibino, C. Kobayashi, H. Terasaki, H. Kagami, M. Ueda, T. Kobayashi, H. Honda, *Tissue. Eng*. **2005**, *11*, 489-496.

(83) K. Shimizu, A. Ito, M. Arinobe, Y. Murase, Y. Iwata,Y. Narita, H. Kagami, M. Ueda, H. Honda, *J. Biosci. Bioeng*. **2007**, *103*, 472-478.

(84) H. Nitzsche, H. Metz, A. Lochmann, A. Bernstein, G. Hause, T. Groth, K. Mader, *Tissue. Eng. Pt. C-Meth*. **2009**, *15*, 513-521.

(85) J. E. Hendersona, L. Z. Limb, M. Julienb, S. T. Vengallatorec, M. D. Buschmannd, E. J. Harveye, *Bone*. **2009**, *44*, S260-S261.

(86) G. Frasca, F. Gazeau, C. Wilhelm, *Langmuir*. **2009**, *25*, 2348-2354.

(87) T. Sasaki, N. Iwasaki, K. Kohno, M. Kishimoto, T. Majima, S.I. Nishimura, A. Minami, *J. Biomed Mater. Res. A*. **2008**, *86A*, 969-978.

(88) K. Shimizu, A. Ito, H. Honda, *J. Biosci. Bioeng*. **2007**, *104*, 171-177.

(89) S. H. Hu, T. Y. Liu, C. H. Tsai, S.Y. Chen, *J. Magn. Magn. Mater*. **2007**, *310*, 2871-2873.

(90) A. Ito, K. Ino, T. Kobayashi, H. Honda, *Biomaterials*. **2005**, *26*, 6185-6193.

(91) A. K. Gupta, M. Gupta, *Biomaterials*. **2005**, *26*, 3995-4021.

(92) J. Dobson, Nat. *Nanotechnol*. **2008**, *3*, 139-143.

(93) A. Ito, H. Akiyama, Y. Kawabe, M. Kamihira, *J. Biosci. Bioeng*. **2007**, *104*, 288-293.

(94) R. F. Fakhrullin, J. Garcıa-Alonso, V. N. Paunov, *Soft. Matter*. **2010**, *6*, 391-397.

(95) M. Das, P. Dhak, S. Gupta, D. Mishra, T. K. Maiti, A. Basak, P. Pramanik, *Nanotechnology*. **2010**, *21*, 125103.

(96) A. Sebastianelli, T. Sen, I. J. Bruce, *Lett. Appl. Microbiol*. **2008**, *46*, 488-491.

(97) T. Sen, A. Sebastianelli, I. J. Bruce, *J. Am. Chem. Soc*. **2006**, *128*, 7130-7131.

(98) S. J. Son, J. Reichel, B. He, Abstr. *Pap. Am. Chem. S*. **2005**, *230*, U247.

(99) X. Q. Liu, Y. P. Guan, Y. Yang, Z. Y. Ma, X. B. Wu, H. Z. Liu, *J. Appl. Polym. Sci*. **2004**, *94*, 2205-2211.

(100) X. Q. Liu, J. M. Xing, Y. P. Guan, G. B. Shan, H. Z. Liu, *Colloid. Surface. A*. **2004**, *238*, 127-131.

(101) L. Y. Wang, Y. D. Li, *Chem. Commun*. **2006**, 2557–2559.

(102) B. Le Drogoff, L. Clime, T. Veres, *Microfluid. Nanofluid*. **2008**, *5*,373-381.

(103) L. Y. Wang, J. Bao, L. Wang, F. Zhang, Y. D. Li, *Chem. Eur. J*. **2006**, *12*, 6341-6347.

(104) J. E. Smith, L. Wang, W.H. Tan, Trac. *Trend. Anal. Chem*. **2006**, *25*, 848-855.

(105) P. Wang, J. Q. Zhao, Z. J. Jiang, Y. C. Liu, S. M. Liu, T. Nonferr. *Metal. Soc*. **2009**, *19*, S605-S610.

(106) J. Wang, D. K. Xu, R. Polsky, *J. Am. Chem. Soc*. **2002**, *124*, 4208.

(107) L. Z. Gao, J. Zhuang, L. Nie, J. B. Zhang, Y. Zhang, N. Gu, T. H. Wang, J. Feng, D. L. Yang, S. Perrett, X. Yan, Nat. *Nanotechnol*. **2007**, *2*, 577-583.

(108) H. H. Yang, S. Q. Zhang, X. L. Chen, Z. X. Zhuang, J. G. Xu, X. R. Wang, *Anal. Chem*. **2004**, *76*, 1316-1321.

(109) A. H. Latham, M. E. Williams, *Accounts. Chem. Res*. **2008**, *41*, 411-420.

(110) C. L. Dennis, A. J. Jackson, J. A. Borchers, P. J. Hoopes, R. Strawbridge, A. R. Foreman, J. van Lierop, C. Gruttner, R. Ivkov, *Nanotechnology*. **2009**, 2*0*, 395103.

(111) T. Kikumori, T. Kobayashi, M. Sawaki, T. Imai, *Breast. Cancer. Res. Tr*. **2009**, *113*, 435-441.

(112) V. Zablotskii, O. Lunov, C. Gomez-Plo, *Acta. Phys. Pol. A*. **2009**, *115*, 413-417.

(113) N. Kawai, A. Ito, Y. Nakahara, M. Futakuchi, T. Shirai, H. Honda, T. Kobayashi, K. Kohri, *Prostate*. **2005**, *64*, 373-381.

(114) M. Kawashita, M. Tanaka, T. Kokubo, Y. Inoue, T. Yaoe, S. Hamada, *T. Shinjo*, *Biomaterials*. **2005**, *26*, 2231-2238.

(115) P. Cantillon-Murphy, L. L. Wald, M. Zahn, E. Adalsteinsson, *Concept. Magn. Reson. A*, **2010**, *36A*, 36-47.

(116) A. Ito, F. Matsuoka, H. Honda, T. Kobayashi, *Cancer. Gene. Ther*. **2003**, *10*, 918-925.

(117) S. Wada, L. Yue, K. Tazawa, I. Furuta, H. Nagae, S. Takemori, T. Minamimura, *Oral. Dis*. **2001**, *7*, 192-195.

(118) M. Mahmoudi, A. Simchi, M. Imani, U. O. Hafeli, *J. Phys. Chem. C*. **2009**, *113*, 8124-8131.

(119) S. Mohapatra, S. K. Mallick, T. K. Maiti, S. K. Ghosh, P. Pramanik, *Nanotechnology*. **2007**, *18*, 385102.

(120) N. Kawai, A. Ito, Y. Nakahara, M. Futakuchi, T. Shirai, H. Honda, T. Kobayashi, K. Kohri, *Prostate*. **2005**, *64*, 373-381.

(121) A. K. Gupta, S. Wells, IEEE. *T. Nanobiosci*. **2004**, *3*, 66-73.

(122) Y. Sun, Z. L. Chen, X. X. Yang, P. Huang, X. P. Zhou, X. X. Du, *Nanotechnology*. **2009**, *20*, 135102.

(123) D. B. Wang, D. B. Yu, M. S. Mo, X. M. Liu, Y. T. Qian, *J. Colloid. Interf. Sci* . **2003**, *261*, 565-568.

(124) S. H. Sun, H. Zeng, D. B. Robinson, S. Raoux, P. M. Rice, S. X. Wang, G. X. Li, *J. Am. Chem. Soc*. **2004**, *126*, 273-279.

(125) W. Jiang, Y. Wu, B. He, X. B. Zeng, K. L. Lai, Z. W. Gu, *J. Colloid. Interf. Sci*. **2010**, *347*, 1-7.

(126) J. Xu, H. B. Yang, W. Y. Fu, K. Du, Y. M. Sui, J. J. Chen, Y. Zeng, M. H. Li, G. Zou, *J. Magn. Magn. Mater*. **2007**, *309*, 307-311.

(127) X. F. Qu, Q. Z. Yao, G. T. Zhou, S. Q. Fu, J. L. Huang, *J. Phys. Chem. C*. **2010**, *114*, 8734-8740.

(128) X. Z. Wang, Z. B. Zhao, J. Y. Qu, Z. Y. Wang, J. S. Qiu, *J. Phys. Chem. Solids*. **2010**, *71*, 673-676.

(129) A. S. Bhatt, D. K. Bhat, M. S. Santosh, Physica. B. 2010, 405, 2078-2082.

(130) W. S. Lu, Y. H. Shen, A. J. Xie, W. Q. Zhang, *J. Magn. Magn. Mater*. **2010**, *322*, 1828-1833.

(131) Y. Zhang, J. Y. Liu, S. Ma, Y. J. Zhang, X. Zhao, X. D. Zhang, Z. D. Zhang J. *Mater. Sci-Mater. M*. **2010**, *21*, 1205-1210.

(132) Z. Zou, A. G. Xuan, Z. G. Yan, Y. X. Wu, N. Li, *Chem. Eng. Sci*. **2010**, *65*, 160-164.

(133) A. Trinchi, T. H. Muster1, J. B. Dunlop, S. J. Collocott, 2008 International Conference on Nanoscience and Nanotechnology, **2008**, 83-85.

(134) Y. Lee, J. Lee, C. J. Bae, J. G. Park, H. J. Noh, J. H. Park, T. Hyeon, *Adv. Funct. Mater*. **2005**, *15*, 503-509.

(135) A. J. Barker, B. Cage, S. Russek, C. R. Stoldt, *J. Appl. Phys*. **2005**, *98*, 063528.

(136) Y. W. Zhao, Y. Zhang, H. Zhu, G. C. Hadjipianayis, J. Q. Xiao, *J. Am. Chem. Soc*. **2004**, *126*, 6874-6875.

(137) Y. G. Zhang, F. Lu, Z. Y. Wang, H. X. Wang, M. G. Kong, X. G. Zhu, L. D. Zhang, *Cryst. Growth. Des*. **2007**, *7*, 1459-1462.

(138) J. H. Bang, R. J. Hehnich, K. S. Suslick, *Adv. Mater*. **2008**, *20*, 2599-2603.

(139) Y. C. Li, X. H. Li, C. H. Yang, Y. F. Li, *J. Phys. Chem. C*. **2004**, *108*, 16002-16011.

(140) X. J. Chen, H. F. Xu, N. S. Xu, F. H. Zhao, W. J. Lin, G. Lin, Y. L. Fu, Z. L. Huang, H. Z. Wang, M. M. Wu, *Inorg. Chem*. **2003**, *42*, 3100-3106.

(141) J. H. Yu, J. Joo, H. M. Park, S. I. Baik, Y. W. Kim, S. C. Kim, T. Hyeon, *J. Am. Chem. Soc*. **2005**, *127*, 5662-5670.

(142) Y. C. Zhu, Y. Bando, L. W. Yin, Adv. Mater. 2004, 16, 331-334.

(143) S. H. Yu, M. Yoshimura, *Adv. Mater*. **2002**, *14*, 296-300.

(144) Y. Jiang, X. M. Meng, J. Liu, Z. Y. Xie, C. S. Lee, S. T. Lee, *Adv. Mater*. **2003**, *15*, 323-327.

(145) S. Biswas, S. Kar, *Nanotechnology*. **2008**, *19*, 045710.

(146) G. Ghosh, M. K. Naskar, A. Patra, M. Chatterjee, *Opt. Mater*. **2006**, *28*, 1047-1053.

(147) K. W. Cheah, L. Xu, X. F. Huang, Environ. *Nanotechnology*. **2002**, *13*, 238-242.

(148) C. Kittel, *Introduction to Solid State Physics*, WILEY, **1986**.

Chapter Five

Analytic Techniques

Contents

5.1 BET Surface Area Analysis

5.1.1 Overview

Physisorption of nitrogen was used to determine surface area and pore volume of each solid sample at molecular level. The surface area of materials prepared by sol-gel methods showed a typical type II isotherm, which was expressed in meter square per gram. The data were collected and processed using the Brunauer, Emmett, and Teller (BET) technique by Sorptomatic 1990 apparatus and software automatically [(1)].

5.1.2 Theory

There are two ways that surface adsorption of gas molecules on solid surface can take place, namely physisorption and chemisorption. Physisorption takes place at low temperature over non specific surface sites with multilayers of adsorbate. Conversely, chemisorption of gas molecules on surface is only limited to the maximum of one monolayer on specific surface sites, which can take place at high temperatures.

Brunauer, Emmett and Teller in 1938 had developed an extended method based on Langmuir theory of multilayer adsorption using nitrogen at 77K. Nitrogen is an inert gas suitable for multilayer phsisorption. The equation which presents the BET theory is as follows:

$$\frac{P}{V(P_0 - P)} = \frac{1}{V_m C} + \frac{C - 1}{V_m C}\left(\frac{P}{P_0}\right)$$

Where:

P_0 Saturation pressure at total pressure of gas absorbed at the experimental temperature.
V Volume of gas absorbed at P
V_m Volume of gas absorbed monolayer coverage
C Constant

Surface area can be derived from the P/P_0 values in the range of 0.05- 0.35. However, the values of less than 0.05 give a large degree of error in measurement while the values above 0.35 reach the multilayer adsorption. The equation above is written in form of linear equation $y = m\,x + c$. Plot of $\frac{P}{V(P_0 - P)}$ against $(\frac{P}{P_0})$ yields a straight line with an intercept of $\frac{1}{V_m C}$ and a gradient of $\frac{C-1}{V_m C}$. Both C and $V_m C$ can be calculated and the surface area of the sample can be deduced using the following equation:

$$A = \frac{V_m N_a \sigma}{22414 m}$$

Where:

N_a is Avogadro constant

σ is the area of single nitrogen molecules, which is 1.62 nm^2

m is the mass of the absorbent

5.1.3 Experimental procedure

Surface area measurement of typical sample in this study was performed by nitrogen physisorption to yield the information on pore size and volume of and also the voids between the 2D and 3D packed nanoparticles. A typical sample was placed into a holder of Sorptomatic 1990 which was operated using N_2 at 77 K. About 300 milligrams of samples was pre-dried under 0.1 torr at 150 ^oC for 3 hours prior to the measurement.

5.2 X-Ray Powder Diffraction (XRPD)

5.2.1 Overview

X-ray powder diffraction was used to identify the crystalline phases and estimated the average particle size of the sample.

5.2.2 Theory

Figure 1 shows a typical X-ray diffractometer for the analysis of crystallographic arrangement of a given material. According to Bragg's law the source of X-ray is subject to the solid crystalline material, diffracted waves that are in phase reach the detector to give a peak at specific angles. The relative intensity of peaks and the specific angles at which these peaks appear are characteristics of the sample when compared to database. Highly crystalline materials are suitable for XRPD analysis due to the fact that the wavelength of X-ray is comparable to atomic dimension. Crystalline materials consist of periodically arranged atoms repeatedly throughout the crystal lattices which give mainly a constructive interference with sharp peaks illustrated in figure 2. It is assumed that there are no stack faults and point defects in the bulk material. Conversely, amorphous materials possess irregular arrangement of atoms molecules and ions, which mainly give destructive interference with small degree of constructive interference of broad peaks.

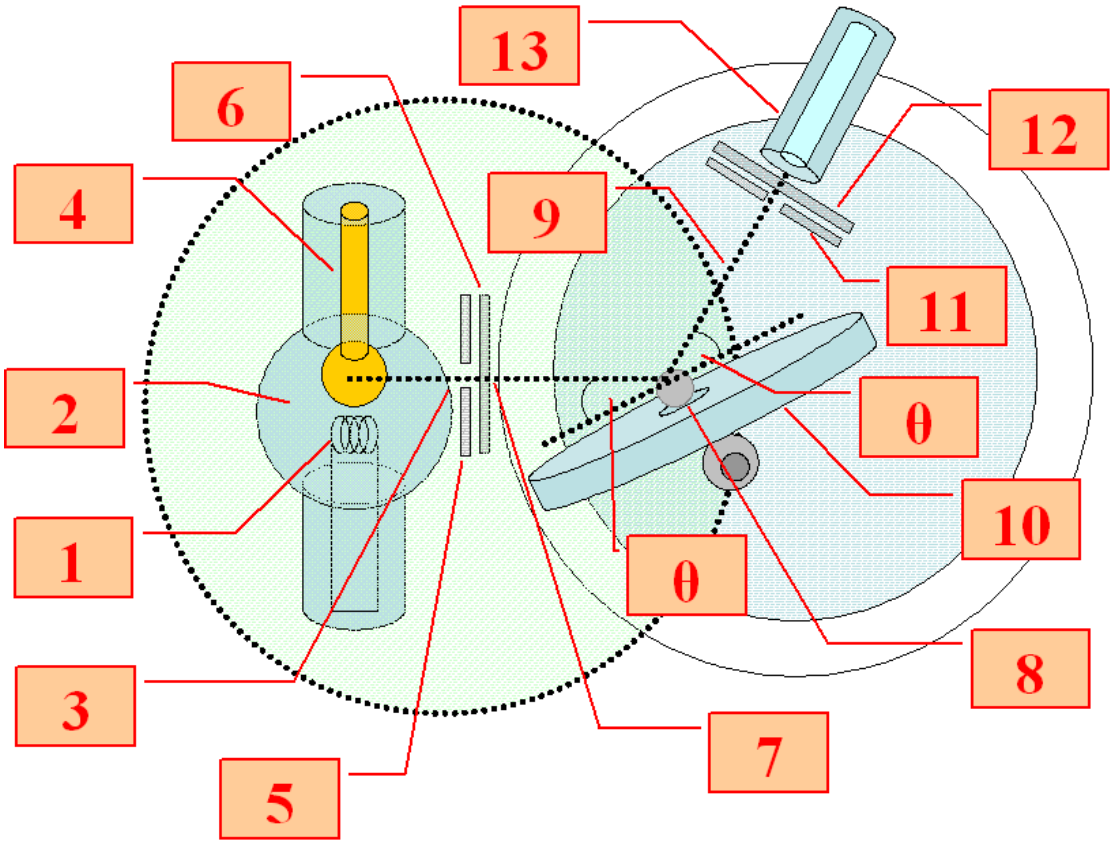

Figure 1: Schematic representation of powder X-ray diffractometer setup, including the parts 1) Tungstun filament, 2) Vacuum, 3) Beryllium window, 4) Copper, 5) Slit, 6) monochromator, 7) Insident X-ray, 8) Crytal sample, 9) Diffracted X-ray, 10) Sample holder disc, 11) Second slit, 12) Secondary monochromator and 13) X-ray detector.

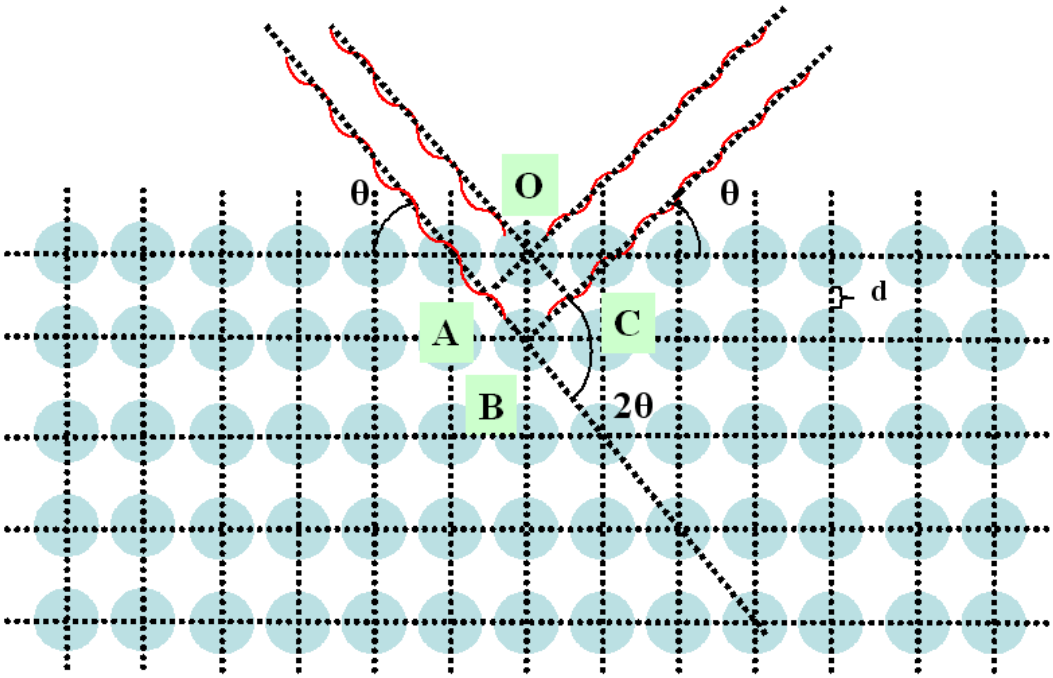

Figure 2: Illustrates the schematic representation of Bragg equation (not to scale).

$$\frac{AB}{OB} = Sin\theta$$

$$AB = OBSin\theta$$

$$OB = d$$

$$AB = BC$$

$$AB = dSin\theta$$

$$BC = dSin\theta$$

$$AB + BC = dSin\theta + dSin\theta$$

$$AB + BC = ABC$$

$$ABC = 2dSin\theta$$

$$n\lambda = 2dSin\theta$$

$$4\theta + 4\gamma = 360^o$$

$$4(\theta + \gamma) = 360^o$$

$$\theta + \gamma = 90^o$$

The two wave fronts must travel parallel and adjacent to each other, when the two wave fronts get diffracted by two adjacent atoms in a line vertically. In order for the

two diffracted waves to keep in parallel and in phase one of which must travel an extra distance of an integral number of wavelength ***n***. This number ***n*** also presents the number of adjacent plane of constructive interference and it is taken to be 1. This is diagrammatically illustrated in figure 2. Materials such as d-metals are highly crystalline materials and amorphous materials such as silica and active carbon, the larger the size of the particle the longer the range domains of periodically arranged atoms and ions and greater the yield of constructive interference resulting in narrow sharp peak. From the broadening of the peak the average size of the weighted particles can be calculated using Scherrer equation represented below:

$$d = \frac{0.9\,\lambda}{B\cos\theta_B}$$

Where:

λ is the wavelength in Angstrom

B in the full width at half maximum in radian

θ_B Bragg's angle

Converting degrees to radians can be calculated very easily by the following equation:

$$2\pi = 360^o$$

$$1^r = \frac{180^o}{\pi}$$

$$1^r = 57.3^o$$

$$1^o = \frac{1^r}{57.3}$$

$$1^o = 0.0174^r$$

1^r one radian is equal to 57.3 degrees and 1^o one degree is equal 0.0174 radians.

5.2.3 Experimental procedure

A powder sample was placed to the XRD sample holder of the Phillips FX3000. Copper Kα radiation of wavelength 1.54056 Å was used. The angle of scan was from 3^o to 70^o with 0.050^o increment of a datum collection. The phases were identified using the database of the Joint Committee on Powder Diffraction Standards (JCPDS). This database contained over 500,000 compounds or materials with their relative peak positions and intensities presented. The average size of the crystallite can be calculated from a selected peak broadening using Debye-Scherrer equation. Instrumental broadening due to electronic and mechanical fluctuations on the wavelength generation was taken into account. Potassium bromide was chosen as a reference material. [2, 3]

5.3 Ultraviolet and Visible Spectroscopy (UV/ Vis)

5.3.1 Overview

UV Visible spectroscopy is an important technique that is widely used for quantitative analysis of chemical specie (solute) in dilute solution. The Beer-Lambert's law is applied to derive the concentration of the solute from absorption value. In this project, drug binding constants and the amounts of GC and BSA required to encapsulate iron oxide particles were derived (Chapter 3) using the UV/ Vis spectroscopy.

5.3.2 Theory [4]

Figure 3 shows the UV-Vis spectrometer setup with all vital parts of the machine. The Beer Lambert Law is expressed mathematically as:

$$A = \varepsilon \times C \times l$$

$$\frac{A}{C \times l} = \varepsilon$$

Where:

ε is the molar absorption coefficient $((\text{Mol L}^{-1})^{-1}\text{cm}^{-1})$ or $((\text{g/cm}^3)^{-1}\text{cm}^{-1}$

A is the absorption no units

C is the concentration of the solution Mol L^{-1} is the path length of the light beam through sample cell in cm

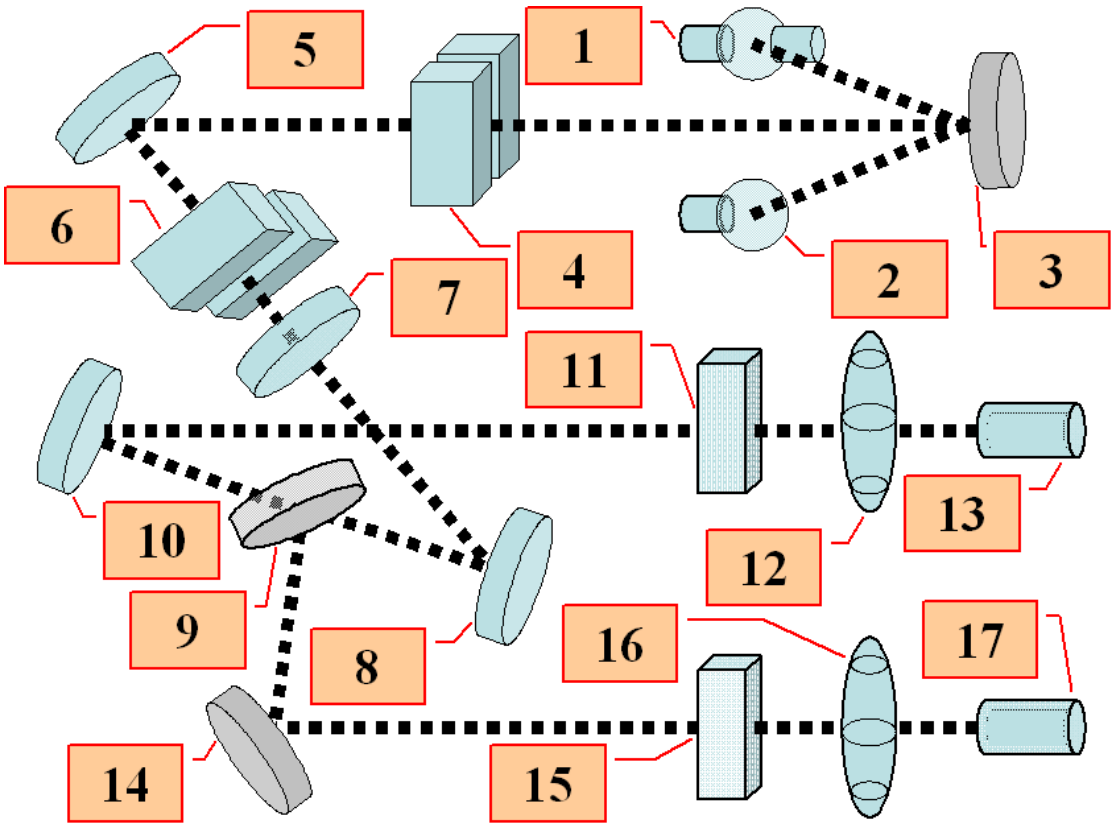

Figure 3 shows UV and Visible spectroscopy setup including: 1) Deuterium lamp for Ultra Violet light source, 2) Tungsten lamp for visible light source, 3) Mirror for reflecting lights, 4) Slit 1, 5) Toroidal grating rotate allowing for specific wavelength to be selected, 6) Slit 2 allowing specific single monochromatic wavelength to pass through, 7) Filter removes higher order of diffracted light beam, 8) Mirror for reflecting lights, 9) Half silvered mirror allowing half of the light to pass through and reflect the other half, 10) Mirror for reflecting light beam to reference cell, 11) Reference cell containing solvent only, 12) Lens for focusing light beam, 13) Detector, 14) Mirror to reflect the other half of light beam to sample cell containing the solvent and the analyte solute, 16) Sample cell and 17) Detector.

5.3.3 Experimental procedure

A drug solution with known concentration was placed into a quartz cuvette and the absorbance was measured using the Lambda 19 UV/Vis NIR Spectrometer. The buffer solution and the distilled water used in this work were established as blank runs in order to minimise the background absorption. The change in drug concentration after the treatment with immobilized BSA as described in Chapter 3 was derived.

5.4 Attenuated Total Reflection Fourier Transformer Infrared Spectrometry FTIR (ATR-FTIR)

5.4.1 Overview

Qualitative and quantitative analyses of organic and biochemical species can be determined using infrared spectroscopy in the region of 400 to 4000 cm^{-1}. This technique is widely used to identify the presence of amide I and amide II groups in protein molecules, aldehydes and ketones in carbohydrates and silanol in silica, etc.

5.4.2 Theory

The functional groups of a compound can generate characteristic IR absorption peaks. The model of a bond between two atoms can be analogues to a spring connected to two spheres at each end. The bond or the spring vibrates at different energy depending on the mass of the bonded atoms (masses of the spheres) and the strength of the bond (the stiffness spring) is related to the following mathematical equation:

$$\upsilon = \frac{1}{2c\pi}\sqrt{\frac{k}{\mu}}$$

$$\mu = \frac{m_a m_b}{m_a + m_b}$$

$$F = -kx$$

Where:

υ is the frequency of vibration in Hertz or s^{-1}

c in the speed of light in m/s

μ is the reduced mass Kg

π is the pie constant

k is the spring constant of the bond N/m

m_a is the mass of the a bonded atom

m_b is the mass of the b bonded atom

F is the restoring force of the spring in N

x is the displacement of spring from on end to its equilibrium position m

Each bond vibrates at a particular frequency, which allows it to be identified and for historical reasons the frequency of vibration is expressed in terms of wavenumber in cm^{-1} and it is proportional to frequency.

An IR beam passes through the pathway to interferometer consisting of beam splitter and two mirrors that are right angles to each another. This produces interferogram that gives the intensity of the infrared radiation at different frequencies simultaneously before it passes through the sample and into the detector. The signal from the interferogram is decoded mathematically using Fourier transformation technique that gives the log of the relative intensity of initial intensity to the transmitted for the individual frequencies, which produces a plot of absorbance against wavenumber. Some frequencies are absorbed more than others depending on what bonding present in the molecules. The sample holder is made of diamond, which protects the zinc selenide layer below. The zinc selenide layer is used to amplify the infrared signal and also acted as a medium with high refractive index to achieve attenuated total reflection. This allows the sample to be analysed in solid or liquid state without

further preparation. The laser beam is reflected to the surface of the sample before being reflected by the upper mirror and guided to the detector by a second mirror, as shown in figure 5.5. A blank run is performed before the sample run, this is to reduce if not eliminated background absorbance of air and other media used to dissolve the sample solute. There are different types of sample holders for different types of solid crystals and liquid samples. A cover is provided for liquid sample to prevent any possible evaporation. Figure 4 shows a diagrammatic representation of the Fourier transformed infrared radiation and the attenuated total reflection sample cell holder, as shown in figure 5.

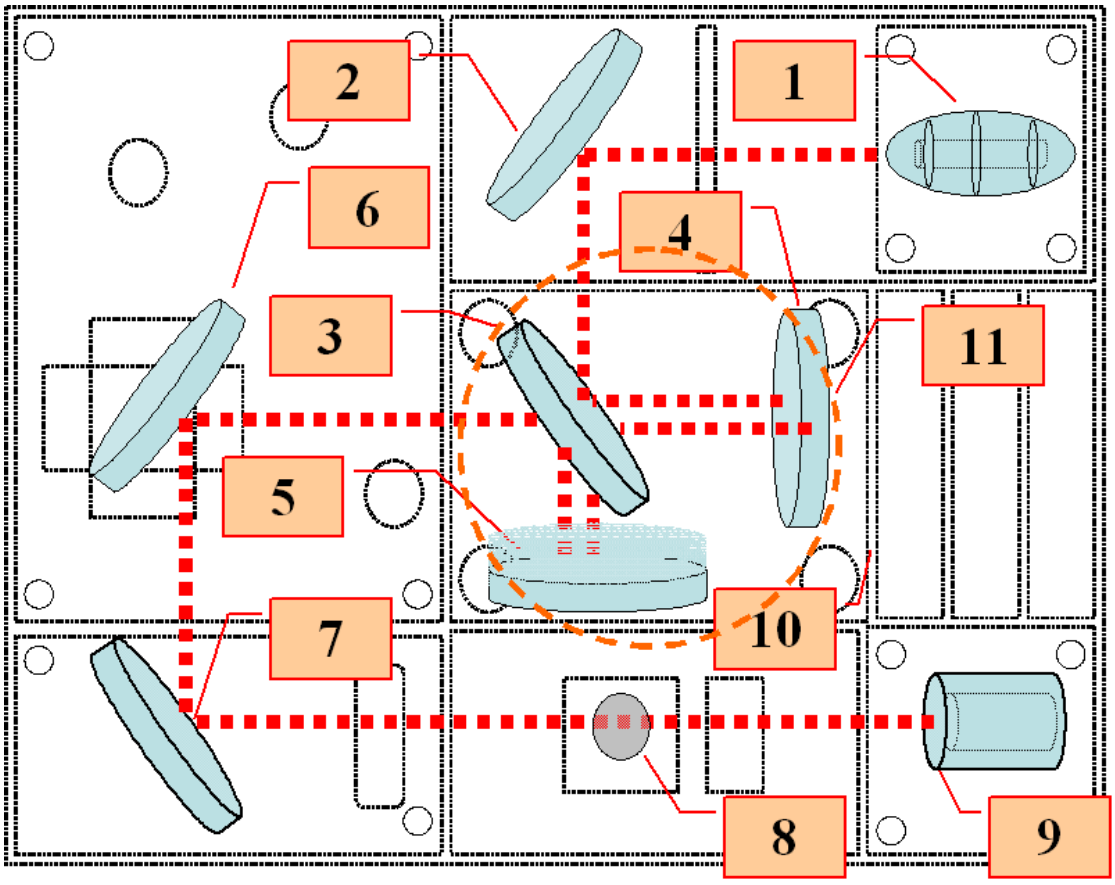

Figure 4 shows Fourier transformer infrared including, 1) Electric heater and reflective capsule for infrared source, 2) Mirror for reflecting beam, 3) Half silvered mirror for beam splitting, 4) Fixed mirror, 5) moveable mirror, 6) Reflecting mirror 1, 7) Reflecting mirror 2, 8) Sample holder, 9) Infrared detector, 10) Filter panel removing dust and moisture and 11) Interferogram.

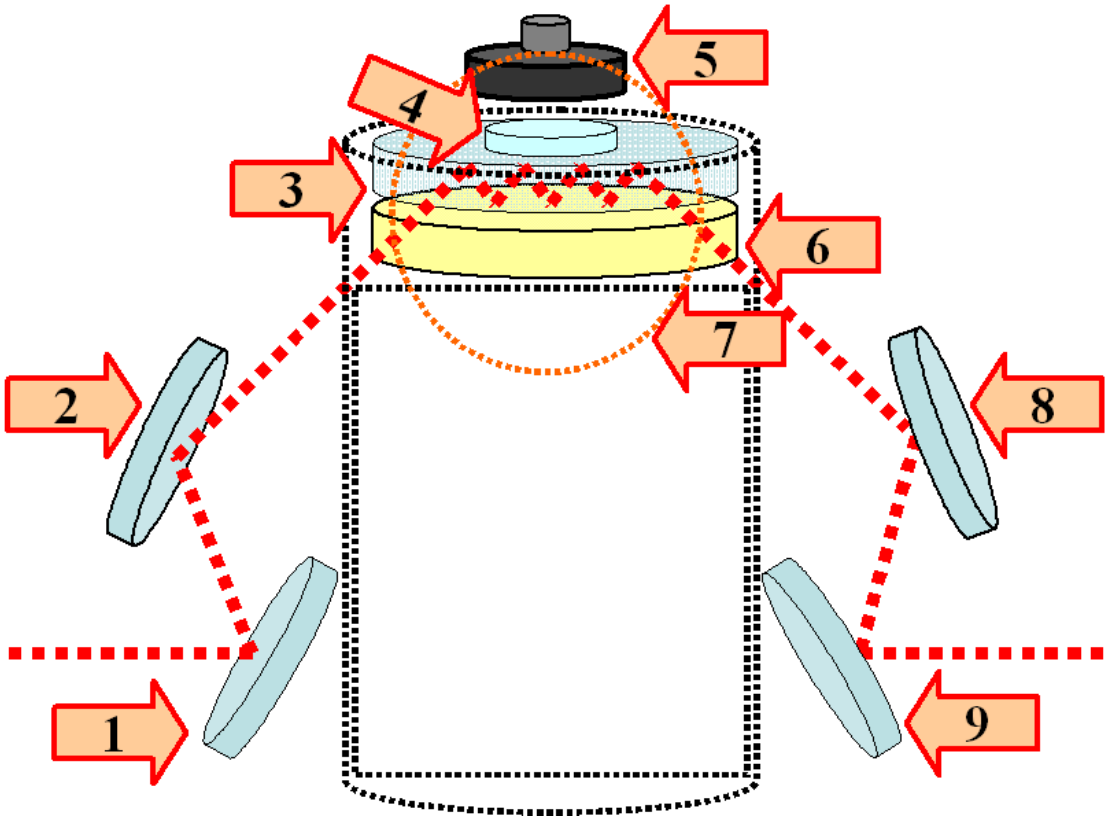

Figure 5 shows Attenuated Total Reflection (ATR) sample holder section, 1) Reflecting mirror 1 bending the infrared beam, 2) Reflecting mirror 2 for bending beam to surface, 3) Diamond window to protect zinc selenide window 6), 4) Sample drop to analyse, 5) Sample holder compressor, 6) Zinc Selenide window, 7) Attenuated total reflection optical pathway, 8) Reflecting mirror 3 to bend infrared beam back to the instrument 9) Reflecting window bending infrared back to it original path.

5.4.3 Experimental procedure

In this study, a selected sample prepared for the ATR-FTIR spectroscopy was dispersed in water at 1 mg/ mL concentration. A homogeneous solution was ensured with sonication treatment at 50 Hz for 15 minutes at room temperature. The FTIR instrument was connected to a heated regulator called the Golden Gate. The sample was pre-heated at 70 ^{o}C and dried after placing few drops of the solution onto the diamond window. Blank run was collected under the same conditions but without the sample. The sample was analysed from 600 to 4000 cm^{-1} at 4 cm^{-1} resolution for 110

scans. The same number of scans was performed for the blank run in order to obtain meaningful and reliable spectra for each sample.

5.5 High Resolution Transmission Electron Microscopy (HRTEM)

5.5.1 Overview

The particle shape, size and distribution in a typical sample can be visualised using high resolution transmission electron microscopy (HRTEM). The obtained lattice fringe distances and inter-planar angles can also allow phase identification. Materials with high electron density are suitable for this microscopic technique and low electron density amorphous material can be seen as they appear with light shades.

5.5.2 Theory

Similar to optical microscopy electron microscopy works under a very similar principle, which are shown in figure 5.2. Instead of using visible light in the case of the optical microscope high energetic electron beam is used in the electron microscope. The highly intense electron beam is produced by passing a high voltage to a heated filament. The energy of electron is in the range of 100-200 keV under high vacuum closed system of 10^{-6} mbar and the point to point resolution of the electron microscope can reach below 1.94 Å. [5] The interior part of an electron microscope can be seen in figure 6. [6] As the electron beam hits on a sample, back scattering of electrons at an angle can take place as result of mutual repulsion between the negatively charged electrons with the electron dense material of the sample. Secondary electron scattering could also take place. X-ray radiation can occur due to electron ionization to the higher energy level as a result of electron collision, leaving a vacant positive hole for electrons in the subsequent higher energy to occupy. The energy difference between the two energy levels librates X-ray or electrons could penetrate the sample with sufficient energy in area where there are voids and gaps. This is shown diagrammatically in figure 7. [7] HRTEM allows high resolution

imaging of individual nanoparticle where their crystallographic phases can be identified and the distance between layers within single crystal phase called fringes can be measured and closely compared with that given by the X-ray crystallography.

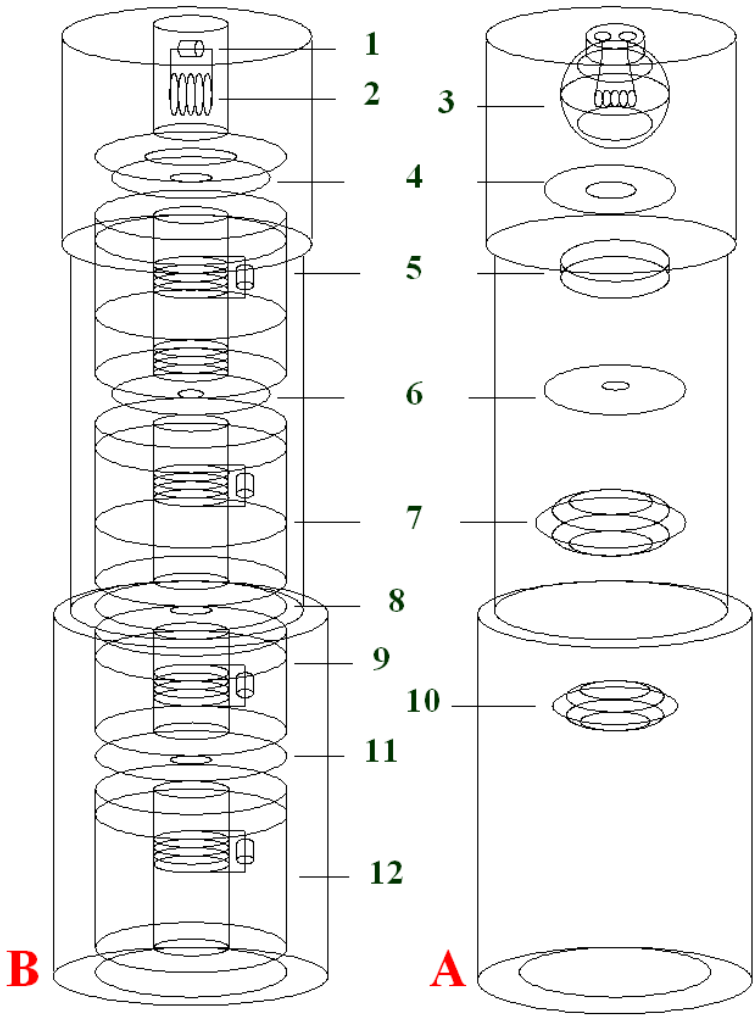

Figure 6 shows optical microscope, A, closely compared with electronic microscope B. The diagram shows the parts inside each microscope including: 1 high voltage input, 2 electron gun LaB_6 for electron source in electron microscope, 3 light bulb for light source in optical microscope, 4 aperture in both microscope, 5 condensers in both microscope, 6 specimen compartment to contain the analysed sample in both microscope, 7 objective lens in both microscope, 8 aperture in electron microscope, 9 intermediate electron lens in electron microscope, 10 projector in optical microscope, 11 aperture in electron microscope and 12 electron projector lens in electron microscope.

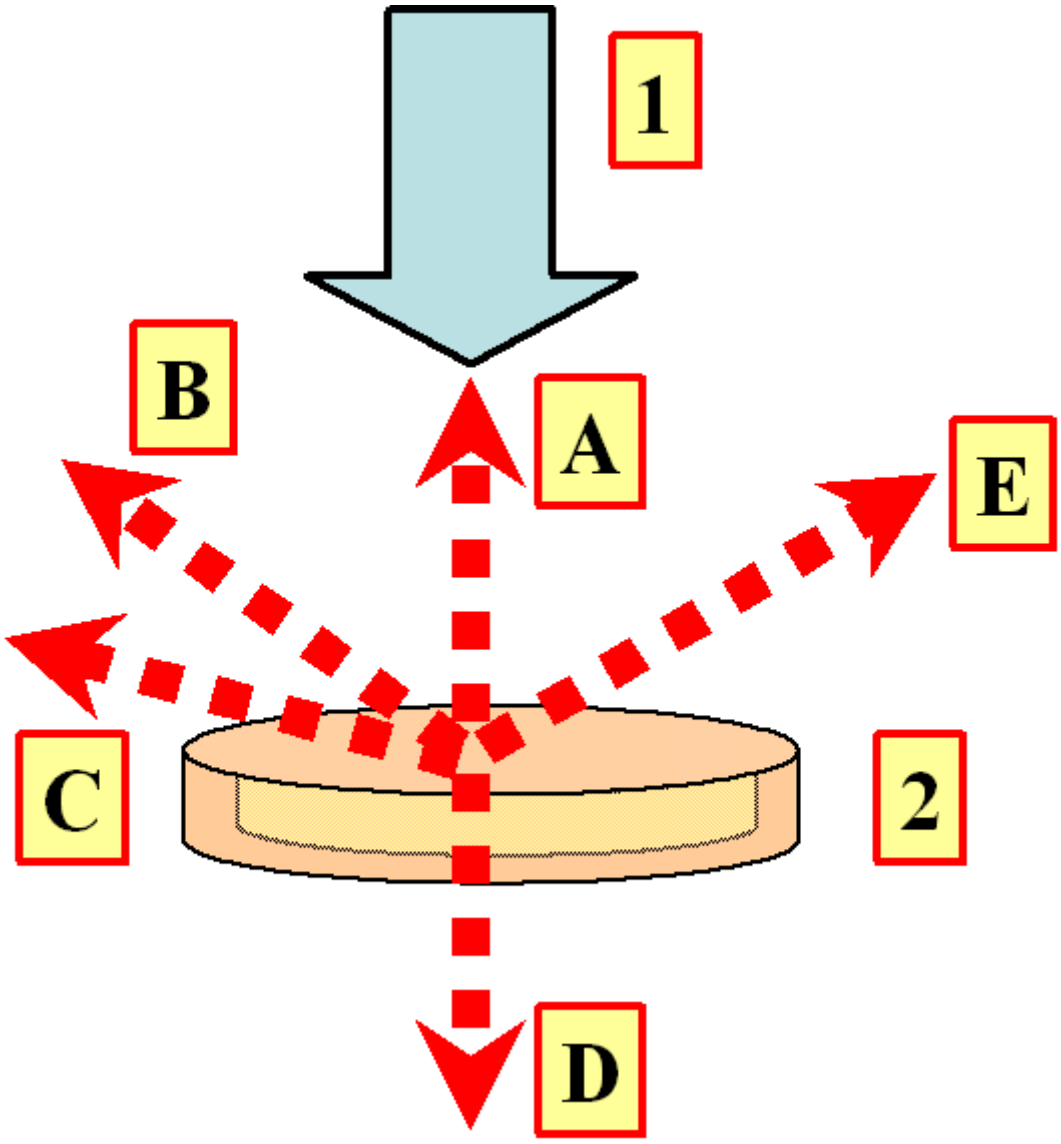

Figure 7 shows the possible interaction between primary electron beam 1) and sample carbon/copper grid 2) in electron microscope. A) Electron back scattering, B) Angular electron scattering, C) Secondary electron scattering, D) Electron beam penetration and X-ray radiation E).

5.5.3 Experimental procedure

Both the JEOL2000FX and JEOL 2010 electron microscopes operated at 200-300 kV with point to point resolution of about 1.94 Å were used to analyse the samples in this project. A suspension (0.1 mg in 1mL organic solvent) for each sample was prepared and sonicated at 50- 60 Hz for 15 minutes, followed by placing 2-3 drops of the

sample suspension onto a copper grid. The grid was made up of 300 copper grid bars covered with a holy thin carbon film as support. The solvent was allowed to evaporate before the dried sample on the Cu grid was loaded into the chamber of the microscope under a high vacuum.

5.6 Thermal Gravimetric Analysis (TGA)

The TGA technique can provide qualitative and quantitative assessment of the thermal stability of a solid sample under specified conditions. The change of sample weight with respect to programmable increase in temperature is recorded.

A sample typically, 10- 20 mg was placed in a nitrogen atmosphere. The flow of nitrogen gas was set in two directions, one projected vertically down at 40 mL/min and the other projected horizontally out at 60 mL/min. The horizontal flow of nitrogen must be sufficiently higher than the vertical flow to prevent extra weight applied to the sample crucible introducing artefacts to the result, damage to the weighing string and to ensure the removal of volatile chemical that are corrosive to the instrument to escape. A diagrammatic illustrating a thermal gravimetric analyser with all vital parts is shown in figure 8 and with sample furnace shown in figure 9. This technique is often used to adsorbed organic molecules on the surface of metal nanoparticle such as carboxyl, amine and hydroxyl groups, etc.

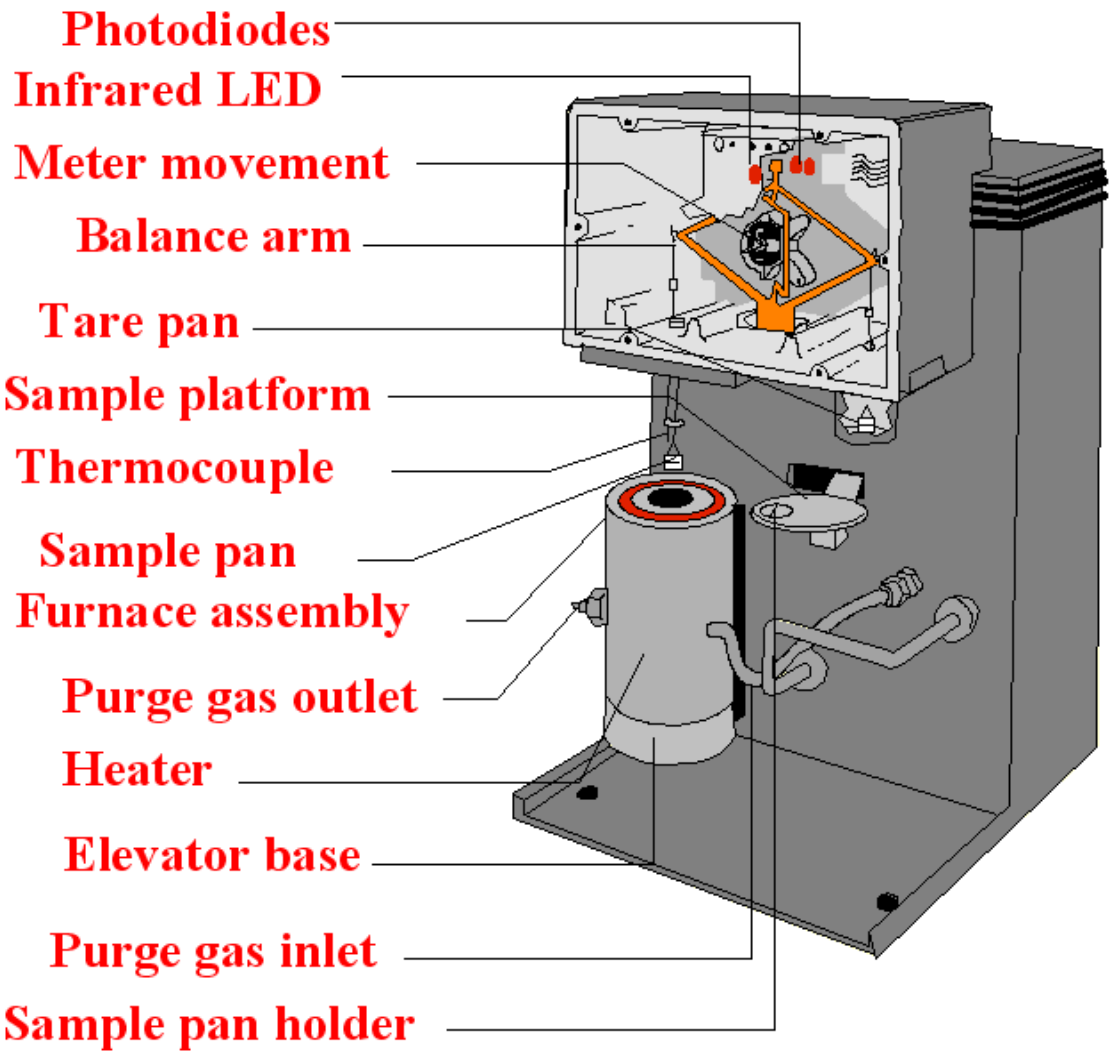

Figure 8 shows a typical thermal gravimetric analysis setup inside out. The picture was taken from thermal analysis (TA) instrument.

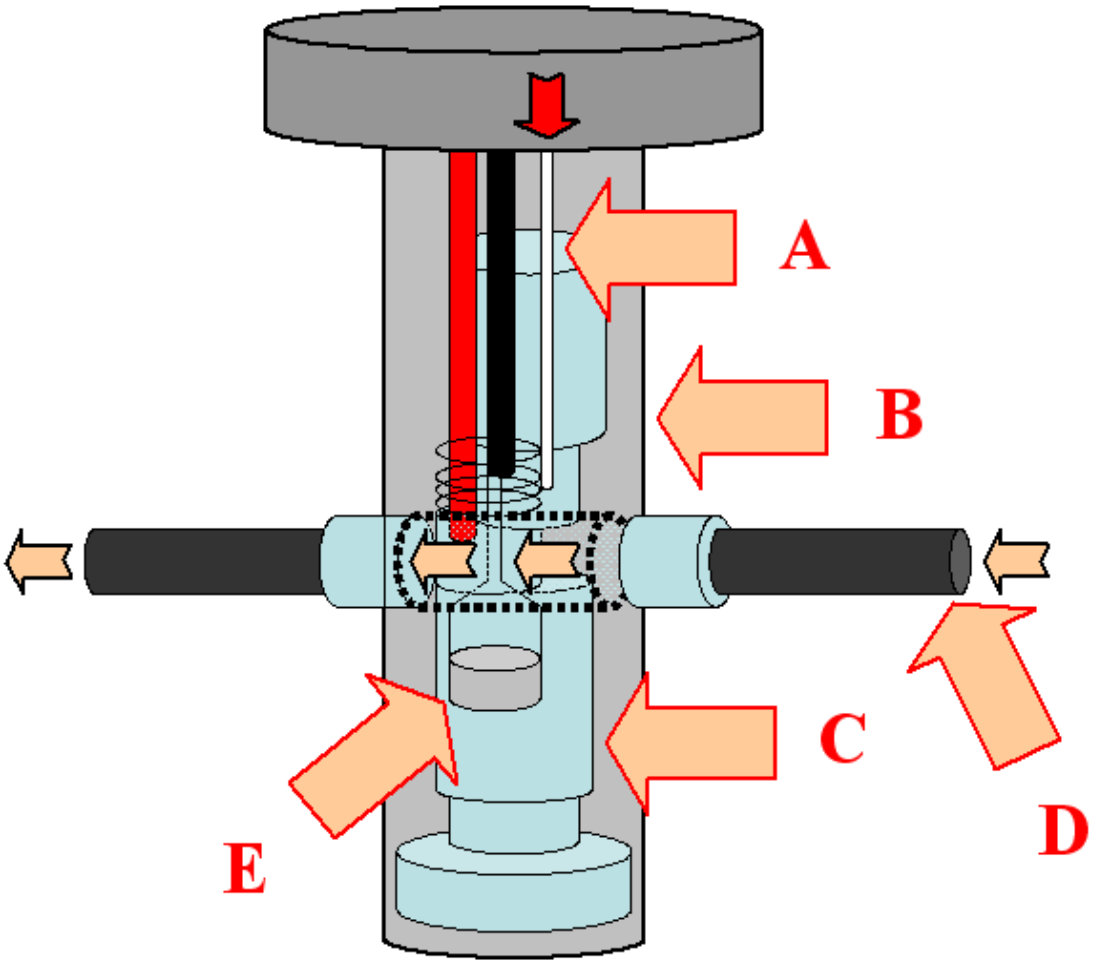

Figure 9 shows a typical thermal gravimetric furnace setup inside out containing the sample crucible. A) Balance purge, B) Furnace housing, C) Furnace, D) Furnace Purge and E) Sample pan.

5.7 Vibrating Sample Magnetometry (VSM)

5.7.1 Overview

This technique used for a wide verity of materials that respond differently under the change of external magnetic field including diamagnetic, paramagnetic, ferromagnetic, ferrimagnetic, anti-ferromagnetic and super-paramagnetic materials. The instrument was first designed by Simon Foner in 1956. [8]

Our samples were tested at the Centre for Nanodestructive Evaluation and Ames Laboratory in Iowa State University, USA.

5.7.2 Theory

A magnetic moment can be induced to a sample upon application of a constant external magnetic field. The sample is magnetised by the magnetic field which in turn by the magnetic domain's alignment with the field. The induced magnetic domain is created due to the alignment of individual magnetic spins in solid with the external magnetic field. The stronger the external magnetic field the larger the magnetisation. Piezoelectric vibrator attached to the sample causes it to vibrate in sinusoidal motion. This generates sinusoidal electric signals, which are detected by coils. The amplitude of this signal is equivalent to the frequency of vibration in motion and its magnitude. A diagrammatic VSM setup is shown in Figure 10.

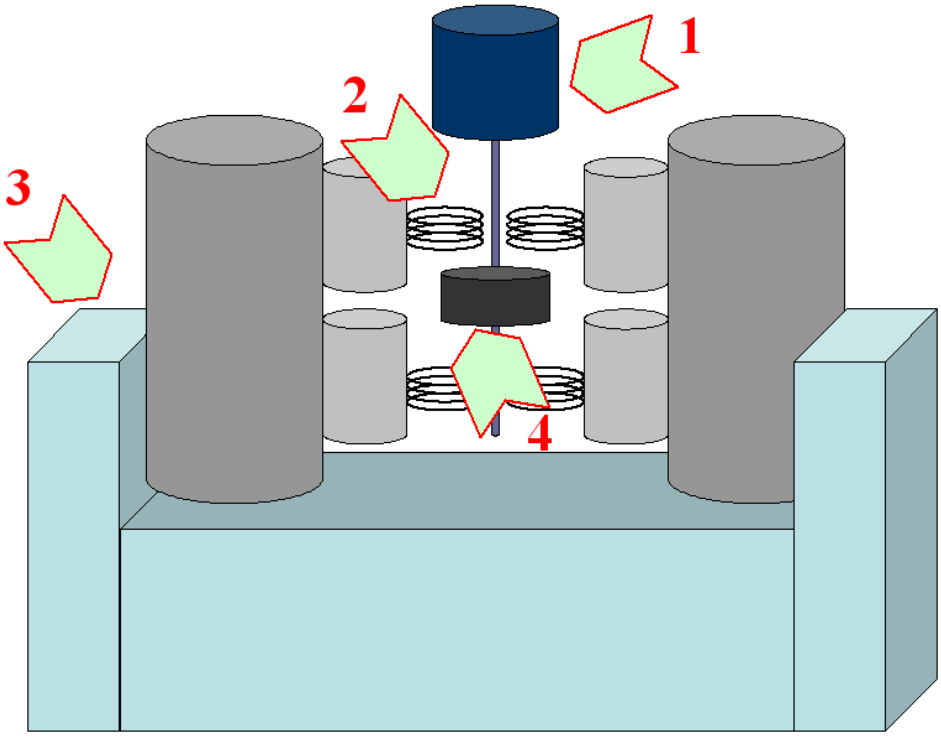

Figure 10 shows VSM setup with essential parts including: 1) piezoelectric vibration unit, 2) pick up coils, 3) external magnet and 4) sample holder.

5.7.3 Experimental Procedure

A typical sample in powder form was placed in a plastic tube in a secure fixed place, which was to prevent the displacement or the realignment of individual dipole moment with respect to the coil. The sample holder was weighed and filled with sample particles and reweighed to work out the weight of sample inserted. The VSM model 4500 Princeton Applied Research with 7000 Oersted external applied magnetic field was employed.

5.8 Superconduction Quantum Interference Device (SQUID)

This instrument is used to measure the magnetic moment of materials with the highest sensitivity operated at very low current to voltage ratio and nearly absolute zero temperature. The equipment can adopt two modes of measurements, direct current (DC) and alternating current (AC). Using a very small quantity of sample for the measurement there is almost no interference from the heat change due to the electron interaction with the vibrating crystal lattice. But, this can be significant in VSM where larger amount of sample is needed due to its intrinsic low sensitivity. A uniform magnetic field in the range of 5- 18 Tesla is produced in the SQUID by a programmable bipolar power supply. The uniform magnetic field is set to align with an axial cylindrical bore of a superconducting detection coil, which is an essential component of the SQUID. When an external magnetic field is applied to the sample, an induced magnetic field from the sample is created and measured. Figure 11 shows the schematic of a SQUID with a superconducting loop immersed in liquid helium around a sample capsule.

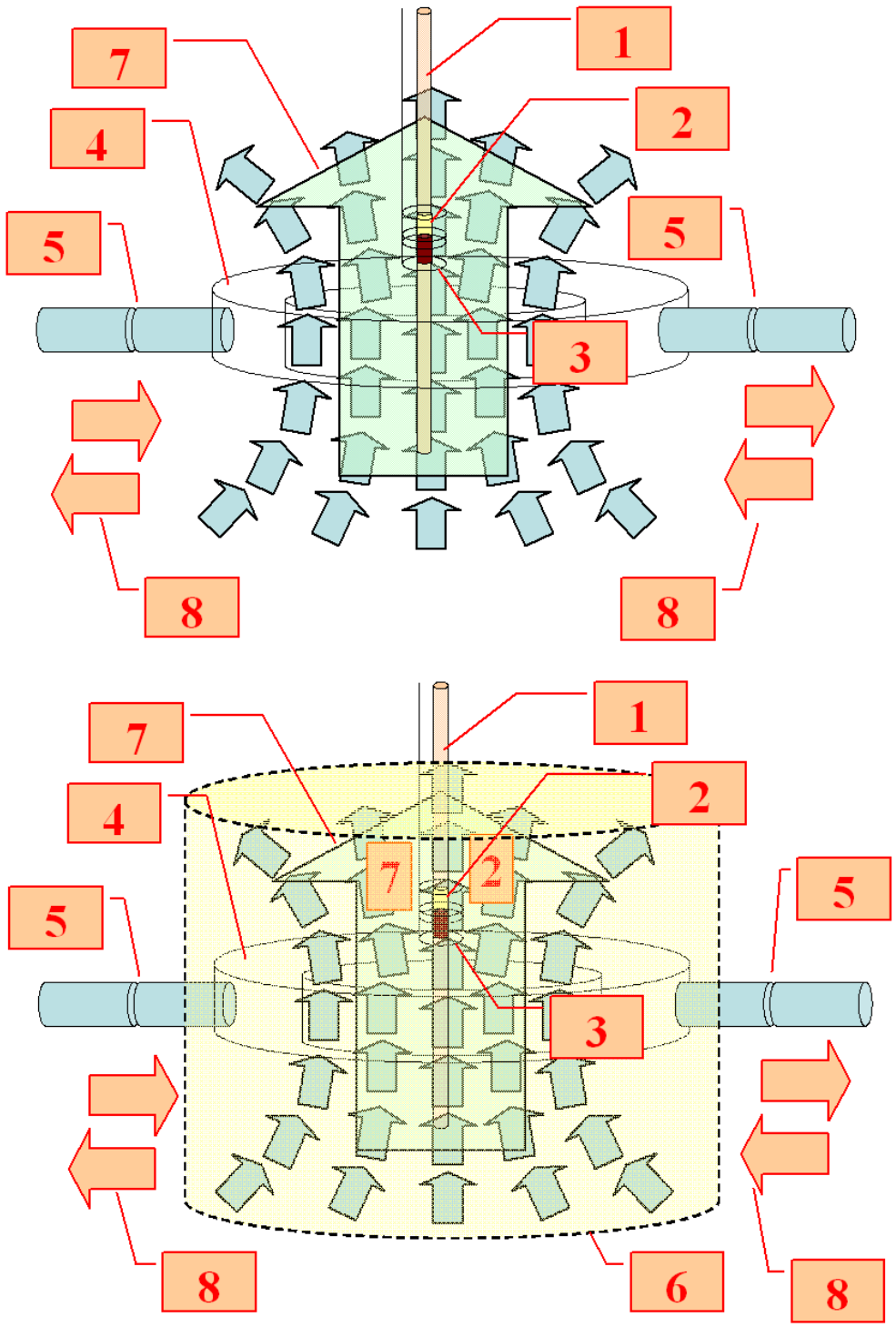

Figure 11 shows superconducting loop in superconducting quantum interference devices (SQUID) with the following parts, 1) Sample straw, 2) Sample capsule, 3) Sample coil, 4) Superconducting loop, 5) Josephson junction, 6) Liquid helium, 7) Magnetic field direction, and 8) Direction of electric current.

5.9 Zeta Potential

Zeta potential is the potential created at the interface of double charged layers on a colloid surface. Charged particles in colloidal systems possess double charged layers. Between the doubly charged interfaces there are two types of layers, a fixed plane called Stern layer and a dynamic layer entitled Nernst diffused layer. At the first surface of the particle, the charge is the strongest to hold the oppositely charged species in a fixed position. However as this charge propagates to outer layers, this becomes weaken with a higher surface area as a result of extended volume. The electrostatic interaction is relatively weak, which results in weakly held oppositely charged species. Figure 12 illustrates the fixed Stern layer and the diffused Nernst layer.

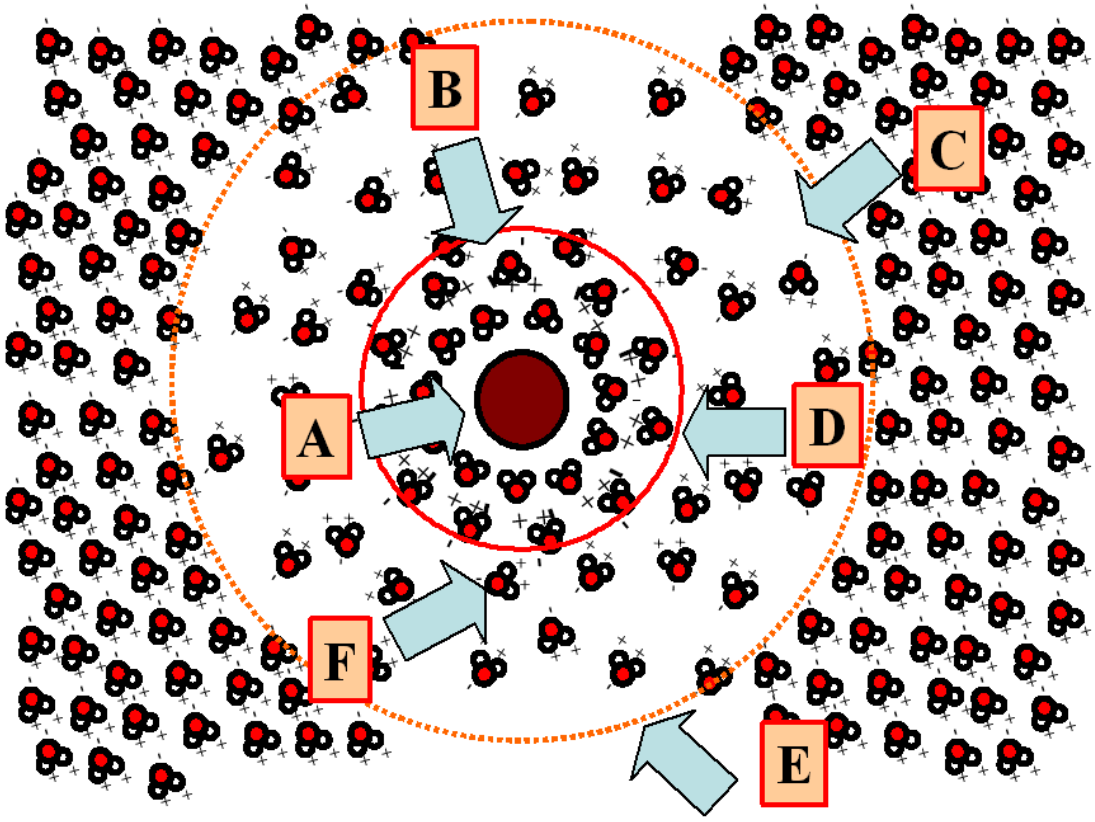

Figure 12 shows the A) colloidal particle such as iron oxide, B) Stern fixed layer surrounding the iron oxide particle, C) Nernst diffused layer, D) layer boundary between Stern layer and Nernst layer, E) solvent (water) molecules and F) layer boundary between Stern layer and the surrounding water molecules.

The magnitude of zeta potential of particle depends critically on the external pH value. At lower pH the colloid surface is covered with excess of positive charge and at higher pH there are excess negative charged hydroxyl groups. By varying the pH values the colloid particle passes through a neutral point called isoelectric point (IE) where the kinetic mobility of the particle is almost zero. This isoelectric point is very difficult, near to the impossible, to define experimentally and can only be derived by extrapolating from either positive point to negative point or the vice versa.

The zeta potential of colloidal particles can be calculated theoretically from the mathematical expression given below:

$$\zeta = \frac{4\pi\eta v_{\varepsilon}}{D}$$

Where:

η is the viscosity of solvent in Pa.s or kg/(m.s)

v_{ε} is the electrophoresis mobility of colloidal particle $C^2\ N^{-1}\ m^{-2}$

ζ is the zeta potential of particle in mV

D is the dielectric constant of solvent in no units

Figure 13 shows the schematic equipment for the zeta potential measurement where a typical sample is placed in a special sample holder. Measuring electrophoresis mobility of a particle, viscosity and dielectric constant of a solvent system allow the zeta potential to be evaluated. The dielectric constant or permittivity is a constant that indicates how easily a material can be polarized by electric field compared to vacuum as insulating material; this is mathematically expressed as the ratio of permittivity of the material to that of vacuum in the equation below

$$\boldsymbol{D} = \frac{\boldsymbol{\varepsilon_s}}{\boldsymbol{\varepsilon_o}}$$

Where:

$\boldsymbol{D}$ is the dielectric constant in no unit

$\boldsymbol{\varepsilon_s}$ is the static permittivity of the material in $J^{-1}C^2m^{-1}$

$\boldsymbol{\varepsilon_0}$ is vacuum permittivity in $J^{-1}C^2m^{-1}$

A Malvern instrument, the Malvern Zeta Master is equipped with a helium-neon laser light source to measure the electrophoresis mobility of colloidal particles. In this instrument, two coherent waves of red light are sent across the capillary cell at stationary level. Electric field is applied to the sample in suspension. The sample particles migrate as a result of attraction by the opposite charge applied by the electric field. This induces frequency of fluctuation, which depends on the mobility of the particle. The sample scatters the red laser beam as it passes across. When the scattered beam reaches the photomultiplier detector, the signal can then be processed by digital collector. [(9)] Figure 14 shows the Malvern instrument with the built-in zeta potentiometer.

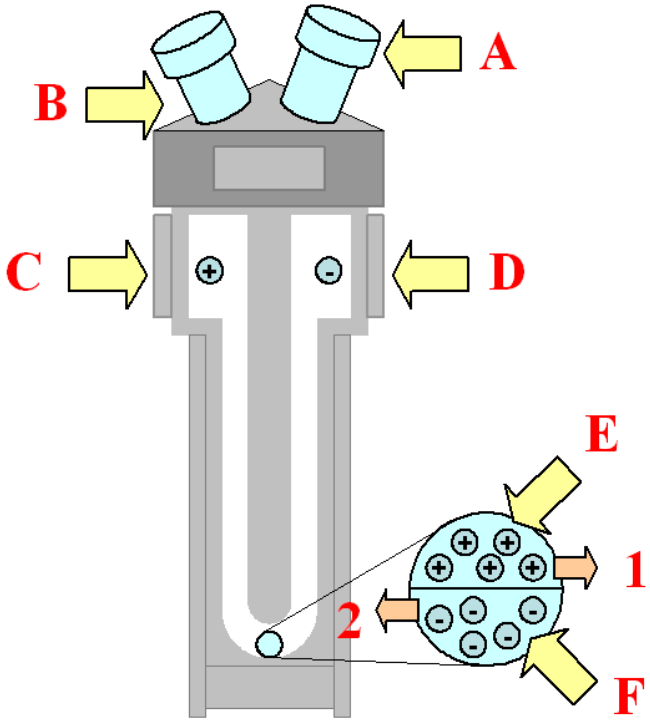

Figure 13 shows the sample cell with important parts including: A) Cap cell, B) Sample inlet, C) Anode electrode, D) Cathode electrode, E) Positively charge ion, F) Negatively charge ion, 1) Positively charged ion migrate to negatively charged electrode cathode and 2) Negatively charged ion migrate to positively charged electrode anode.

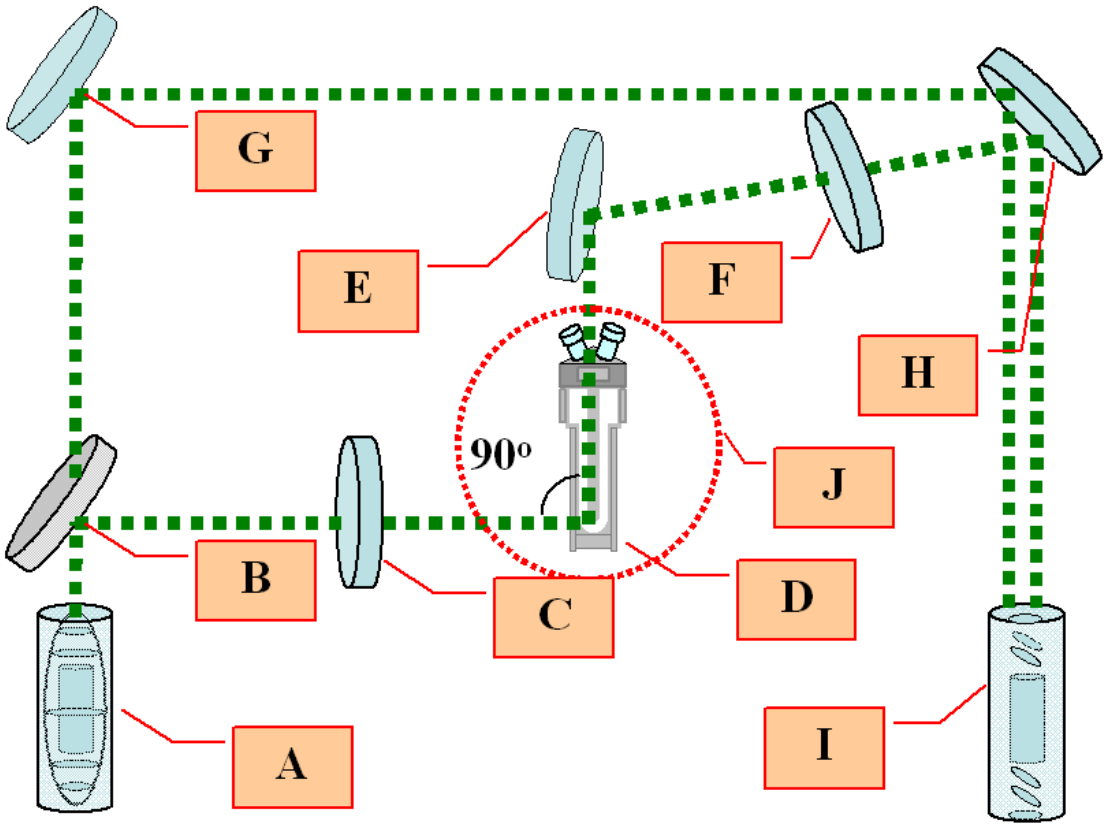

Figure 14 shows the zeta-sizer potentiometer with following vital component: A) Laser at high energy of 10^{15} Hz, B) Beam splitter, C) Attenuator, D) Sample cell, E) Reflecting mirror, F) Compensating optics, G) Reflecting mirror, H) Combining optics, I) Detector and J) Sample compartment.

Zeta potentials were measured in this thesis including iron oxide, silica, GC, BSA and encapsulated GC and BSA using the Malvern Zeta Master. [(10)] The samples were placed at different pH valued solutions ranging from 3.0-11.0 and the zeta potential values were measured for each pH value when sufficient equilibrium time (5 mins) was given.

5.12 References

(1) S. Bruauer, P. H. Emmett, E. Teller, J . Am. Chem. Soc. 1938, 60, 309.

(2) D. A. Skoog, F. J. Holler, T. A. Nieman, in Principles of Instrumental Analysis, Harcourt Brace College Publishers, Florida, 1998.

(3) M. T. Weller, Inorganic Materials Chemistry, Oxford University Press Inc., Bath, 1994.

(4) G. Gauglitz, T. Vo-Dinh, Handbook of Spectroscopy, WILEY-VCH GmbH&Co. KGaA, Weinheim, 2003.

(5) P. J. Goodhew, F. J. Humphreys, Electron Microscopy and Analysis, 2nd ed., 1988.

(6) R. B. Anderson, P. T. Dawson, Experimental Methods in Catalytic Research, Academic Press, London, 1976.

(7) J. W. Niemantsverdriet, Spectroscopy in catalysis: an introduction, VCH, New York, 1993.

(8) M. Solzi, M. Ghidini, G. Asti, Magnetic Nanostructures, American Scientific Publishers, California, 2002.

(9) R. J. Hunter, Introduction to modern colloid science, Oxford University Press, Oxford, 1993.

(10) D. J. Shaw, Introduction to Colloid and Surface Chemistry, Butterworth-Heinemann, Oxford, 1991.

Chapter Six

Conclusion

Contents

6.1 Conclusion

There are a number of conclusions I would like to make after the completion of my DPhil research. First, it has been long known that nano size iron oxide particles can be used as magnetic vehicles for chemicals or bio-chemicals for a wide range of new applications but it is challenging to ensure that the immobilisations can be done effectively. In this DPhil study, I demonstrate some simple and cost effective methods for the preparations of encapsulated iron oxide with biological species and materials with catalytic and optical interests using sol-gel, layer by layer and Ostwald ripening techniques, etc.

It is well accepted that magnetic nanoparticles can have many exciting applications in biomedical and electronic areas. In this thesis, it is however, clearly shown that extensive interaction of small magnetic particles with the biological molecules could partially or completely denature the attached biological materials. Thus, it is not recommended to mix the two materials directly. As a result, magnetic iron oxide nanoparticle encapsulated in porous SiO_2 is therefore developed to entrap the biological and organic materials for the applications in the areas of cancer treatments and toxic pollutant degradation treatments, respectively. Also, in this work, I demonstrate the encapsulation of magnetic material in soft organic based materials GC and BSA. Using these composites there is no attenuation in the binding values of the water soluble drug molecules such as diazepam, ibuprofen and warfarin, etc. with the immobilised BSA. This method may open up the materials to be used as contrast enhancement agents in MRI. In addition, using the same methodology it is possible to encapsulate other biological or non-biological materials for the fine tune of specific applications. This technique should allow wider scopes for bioinorganic nanotechnology applications.

Another new method to encapsulate magnetic materials in porous ZnS via Ostwald ripening using thermal decomposition method is also developed in this DPhil research. It is shown that iron oxide nanoparticles as ‘seed nuclei’ can be used to initiate the growth of ZnS over-layer. It has been well documented that the use of ZnS

photocatalytic materials in waste treatment is expensive and offers low efficiency due to the difficulty in their separation from product solutions. I show in this thesis that incorporation of a magnetic core into the ZnS can ensure regeneration of the composite material by magnetic separation for a longer life span. The combination of magnetic and photocatalytic properties was never exploited before this work and this approach may extend the application of magnetic nanoparticles to the area of energy research using photoactive ZnS based materials. Using this method different types of semiconducting and photocatalytic materials to encapsulate magnetic core materials can also be envisaged.

Chapter Seven

Chemical Material

Appendix 1= List of chemical

Name of chemical	Name of company	Purity of chemical	Quantity
Iron (II) chloride	Sigma-Aldrich	99%	250 g
Iron (III) chloride	Sigma-Aldrich	97%	1 kg
Ammonia solution	Fisher Scientific	35%	2.5 l g
Zinc acetate	Aldrich	99.99%	25 g
Glycol chitosan	Sigma	≥ 60%	1 g
Bovine serum albumin	Sigma	99%	25 g
Cetyltrimethyl ammonium bromide	Sigma	≥99%	100 g
Tetraethyl ortho silicate	Aldrich	≥99.0%	250 ml
Dipotassium hydrogen phosphate trihydrate	Sigma-Aldrich	≥99.0%	500 g
Potassium dihydrogen phosphate	Sigma	≥99.0%	500 g
Diethylene glycol	Sigma	≥99.0%	500 ml
Toluene	Sigma-Aldrich	≥99.9%	1 l
Thiourea	Sigma-Aldrich	≥99.0%	500 g
Polyvinylpyrrolidone (M_w= 40000)	Sigma-Aldrich	99.%	100 g
Diazepam	Sigma	-	100 mg
Ibuprofen	Aldrich	99%	1 g
Warfarin	Fluka	-	10 g
Ethanol	Fisher Scientific	-	500 ml
Hydrochloric acid	Fisher Scientific	32%	2.5 l
Sodium hydroxide	Sigma-Aldrich	99.99%	100 g